N°d'ordre NNT : 2023-ISAL-0015

THESE de DOCTORAT DE L'INSA LYON, membre de l'Université de Lyon

Ecole Doctorale N° ED 162
Mécanique, Énergétique, Génie civil, Acoustique

Spécialité de doctorat : Génie Mécanique

Soutenue publiquement le 03/03/2023, par :
Zineb BOULAAJAJ

Numerical and experimental study of crack propagation on monocrystalline silicon wafers

---

Devant le jury composé de :

BONAMY, Daniel	Expert Senior, HdR (CEA Saclay)	Rapporteur
RETHORE, Julien	Directeur de Recherche CNRS(Ecole Centrale de Nantes)	Rapporteur
ADDA-BEDIA, Mokhtar	Directeur de Recherche CNRS (ENS Lyon)	Examinateur
PRABEL, Benoit	Ingénieur de Recherche (CEA Saclay)	Examinateur
NELIAS, Daniel	Professeur (INSA de Lyon)	Directeur de thèse
FOURMEAU, Marion	Maitresse de Conférences (INSA de Lyon)	Encadrante
MAIGRE, Hubert	Chargé de Recherche CNRS (INSA Lyon)	Invité

Département FEDORA – INSA Lyon - Ecoles Doctorales

SIGLE	ECOLE DOCTORALE	NOM ET COORDONNEES DU RESPONSABLE
CHIMIE	**CHIMIE DE LYON** **https://www.edchimie-lyon.fr** Sec. : Renée EL MELHEM Bât. Blaise PASCAL, 3e étage secretariat@edchimie-lyon.fr	**M. Stéphane DANIELE** C2P2-CPE LYON-UMR 5265 Bâtiment F308, BP 2077 43 Boulevard du 11 novembre 1918 69616 Villeurbanne **directeur@edchimie-lyon.fr**
E.E.A.	**ÉLECTRONIQUE, ÉLECTROTECHNIQUE, AUTOMATIQUE** **https://edeea.universite-lyon.fr** Sec. : Stéphanie CAUVIN Bâtiment Direction INSA Lyon Tél : 04.72.43.71.70 secretariat.edeea@insa-lyon.fr	**M. Philippe DELACHARTRE** INSA LYON Laboratoire CREATIS Bâtiment Blaise Pascal, 7 avenue Jean Capelle 69621 Villeurbanne CEDEX Tél : 04.72.43.88.63 **philippe.delachartre@insa-lyon.fr**
E2M2	**ÉVOLUTION, ÉCOSYSTÈME, MICROBIOLOGIE, MODÉLISATION** **http://e2m2.universite-lyon.fr** Sec. : Bénédicte LANZA Bât. Atrium, UCB Lyon 1 Tél : 04.72.44.83.62 secretariat.e2m2@univ-lyon1.fr	**Mme Sandrine CHARLES** Université Claude Bernard Lyon 1 UFR Biosciences Bâtiment Mendel 43, boulevard du 11 Novembre 1918 69622 Villeurbanne CEDEX **sandrine.charles@univ-lyon1.fr**
EDISS	**INTERDISCIPLINAIRE SCIENCES-SANTÉ** **http://ediss.universite-lyon.fr** Sec. : Bénédicte LANZA Bât. Atrium, UCB Lyon 1 Tél : 04.72.44.83.62 secretariat.ediss@univ-lyon1.fr	**Mme Sylvie RICARD-BLUM** Institut de Chimie et Biochimie Moléculaires et Supramoléculaires (ICBMS) - UMR 5246 CNRS - Université Lyon 1 Bâtiment Raulin - 2ème étage Nord 43 Boulevard du 11 novembre 1918 69622 Villeurbanne Cedex Tél : +33(0)4 72 44 82 32 **sylvie.ricard-blum@univ-lyon1.fr**
INFOMATHS	**INFORMATIQUE ET MATHÉMATIQUES** **http://edinfomaths.universite-lyon.fr** Sec. : Renée EL MELHEM Bât. Blaise PASCAL, 3e étage Tél : 04.72.43.80.46 infomaths@univ-lyon1.fr	**M. Hamamache KHEDDOUCI** Université Claude Bernard Lyon 1 Bât. Nautibus 43, Boulevard du 11 novembre 1918 69 622 Villeurbanne Cedex France Tél : 04.72.44.83.69 **hamamache.kheddouci@univ-lyon1.fr**
Matériaux	**MATÉRIAUX DE LYON** **http://ed34.universite-lyon.fr** Sec. : Yann DE ORDENANA Tél : 04.72.18.62.44 yann.de-ordenana@ec-lyon.fr	**M. Stéphane BENAYOUN** Ecole Centrale de Lyon Laboratoire LTDS 36 avenue Guy de Collongue 69134 Ecully CEDEX Tél : 04.72.18.64.37 **stephane.benayoun@ec-lyon.fr**
MEGA	**MÉCANIQUE, ÉNERGÉTIQUE, GÉNIE CIVIL, ACOUSTIQUE** **http://edmega.universite-lyon.fr** Sec. : Stéphanie CAUVIN Tél : 04.72.43.71.70 Bâtiment Direction INSA Lyon mega@insa-lyon.fr	**M. Jocelyn BONJOUR** INSA Lyon Laboratoire CETHIL Bâtiment Sadi-Carnot 9, rue de la Physique 69621 Villeurbanne CEDEX **jocelyn.bonjour@insa-lyon.fr**
ScSo	**ScSo*** **https://edsciencessociales.universite-lyon.fr** Sec. : Mélina FAVETON INSA : J.Y. TOUSSAINT Tél : 04.78.69.77.79 melina.faveton@univ-lyon2.fr	**M. Bruno MILLY** Université Lumière Lyon 2 86 Rue Pasteur 69365 Lyon CEDEX 07 **bruno.milly@univ-lyon2.fr**

*ScSo : Histoire, Géographie, Aménagement, Urbanisme, Archéologie, Science politique, Sociologie, Anthropologie

Abstract

Mechanical failure is a critical phenomenon affecting the electrical performances of monocrystalline silicon, which is commonly used for solar cells and microelectromechanical systems. The main cause behind the catastrophic failure of such Si components is dynamic crack propagation. Numerous studies were conducted to apprehend this cleavage failure both at the initiation of the crack and along its propagation. Interestingly, it was found that crack propagation in monocrystalline silicon can reach up to 80% of Rayleigh wave speed. This threshold value has made us question whether some micro-processes or dissipation phenomena are taking place in the vicinity of the crack.

As part of the efforts made to shed light on the kinetic aspects of cracks, a numerical study is carried out to predict its propagation velocity and evolution. The inertial effects are accounted for using an explicit integration scheme. An exhaustive study was conducted to determine the numerical parameters that could control or influence the onset and the evolution of rapid crack propagation. Since we initially aimed at reproducing experimental bending tests, a three-dimensional model was necessary. The fracture approach XFEM was used and the explicit 3D model was implemented on the open-source code Cast3m.

A series of fracture experiments employing the potential drop technique were performed to characterize the crack velocities precisely. The samples were thin monocrystalline wafers onto which a thin chrome layer and gold electrodes are deposited. To control the crack path, a notch was made by hand on each wafer. The electrical circuit is a battery-feed Wheatstone bridge with our silicon wafer replacing one of the resistances. Crack propagation engenders a change in the voltage measurement. A relationship between the voltage across the wafer and the crack front position enables us to derive the crack velocity. This high-resolution experimental set-up is then validated by simultaneously performing the same measures using a high-speed camera.

KEYWORDS: eXtended Finite Element Method, dynamic fracture, explicit integration scheme, 3D crack propagation, potential drop technique, crack velocity, high-speed camera.

Résumé

La défaillance mécanique est un phénomène critique affectant les performances électriques du silicium monocristallin, couramment utilisé dans les cellules photovoltaïques et les systèmes micro électromécaniques. La rupture fragile dynamique des composants Si est principalement causée par la présence de fissures. De nombreuses études ont été menées pour appréhender les tendances d'une rupture fragile par clivage. D'un point de vue expérimental, il s'avère que la propagation des fissures dans le silicium monocristallin peut atteindre jusqu'à 80% de la vitesse des ondes de Rayleigh. Cette vitesse limite a soulevé de nombreuses questions quant à sa dépendance vis-à-vis de la microstructure et des phénomènes dissipatifs survenant en pointe de fissure.

Dans le cadre des efforts déployés pour élucider le caractère dynamique des fissures, une étude numérique est réalisée afin de prédire leur vitesse de propagation et son évolution au cours du temps. Les effets inertiels sont pris en compte à l'aide d'un schéma d'intégration explicite. Une étude préliminaire a d'abord été menée dans le but de définir tous les paramètres numériques qui pourraient intervenir et influer sur l'apparition et l'évolution de la discontinuité mobile. Initialement, nous avions pour objectif de reproduire les essais expérimentaux, ainsi un modèle tridimensionnel s'avérait indispensable. L'approche XFEM a été utilisée afin de simuler les fissures et le modèle 3D explicite a été implémenté sur le code open source Cast3m.

Vu la rapidité du phénomène et la géométrie de nos échantillons, la caractérisation fine de la vitesse des fissures représente un enjeu de taille. Pour ce faire, une série de mesure par couches minces a été effectuée. Les échantillons sont des wafers en silicium monocristallin préparés préalablement en déposant sur leurs surfaces une mince couche de chrome et des électrodes en or. Afin de contrôler la trajectoire de la fissure, une pré-entaille a été faite à la main sur chaque wafer. Le circuit électrique est un pont de Wheatstone constitué de 4 résistances, où l'une est remplacée par un wafer et d'une pile alimentant l'ensemble. L'extension de la fissure entraîne un changement notable dans la mesure de tension. Une relation entre la tension et la position du front de fissure nous permet de déduire la vitesse de propagation. Cette configuration expérimentale à très haute fréquence est ensuite validée en effectuant simultanément les mêmes mesures à l'aide d'une caméra rapide.

MOTS CLÉS: XFEM, rupture fragile, dynamique, fissuration 3D, méthode de mesure par couches minces, vitesse de propagation, caméra rapide.

Contents

List of Figures

List of Tables

Introduction

Fracture mechanics has always been considered one of the most challenging fields of mechanics and structural engineering. The existence of defects within a given material may compromise the structural integrity of the industrial component, thus making it more prone to catastrophic failure. Many recent studies were conducted to elucidate the driving mechanisms of cracks and the overall material response. Based on a thorough theoretical characterization of what is occurring in the vicinity of cracks, the general concepts of fracture have been established. However, an extensive understanding of the physics behind some of the fracture mechanisms has not been achieved yet and is subject to several ongoing investigations.

In fracture analysis, brittle failure has been regarded as one of the most critical, yet complex types of fracture. In such cases, failure occurs instantly and at a relatively high crack velocity. The irreversibility and the suddenness of this phenomenon are all the more difficult to prevent from happening. As for the dynamic features of fracture, they are especially outlined in two main configurations: for stationary cracks under a dynamic loading such as impact and for rapidly moving cracks subjected to a quasi-static loading. Since the inertial effects are quite substantial, addressing either problem requires their integration within the crack description: from its initiation and along its propagation.

Nowadays, with all the climate change issues such as the lack of natural resources and the constantly increasing levels of pollution, it has become urgent to advocate the use of a higher share of renewable energy. Therefore, many developments are carried out to improve their performance and efficiency. As part of its missions, the French National Research Agency (ANR) invested in multi-scientific platforms to test the durability of solar systems (Equipex DURASOL). One among which has been installed in the laboratory LaMCoS. Its main objective is to characterize solar cells' mechanical properties, most importantly the monocrystalline and multicrystalline silicon wafers. While dwelling on the environmental factors that prevent solar cells from achieving higher electrical efficiency, it has been observed that their performance is inherently dependent on the integrity of their components. Besides the brittleness of crystalline silicon, the small thickness of wafers makes them easily breakable throughout the manufacturing process and during usage. This major drawback hinders photovoltaic systems from improving the energy return on investment. In the work of Carton [CAR 20], a probabilistic study has been thoroughly conducted to assess the reasons behind the onset of failure.

The work carried out by Lv Zhao and Wang Meng [ZHA 16, WAN 19b] aimed at characterizing the cleavage fracture of monocrystalline wafers provided by CEA-INES. One key aspect has particularly drawn our attention. The measured crack velocities in pre-notched specimens approach the Rayleigh wave velocity C_r, which is a few kilometers per second. This renders the failure process instantaneous. However, it is intriguing how the cracks would never attain this terminal velocity, but rather end up propagating at a limiting speed representing 80% of C_r. To apprehend the physical mechanisms associated with such accelerating cracks, a series of experiments were carried out on monocrystalline wafers [WAN 19b]. The crack velocities were quantified using a high-speed camera, yet few measurement points were reported due to the rapid crack growth rate. Overall, it appears that cracks propagate at a steady state. As for the crack speed values, they may vary from hundreds of meters to a few kilometers per second. The main cause behind this variation is the fracture stress of the specimen, hence its notch length [WAN 19b]. Furthermore, a meticulous fractographic examination of the cracked surfaces was formerly performed to investigate any arising feature or surface mark that may shed some light on dissipation processes or wave interaction. Besides, finite element simulations have been carried out on multicrystalline silicon and were able to predict the crack trajectory throughout various grains [ZHA 16].

Given the industrial need to overcome and avoid cracking problems, many approaches have been developed to predict crack initiation and trajectory. The scientific community has also put effort into seeking a deeper knowledge of failure mechanisms such as crack velocity or crack instabilities. The present study comes as a complementary work to the two previous doctoral theses. It aims to further explore the numerical aspect of the problem, in particular crack speed. By choosing the adequate approach capable of simulating dynamic crack propagation, we intend to recover the variation of crack speed along its path numerically. Also, the initiation and propagation criteria will be examined so as their relevance towards predicting crack velocity without any calibration. In this thesis, we focus on implementing the Extended finite elements (XFEM) in the open-source software Cast3m of the CEA to simulate dynamic crack propagation on monocrystalline silicon.

In the first chapter, a brief introduction to the history of fracture mechanics is presented. Herein, we recall the scientific breakthroughs that shaped the actual fracture mechanics field. Then, the general concepts of linear elastic fracture mechanics (LEFM) are introduced. Within, we recollect the advances made toward a better understanding of dynamic fracture and their fundamental assumptions. Eventually, different cracking criteria are reviewed.

In the second chapter, a state of the art of the numerous numerical methods, their advantages and limitations are discussed. As part of our work, the use of an explicit time integration solver and a three-dimensional model has been crucial for our algorithm.

Therefore, a detailed analysis has been performed to assess which approach would be appropriate for our problem. The same goes for the software, which needed to be open-source.

The third chapter is devoted to the implementation of an explicit XFEM model of dynamic crack propagation in 3D structures. This study has first focused on reviewing the missing procedures to be implemented in Cast3m. The simulation assumptions are explained, the key steps of the algorithm and the developed procedures are detailed. Furthermore, a parametric study of the 3D crack problem is presented. Initially, the intended objectives were to compare numerical results with experiments. Due to the high computational cost, all the simulations are performed on a simplified model to check and validate the correct functioning of the code. Therefore, crack velocities are computed but can not be compared nor verified experimentally.

In the fourth chapter, it was important to follow up on the experimental work that has been done before. A higher-resolution acquisition method for crack velocity measurements has been installed. The potential drop technique and its different settings are discussed. The first series of experiments were conducted on notched specimens of monocrystalline silicon. From the measured electrical signal, the crack velocity and its profile are depicted. Nevertheless, no data was available to compare and validate our electrical setup. In view of the existing methods, it seemed more reliable to combine this newly implemented technique with the high-speed camera. For a given test, the crack average and instantaneous velocities of both methods are compared and the measurement uncertainties are commented on.

Chapter 1

Fracture Mechanics: State of the Art

Contents

1.1 Introduction

This chapter presents the basics and the theoretical notions of fracture mechanics. The history of this mechanical field will be recalled to provide an insight into the developments it went through and how it became one of the most sought-after and crucial domains in materials engineering. In light of our studied material, monocrystalline silicon, we will mainly focus on brittle failure and its various mechanisms. Eventually, an exhaustive review of some of the most notorious fracture criteria will be provided.

1.2 Historical background

Inglis [ING 13] was the first to investigate stress concentrations in the vicinity of a crack tip. For a linear elastic material, he considered a plate with an elliptical hole subjected to a uniform loading. He found that when the radius of curvature at the crack tip tends to zero, thus an ideal sharp crack, the stresses tend to infinity. His findings are the foundation of the asymptotic solution of the crack-tip stress fields.

Years later, Griffith observations [GRI 21] on glass fibers brought him to attempt an energetic approach based on thermodynamic equilibrium to solve the fracture problem. This approach was mainly motivated by the conflicting facts noted while testing the foregoing assumption. He noticed that the stress needed to reach the complete failure of glass fibers can be quantified and is not as infinite as it had been presumed. As a result of his theoretical analysis, Griffith stated that crack propagation results from the conversion of elastic strain energy into fracture surface energy. This theory is only limited to the range of linear elastic materials undergoing brittle fracture. Griffith criterion can be formulated as follows:

$$G = 2\gamma \tag{1.1}$$

where G is the elastic strain energy and γ is the surface energy.

1.3 Linear elastic fracture mechanics

Linear Elastic Fracture Mechanics (LEFM) is the branch of fracture mechanics where the size of the plastic zone ahead of the crack tip is negligible with respect to crack length. Therefore, all the nonlinear processes of the process zone are disregarded. Fracture in brittle materials is usually addressed using this analysis.

Based on the applied load, different fracture modes can be identified (cf. FIG.1.1):

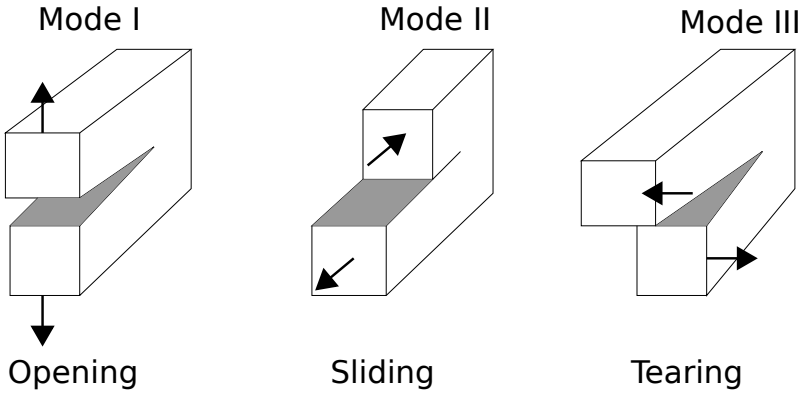

Figure 1.1: The three fracture modes.

— Mode I, denoted opening mode, is characterized by a normal displacement of the crack surfaces with respect to the plane of the crack and is caused by a tensile stress.

— Mode II, denoted sliding mode, is the result of an in-plane shear stress. Herein, the crack surface tends to move in the plane of the crack and perpendicular to the crack front.

— Mode III, denoted tearing mode when an out-of-plane shear stress is applied. This fracture mode is marked by an in-plane crack surface displacement which is parallel to the crack front.

Structures are often subjected to complex load patterns, where a combination of these three modes is expected.

1.3.1 Asymptotic approach

Using polar coordinates (r, θ) with the origin at the crack tip (cf. FIG.1.2), Irwin [IRW 21] quantified the stress field in the vicinity of a crack as:

$$\sigma_{ij} = \frac{K_I}{\sqrt{2\pi r}} f_{ij}^{I}(\theta) + \frac{K_{II}}{\sqrt{2\pi r}} f_{ij}^{II}(\theta) + \frac{K_{III}}{\sqrt{2\pi r}} f_{ij}^{III}(\theta) + o(\sqrt{r}), \tag{1.2}$$

where the contribution of each fracture mode is taken into account by introducing the stress intensity factors, denoted as K_i and where the subscript i refers to the type of fracture (i = I, II, III), $f_{ij}(\theta)$ are the Westergaard functions [WES 21] that only depends on the angle θ and σ_{ij} the stress field components at the crack tip. The singularity of the stress field is outlined by the term $\frac{1}{\sqrt{r}}$, which tends to infinity once at the crack tip ($r = 0$). For a linear static analysis, the static stress intensity factors are defined as :

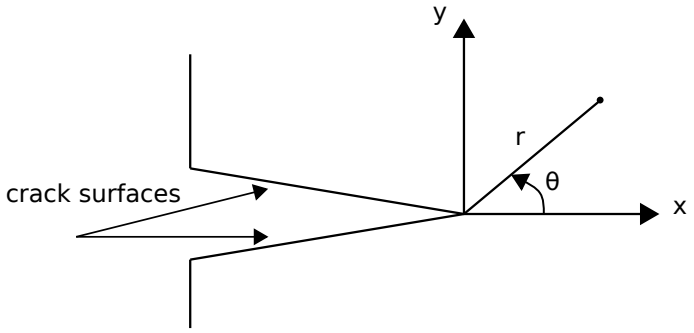

Figure 1.2: Coordinate system around a crack tip.

$$
\begin{aligned}
K_I &= \lim_{r\to 0}\sqrt{2\pi r}\sigma_{22}(\theta=0) = \lim_{r\to 0}\frac{\mu}{k+1}\sqrt{\frac{2\pi}{r}}[\![u_2(\theta=\pi)]\!] \\
K_{II} &= \lim_{r\to 0}\sqrt{2\pi r}\sigma_{12}(\theta=0) = \lim_{r\to 0}\frac{\mu}{k+1}\sqrt{\frac{2\pi}{r}}[\![u_1(\theta=\pi)]\!] \\
K_{III} &= \lim_{r\to 0}\sqrt{2\pi r}\sigma_{23}(\theta=0) = \lim_{r\to 0}\frac{\mu}{4}\sqrt{\frac{2\pi}{r}}[\![u_3(\theta=\pi)]\!]
\end{aligned}
\tag{1.3}
$$

where the operator $[\![.]\!]$ describes the limiting values of a given quantity on both edges of the discontinuity, $\mu = \frac{E}{1+\nu}$ and k the Kolosov constant, given by:

$$
k = \begin{cases} 3-4\nu & \text{for plane strain} \\ \frac{3-\nu}{1+\nu} & \text{for plane stress} \end{cases}
\tag{1.4}
$$

The asymptotic crack tip solutions have been revealed to be quite accurate and sufficient to describe fracture processes in linear elastic materials. For a better understanding of the amount of energy released during crack propagation, the energetic approach is adopted.

1.3.2 Energetic approach

As its name may suggest, the energetic approach is based on the energy balance of a cracked system. This global formulation represents the foundation of fracture mechanics and has been introduced by Griffith [GRI 21]. He postulated that when creating new cracked surfaces, energy is consumed. For slow crack growth, the decrease in the total potential energy of the structure due to an increase of the fracture surface area corresponds to the energy release rate G:

$$
G = -\frac{d\Pi}{dA}
\tag{1.5}
$$

where

$$
\Pi = E_{elas} - \Phi
\tag{1.6}
$$

Π is the potential energy, E_{elas} the strain energy and Φ represents the potential energy of external forces.

A relation between the stress intensity factors and the strain energy release rate has been established. For a crack subjected to mixed mode loading, the energy G is defined:

$$G = \frac{1}{E^*}(K_I^2 + K_{II}^2) + \frac{1+\nu}{E}K_{III}^2 \tag{1.7}$$

where E^* is related to the Young modulus and Poisson ratio:

$$E^* = \begin{cases} \frac{E}{1-\nu^2} & \text{for 3D and 2D plane strain} \\ E & \text{for 2D plane stress} \end{cases} \tag{1.8}$$

That same energy can also be evaluated using the J-integral. This new strain energy release rate concept and its pertaining equation were developed in the work of Cherepanov [CHE 67] and Rice [RIC 68]. Besides its application in LEFM, it can also be employed in the nonlinear elastic analysis, as long as the structure is subjected to a static or quasi-static loading.

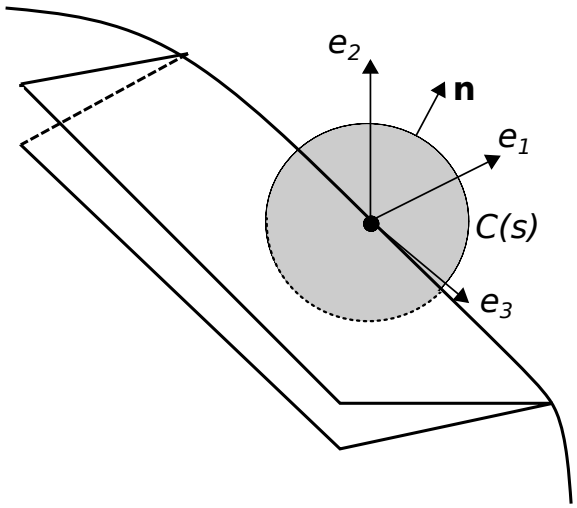

Figure 1.3: The J-contour integral *C(s)*

For a 3D crack front (cf. FIG.1.3), the general form of the J-integral near the crack tip is expressed as:

$$J(s) = \lim_{C\to 0}\int_{C(s)} (W\delta_{1i} - \sigma_{ij}u_{j,1})n_i d\Gamma \tag{1.9}$$

where $W = \int_0^{\varepsilon_{ij}} \sigma_{ij} d\varepsilon_{ij}$ is the strain energy density, σ_{ij} are the components of the Cauchy stress tensor, ε_{ij} the components of the strain tensor and u_i the displacement vector components. n_j is the normal vector to the J-integral contour $C(s)$.

The J-integral is extensively used in numerical models, to evaluate the energy release rate around the crack tip. Furthermore, many cracking criteria rely upon this integral value to predict crack initiation.

1.3.3 Dynamic fracture mechanics

Dynamic fracture mechanics deal with fracture processes for which the material inertia is substantial. These inertial effects originate either from an impact loading on a cracked structure or from rapidly moving cracks.

Mott [MOT 48] was the first physicist to investigate fast cracks. He ascertained that for such dynamic crack propagation, the kinetic energy is to be accounted for on the energy balance equation. Later on, many studies emerged to review and formulate the exact and general concepts of the recent dynamic fracture mechanics [ATK 68, FRE 72, KAN 88]. One major purpose of these analytical developments is to determine the maximum crack speed. While Mott has found it to be equal to one-half of the shear wave speed, the analysis conducted by Freund disclosed a limiting speed of none other than the Rayleigh wave speed. In light of the established equation of motion, it has been postulated that the dynamic energy release rate is:

$$G_{dyn} = (1 - \frac{v}{C_r})G \tag{1.10}$$

where v is the crack velocity, C_r the Rayleigh wave speed and G the static energy release rate.

Similarly, dynamic stress intensity factors can be deduced from the static ones using the equations developed by Bui [BUI 77]:

$$K_j = f_j(\dot{a})K_j^{dyn} \tag{1.11}$$

For each fracture mode, f_j is defined as below:

$$\begin{aligned} f_i(\dot{a}) &= \frac{4\alpha_i\left(1-\alpha_2^2\right)}{(k+1)D(\dot{a})} \text{ with } i \in \{I, II\} \\ f_{III}(\dot{a}) &= \frac{1}{\alpha_2} \\ \alpha_i &= \sqrt{1-\left(\frac{\dot{a}}{C_i}\right)^2} \\ D(\dot{a}) &= 4\alpha_1\alpha_2 - \left(1+\alpha_2^2\right)^2 \end{aligned} \tag{1.12}$$

where C_1 and C_2 are respectively the longitudinal and the shear wave velocity. D is the function whose zero verifies the Rayleigh wave velocity C_r.

1.3.4 Fracture criteria

For some materials, the complexity of the stress and the strain field ahead of the crack hinders researchers from an accurate estimation of the crack growth rate. In order to overcome the lack of knowledge of the overall physical mechanisms occurring in the process zone, many fracture criteria have been put forth. They are mainly based on the concept of the stress intensity factor and the energy release rate. The suitability of one or the inadequacy of the other is intrinsically reliant on some of the processes observed experimentally. According to the type of the problem, static or dynamic, crack initiation occurs once the stress intensity factors or the energy release rate attains a critical value:

$$K = K_c \qquad \text{or} \qquad G = G_c \tag{1.13}$$

In this section, we outline the most common criteria used for linear elastic materials. The same criterion is considered for both crack initiation and propagation.

— **The maximum tangential stress criteria** [ERD 63]: it applies for cracks under mixed-mode loading and where mode III is assumed to have no influence on its propagation. Herein, the near-crack-tip stress field is evaluated using polar coordinates:

$$\begin{aligned} \sigma_{\theta\theta} &= \frac{1}{\sqrt{2\pi r}} \cos\frac{1}{2}\theta[K_I \cos^2\frac{1}{2}\theta - \frac{3}{2}K_{II}\sin\theta] \\ \tau_{r\theta} &= \frac{1}{\sqrt{2\pi r}} \cos\frac{1}{2}\theta[K_I \sin\theta + K_{II}(3\cos\theta - 1)]. \end{aligned} \tag{1.14}$$

The direction of propagation is deduced by solving either for the maximum circumferential stress $\frac{\partial \sigma_{\theta\theta}}{\partial \theta}\Big|_{\theta=\theta_c} = 0$ or for a null shear stress $\tau_{r\theta} = 0$. The propagation angle denoted θ_c, is found as a function of the stress intensity factors:

$$\theta_c = 2\arctan\left(\frac{K_I - \sqrt{K_1^2 + 8K_{II}^2}}{4K_{II}}\right). \tag{1.15}$$

— **The minimum strain energy density criteria** [SIH 74]: using this local criterion implies that cracks will grow in the region of the least strain energy density factor S(θ). This strain energy is evaluated in the vicinity of the crack and can be defined as follows:

$$S(\theta) = a_{11}K_I^2 + 2a_{12}K_IK_{II} + a_{22}K_{II}^2 + a_{33}K_{III}^2 \tag{1.16}$$

with

$$a_{11} = \frac{1}{\sqrt{16\pi\mu}}(3-4\nu-\cos\theta)(1+cos\theta)$$
$$a_{12} = \frac{1}{\sqrt{8\pi\mu}}\sin\theta(\cos\theta-1+2\nu)$$
$$a_{22} = \frac{1}{\sqrt{16\pi\mu}}[4(1-\nu)(1-\cos\theta)+(3\cos\theta-1)(1+\cos\theta)]$$
$$a_{33} = \frac{1}{4\pi\mu}$$

The angle of propagation θ_c is obtained by satisfying the conditions:

$$\frac{\partial S(\theta)}{\partial\theta}\Big|_{\theta=\theta_c} = 0 \qquad \text{and} \qquad \frac{\partial^2 S(\theta)}{\partial\theta^2}\Big|_{\theta=\theta_c} > 0. \tag{1.17}$$

— **The maximum energy release rate criteria** [WU 78]: this criterion relies on Griffith principle but it can also be viewed as its extension since it enables the prediction of the crack growth directions. Its gist postulates that the crack will propagate in the direction that maximizes its energy. Based on Irwin formulation of the energy release rate as a function of the stress intensity factors (1.7), the crack angle θ_c is determined by fulfilling the two conditions:

$$\frac{\partial G}{\partial\theta}\Big|_{\theta=\theta_c} = 0 \qquad \text{and} \qquad \frac{\partial^2 G}{\partial\theta^2}\Big|_{\theta=\theta_c} < 0 \tag{1.18}$$

— **The local symmetry $K_{II} = 0$ criteria** [GOL 74]: it asserts that cracks will propagate in the direction where the condition $K_{II} = 0$ is satisfied.

1.4 Conclusion

This chapter outlined the general concepts of fracture mechanics, more particularly the linear elastic dynamic fracture. It also presented a survey of the main crack propagation criteria, which are much broader given the numerous loading configurations. The asymptotic fields and the energy release rate are well identified and provide satisfactory results when used for slow crack motions. However, in dynamics, they are set to depend on the crack velocity whose variation remains uncertain. For the most part, numerical models constrain crack speeds to propagate below C_r. Such observations should be recovered numerically as the studied material response to the applied loading.

Monocrystalline silicon undergoes cleavage fracture, which is the most brittle form of failure. Furthermore, cracks propagating on the cleavage plane grow at a rate close to the Rayleigh wave speed. For such crystalline materials, an appropriate criterion that considers the material anisotropy would be more accurate in predicting the crystallographic cracking plane and the crack velocity.

Chapter 2

Overview of explicit computational methods for dynamic brittle fracture

Contents

2.1 Introduction

In this chapter, an overview of different Finite Element (FE) models as well as non-FE models for dynamic crack propagation is considered. The prediction of fracture in brittle materials has been the subject of many analytical, experimental and numerical studies. On this basis, numerous numerical methods have been developed to tackle this issue and provide an insight into the physical processes that govern the rapidly moving cracks. The main focus of our study is to recall the most prevailing numerical approaches to solve fracture problems using an explicit time integration algorithm. Throughout this review, some of their models are introduced and their latest developments and limitations are discussed. Among the different methods, we distinguish those relying on a discrete representation of the crack namely, the eXtended Finite Element Method (XFEM) and the remeshing method. Others involve regularization techniques and a smeared representation of the crack such as phase field and cohesive zone models. Besides, there exist other techniques such as peridynamics, which alter the classical theory of continuum mechanics, and molecular dynamics that operate in the nano-scale domain.

2.2 Remeshing method

Since FE analysis is widely used to characterize structural components and simulate physical phenomena, modeling discontinuities using these standard finite elements seems convenient yet onerous. Researchers tried to adjust the continuous formulation of FE to apply it to a discrete problem. The remeshing technique [TRÄ 98] was among the first methods to be introduced in order to track moving cracks. In this chapter, we will give an insight into the two main categories of this technique. The first one is identified as the stationary mesh, it encompasses the node decoupling or the node splitting method [ALS 20]. This technique separates the elements that have reached a stress threshold. The nodes belonging to the split boundary are duplicated to create new free surfaces (cf. Fig. 2.1).

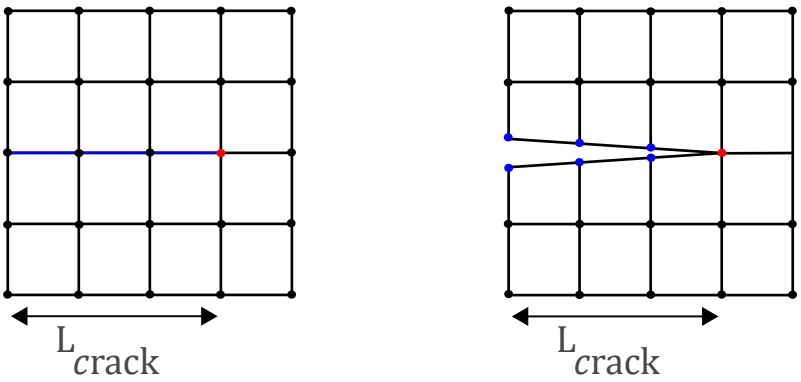

Figure 2.1: Nodes-splitting along crack propagation

However, it can be inferred from its principle that the crack is constrained to propagate only along the elements boundaries, thus entailing a prior knowledge of its path. Another method was suggested by Ingraffea et al. [ING 77], called node grafting, which essence relies on borrowing nodes from adjacent elements and grafting them near the new crack tip position, thus creating a discrete crack increment. For a moving mesh, once the criterion evaluated at the crack front is met, the structure mesh is altered by an extension *da* perceived as the crack advance. This technique was used by Bazant et al. [BAŽ 78] for elastodynamic problems.

Since these methods are embedded in the traditional finite element framework, combining them with an explicit time integration algorithm is straightforward and generally performed to account for dynamic fracture processes.

2.2.1 Explicit remeshing models

For stationary mesh procedures using explicit time integration schemes, it has been shown in the work of [ATL 85], that a sudden crack extension over a short period of time induces high-frequency oscillations. To remedy this issue, Keegstra et al. [KEE 76] and Yagawa et al. [YAG 77] have proposed models where the nodal decoupling occurring along crack propagation is performed gradually. This relaxation mechanism is characterized by its type, either linear or non-linear, and its release rate. While developing those methods [ATL 85], the strain energy release rate and the stress intensity factor have been evaluated, but the crack velocity has not been computed nor reported.

In the work of Song et al. [SON 09], a new cracking node method has been proposed where both node decoupling and XFEM are combined. To distinguish broken from unbroken elements, the discontinuous enrichment of XFEM is incorporated within the model (See Section 2.3). This method, embedded in an explicit time integration scheme, enables to track complex crack paths and has demonstrated good results in terms of fracture energy convergence. Also, for cracks subjected to high loading rates, their paths and velocities are consistent with those found experimentally. Nevertheless, this method has not been employed to quantify the velocities of accelerating cracks under quasi-static loading.

2.2.2 Advantages and limitations

While using this approach, it is conspicuous that the crack front and its propagation are inherently mesh-dependent. Remeshing after each propagation step can be tedious and time-consuming for large 3D structures. Therefore, automatic mesh generating was implemented to avoid performing this task manually [SHE 85, WAW 89]. It is also noteworthy that the more refined the mesh, the more accurate the crack geometry is depicted. To overcome this issue while avoiding massive models, the mesh can be locally

refined around the crack, so that the elements enduring failure are split into smaller ones. However, the changes affecting the finite element grid can be problematic when it comes to reassigning the previous stress and strain field to the newly generated mesh. Many studies have been performed to address this issue. For further details, refer to [DEB 96].

2.3 Extended Finite Element Method

In dynamic fracture modeling, the evolution of discontinuities in time has proven to be cumbersome when using a continuous representation of the physical parameters. To tackle this issue, several numerical methods have been developed within the FE analysis framework, among which the eXtended Finite Element Method (XFEM) is a highly evolved method. The XFEM was first introduced by Belytschko [BEL 99] and Moës [MOË 99] and stemmed from the partition of unity method developed by Melenk and Babuŝka [MEL 96]. The basic idea of this approach is to represent the local discontinuities by introducing new enriched shape functions in the standard displacement approximation (cf. Eq. (2.1)). Hence, an explicit representation of cracks can be performed independently of the structure (cf. Fig. 2.2). The approximate displacement field **u(x)** is expressed as :

$$\mathbf{u}(\mathbf{x}) = \sum_{i \in \mathcal{N}} \mathbf{u}_i \phi_i(\mathbf{x}) + \sum_{j \in \mathcal{N}_H} H(\mathbf{x}) \phi_j(\mathbf{x}) \mathbf{a}_{uj} + \sum_{k \in \mathcal{N}_\psi} \phi_k(\mathbf{x}) \sum_{l=1}^{4} \psi_\alpha \mathbf{b}_k^l \tag{2.1}$$

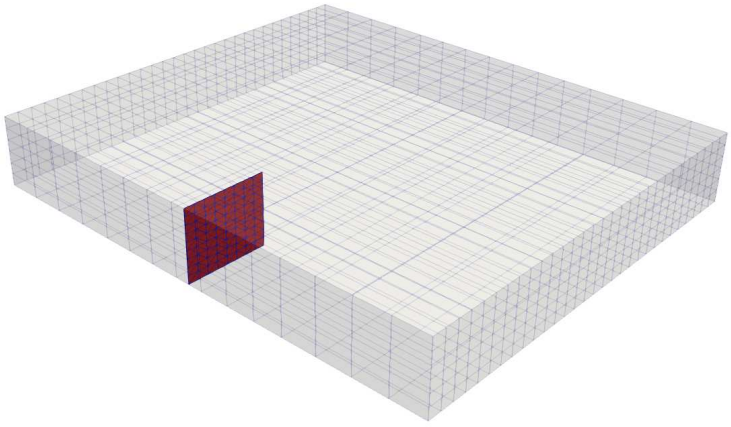

Figure 2.2: Representation of cracks using XFEM.

where $\mathcal{N}$ is the set of all the nodes contained in the mesh, Φ_i is the standard finite element shape function associated with node i and $\mathbf{u}_i$ are the standard degrees of freedom for the same node. As for the enriched part, $\mathbf{a}_{uj}$ describes the enriched degrees of freedom for

node j and is related to the discontinuous function H, whereas $\mathbf{b}_k^l$ are the enriched degrees of freedom for node k and associated to the singular function ψ_α.

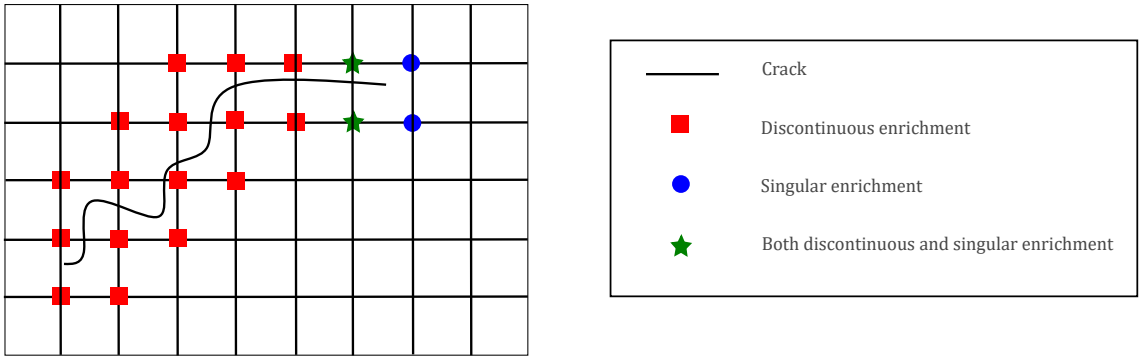

Figure 2.3: Enriched nodes in XFEM.

As introduced in the work of Belytschko et al. [BEL 01], the enriched functions include the Heaviside function H also referred to as the discontinuous field:

$$H(\mathbf{x}) = \begin{cases} +1 & \text{if } \mathbf{x} > 0 \\ -1 & \text{if } \mathbf{x} < 0 \end{cases} \tag{2.2}$$

This function can either solely or jointly be used with the near-tip asymptotic field or the singular field (cf. Fig. 2.3) whose function is described as:

$$\psi_\alpha(\mathbf{x}) = \sqrt{r}[\sin(\frac{\theta}{2}), \cos(\frac{\theta}{2}), \sin(\frac{\theta}{2})\sin(\theta), \cos(\frac{\theta}{2})\sin(\theta)] \tag{2.3}$$

where (r, θ) are polar coordinates centered at the crack tip. To portray an interface and follow its motion, Sethian et al. [SET 99, OSH 88] first proposed the level-sets technique. This method was subsequently used in XFEM, by Stolarska and Sukumar [STO 01, SUK 01] to represent crack paths along the structure. Its principle relies on defining a function over the calculation domain, whose value becomes zero at the interface intended to be described.

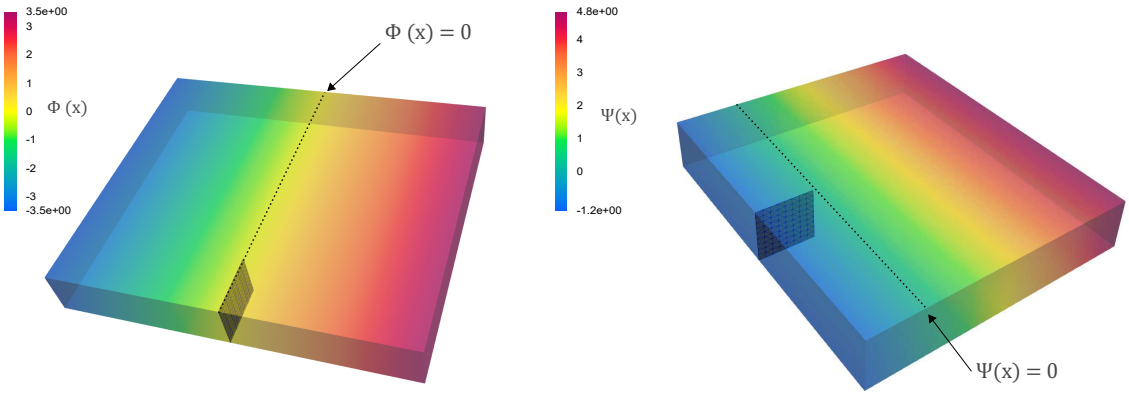

Figure 2.4: Level sets Φ and Ψ.

In the work of Moës et al. and Gravouil et al. [GRA 02], the use of level-sets was extended to three-dimensional structures. The combination of the two level-sets $\Phi(x)$ and $\Psi(x)$ has proved to be an efficient tool, able to define the crack front and its surface (cf. Fig. 2.4). For moving discontinuities, these latter are updated on the basis of a failure criterion without remeshing the structure. The level-set $\Phi(x)$ represents the signed distance function normal to the crack surface, while the level-set $\Psi(x)$ measures the signed distance function tangential to the crack surface and normal to the crack front. When combining the two, the crack front and the crack surface are located as follows:

$$\begin{aligned} \text{crack surface} &= \{\Phi(\mathbf{x}) = 0 \quad \textit{and} \quad \Psi(\mathbf{x}) < 0\} \\ \text{crack front} &= \{\Phi(\mathbf{x}) = 0 \quad \textit{and} \quad \Psi(\mathbf{x}) = 0\} \end{aligned} \tag{2.4}$$

And the two level-sets are assumed to be orthogonal:

$$\nabla\Phi(\mathbf{x}) \cdot \nabla\Psi(\mathbf{x}) = 0 \tag{2.5}$$

2.3.1 Explicit time integration with XFEM

Recently, problems involving very rapid crack growth have compelled researchers to use explicit time integration schemes and account for physical phenomena occurring along crack propagation. In XFEM, many studies were conducted to associate the fracture approach with the dynamic analysis, yet few have used explicit integration schemes. Belytschko et al. [BEL 03] were the first to raise the issue of the critical time step, inherent to explicit integration schemes. In fact, when the discontinuity approaches the element boundaries, the singular mass matrix terms can reach very small values hence generating critical time steps approaching zero. To overcome this issue, Hughes et al. [HUG 79] have proposed a quasi-explicit solver where the region containing the crack is solved by an implicit scheme while the rest of the structure was evaluated using an explicit analysis. This method was implemented in Abaqus [SMI 09] to remedy the

inability of the software to combine Abaqus Explicit and XFEM.

When using explicit schemes, a stability analysis should always be checked to avoid the growth of round-off errors that might impact the final answer. In some explicit numerical simulations, the stability is constrained by the value of the time step that should not exceed a critical value [COU 28]. Since this latter can be very small, it is common to go through a very large number of time steps to simulate a given phenomenon. In XFEM, this problem is overstated by the existence of cracked elements. The critical time step tends to zero once the crack reaches the element node. To prevent this issue, Menouillard et al. [MEN 08, MEN 06] have proposed an energy-based technique for lumping the mass matrix using discontinuous enrichment only. It prevents the time step from reaching null values, thus dealing with reasonable time steps during the numerical simulation. It was shown in his work, that the optimized critical time step in XFEM is of the same order of magnitude as the one computed for a standard finite element problem.

In the work conducted by Nistor et al. [NIS 06], an explicit analysis of bi-dimensional discontinuous structures under dynamic loading using XFEM, was implemented in a home-made code [NIS 05]. This 2D analysis was mainly conducted to evaluate the path-independent integral and has not been tested for propagating cracks. For 3D structures, Menouillard [MEN 07] implemented the XFEM formulation in the explicit code Europlexus to track crack propagation in split Hopkinson Pressure Bar. His approach focuses on using only one enrichment, the discontinuous enrichment, and has been revealed to be sufficient to guarantee a crack path close to the observed one experimentally. However, it is important to highlight that the aforementioned models were specially developed to simulate fracture problems involving dynamic loading. Consequently, the crack speeds are not evaluated since they are perceived as initial parameters that should be predefined when generating the model.

2.3.2 Advantages and limitations

XFEM overcomes the remeshing technique issues and enables the analysis of moving discontinuities within the finite element framework. Without altering the structure mesh, this approach is able to describe the crack paths with no prior knowledge. However, mass lumping remains an impediment to achieving a dynamic brittle fracture model using explicit XFEM. Many previous studies have addressed this matter [MEN 08, MEN 06, ROZ 08], yet the developed strategies only take into account the discontinuous enrichment, i.e. omitting the singular one. The absence of this latter compels the crack front to propagate inside an element, hence it is only detected when located on an element boundary. Such propagation may affect the velocity of the crack and constrain the model to an element-to-element propagation. Reducing the mesh size, might help overcome this issue in 2D structures, but remains an obstacle for cracks in 3D structures.

2.4 Cohesive Zone Model

The cohesive zone model (CZM) is a commonly used method to model crack propagation. It was first proposed by Dugdale [DUG 60] and Barenblatt [BAR 62] and its principle relies on defining a region along and ahead of the crack tip with interfacial cohesive surface elements. To characterize the interfacial fracture, two cohesive zone formulations might be used, either a potential-based model [NEE 87, FRE 08, PAR 09] or a non-potential-based model [ZHA 08, BOS 06]. The former model originated from the relationship between energies and the atomic separation of bimetallic interfaces [ROS 81] while the latter is an alternative model developed to account for the mixed-mode decohesion process. For both model types, a traction-separation law (TSL) is required to represent the softening behavior. This law dictates that the opening displacement will increase until the traction across the interface reaches a maximum cohesive strength σ_c, then it will diminish gradually up to a null cohesive strength to create traction-free crack surfaces. Numerous investigations have been carried out on shaping this law and among the prevailing ones, we distinguish the exponential form [XU 94, BOS 08], polynomial form [FRE 08, NEE 87], bilinear [YAH 18] and trilinear form [MOR 19], depicted schematically in FIG.2.5.

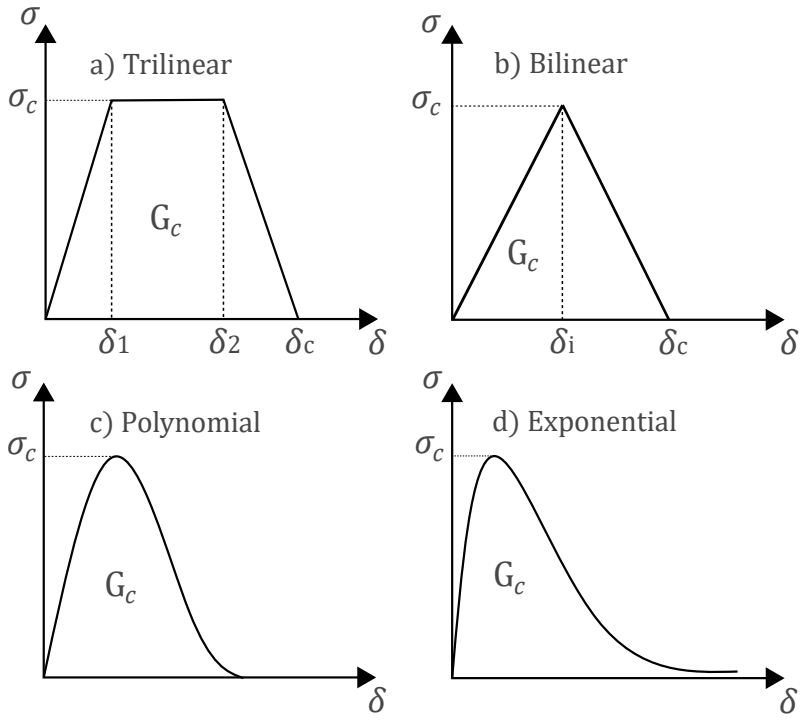

Figure 2.5: Traction-separation laws.

The opening of a bilinear cohesive zone model is illustrated in FIG.2.6 and the damage phases are delimited by the initial δ_i and the critical δ_c openings.

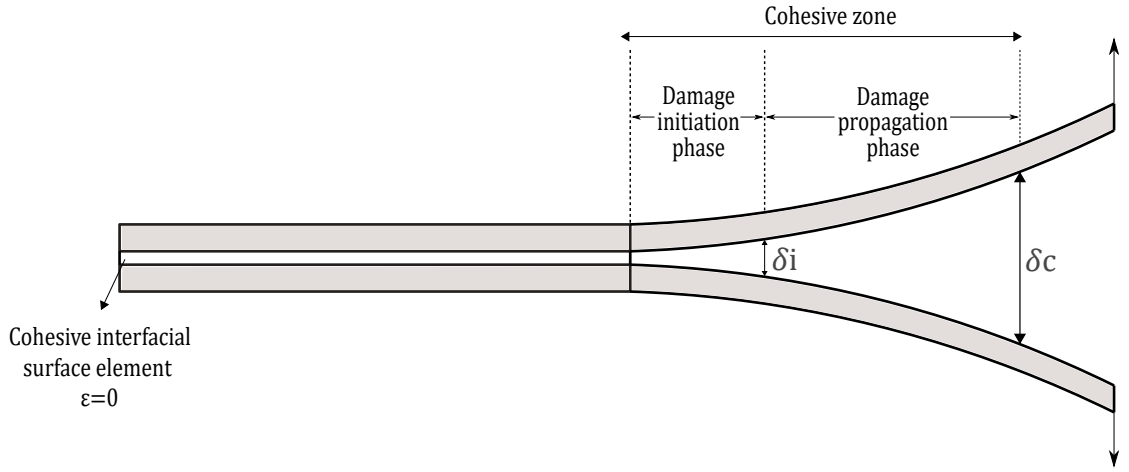

Figure 2.6: Schematic illustration of the cohesive zone model approach.

In structural mechanics, the CZM approach is associated with finite element analysis. The elements are governed by the traction-separation law, which links the cohesive traction vector to the displacement separation vector acting across the cohesive surfaces. For any type of TSL, CZM can either be described as intrinsic or extrinsic [ZHA 08, KUB 03] (cf. Fig. 2.7). With intrinsic models, the TSL curve comprises two parts: an elastic part (from the origin to the maximum cohesive strength) which denotes an increasing resistance of the cohesive surface to separation and a softening part (from maximum cohesive strength to zero) describing the failure process. For their numerical implementation, intrinsic CZM is initially incorporated before the simulation. The integration of the cohesive interfaces within the structure can be performed partially (in a particular zone of the studied mesh) or completely (inserting CZM over all the meshes interfaces). Such models are used in many industrial software such as Abaqus [SMI 09] or Castem [HOF 78] where cohesive elements are only inserted over selected zones (assumed to be the zones where damage and crack will occur). When the crack path is not known a priori, the intrinsic CZM can be pre-inserted over all the finite elements interfaces as implemented in Zebulon [MIS 11], LMGC90 [DUB 13] or Xper [PER 10] so that the crack path will emerge according to the loading intensity and history. However, the global elasticity of the structure is pathologically affected by the presence of the initial cohesive stiffness in the elastic part (the so-called inherent artificial compliance denoted C_0). One has so to suitably calibrate the cohesive stiffness following an adequate criterion [BLA 12]. As regards extrinsic CZM, the failure process is solely described. Therefore, the cohesive zone elements are adaptively incorporated on-the-fly once the elements along the crack path attain the cohesive strength. Contrary to intrinsic CZM, pathological stiffness loss is not met for extrinsic models. However, the numerical implementation of extrinsic CZM

can become highly cumbersome. Apart from needing special treatment, particularly for parallelization, such models can suffer from the time discontinuity issue when computing the stress fields.

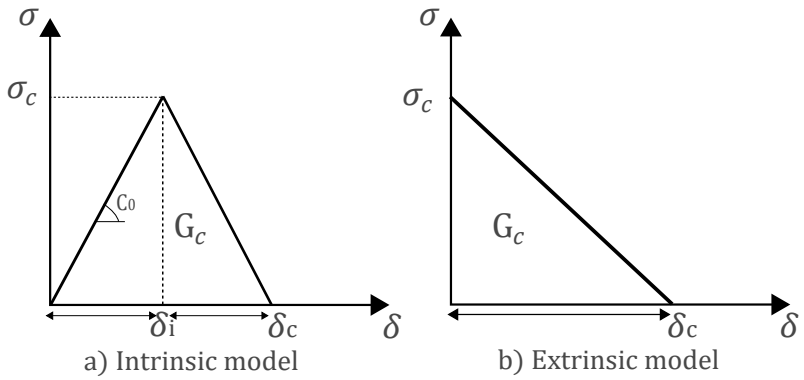

Figure 2.7: Intrinsic and extrinsic models of cohesive fracture

2.4.1 Explicit Cohesive Zone Models

Initially, the CZM was applied to study the yielding of steel sheets [DUG 60] and was later developed to evaluate brittle fracture in beams made of concrete [HIL 76]. Over the years, this model was expanded to cover a wider range of materials and it has also been improved to address different types of failure. For the dynamic brittle fracture phenomenon, a rate-dependent cohesive model able to reproduce experimental crack velocities was established [SAM 02]. Zhou et al. [ZHO 05] introduced a microscopic rate-dependent cohesive law along the crack tip process zone :

$$t_{\text{eff}} = t_{\text{eff}}(\delta_{\text{eff}}, \dot{\delta}_{\text{eff}}) \tag{2.6}$$

where the cohesive strength t_{eff} is related to the effective displacement of cohesive surfaces δ_{eff} and the opening speed $\dot{\delta}_{\text{eff}}$. The generalized equation defining the critical crack opening displacement is given by :

$$\delta_{\text{c}} = \delta_{\text{co}} \left[1 + \left(\frac{\dot{\delta}_{\text{eff}}}{\dot{\delta}_0} \right)^n \right] \tag{2.7}$$

where $\dot{\delta}_0$ is the scaling crack opening rate, n the index of rate-dependency and δ_{co} the static value of critical crack opening distance. This cohesive law was implemented within an explicit dynamic FE framework, where the equation of motion is integrated using an explicit Newmark scheme. A suitable choice of the cohesive settings such as the index of rate-dependency n and the scaling crack opening rate $\dot{\delta}_0$ showed that this law can accurately assess the crack velocity, thus reproducing the experimental observations [FIN 99].

In that same context, Doyen et al. [DOY 13] proposed a quasi-explicit time-integration scheme with a rate-dependent CZM to predict the velocity of rapidly moving cracks in brittle materials. In this model, the displacement of the nodes outside of the cohesive region was computed using a finite difference method (explicit) whereas the displacement of the nodes within the cohesive zone was solved by an implicit scheme. Although the computed crack tip speed is in accordance with the values obtained using other established cohesive zone models, the three-dimensional mechanisms have been disregarded and are to be taken into account in the future.

2.4.2 Advantages and limitations

The cohesive zone model has always been used as a predictive approach to fracture. It has been shown in the work of Elices et al. [ELI 02] that the outcomes of CZM computations match those observed or measured experimentally for numerous materials, ductile or brittle as well as for cracked or uncracked structures. Nevertheless, the CZM approach has proved to be mesh dependent [TIJ 00], i.e. the size of the elements within the cohesive region can influence the FEM results. To overcome the mesh density dependency, an artificial compliance was introduced in the traction-separation law for intrinsic models, without altering the overall elastic response [BLA 12]. Besides, the CZM inherently exhibits instabilities, also called solution jumps. It arises from the system storing more energy than what can be released through the cohesive zone. Chaboche et al. [CHA 01] circumvented this problem by using CZM that incorporates a viscous regularisation. For dynamic brittle fracture, it has been observed that most CZM utilize rate-dependent TSL to take into account the complicated mechanisms occurring in the process zone. Furthermore, the shape of the TSL is shown to have an impact on the material response [SCH 03]. Hence, one must select the TSL law according to convenience. Many other parameters, mentioned above, are to be chosen so that the numerical model achieves the best fit possible with experimental measures [RIC 12].

2.5 Phase Field

Phase-field (PF) is a widely used approach that can address fracture problems when combined with the finite element computational method. More broadly, it belongs to the extensive family of non-local damage models. The PF technique for dynamic brittle fracture is based on the variational formulation of Francfort, Marigo and Bourdin [BOU 08]. The PH approach overcomes some of Griffith theory limitations by enabling the depiction of complex crack geometries and crack branching. The key point of this technique is to use a smeared representation of the discontinuity. The PF models, sometimes referred to as smeared crack models, are governed by a continuous field variable, s, associated with a regularization length, l, which describes the smooth transition from an undamaged material state to a fully broken state [BOU 00] (cf. Fig. 2.8).

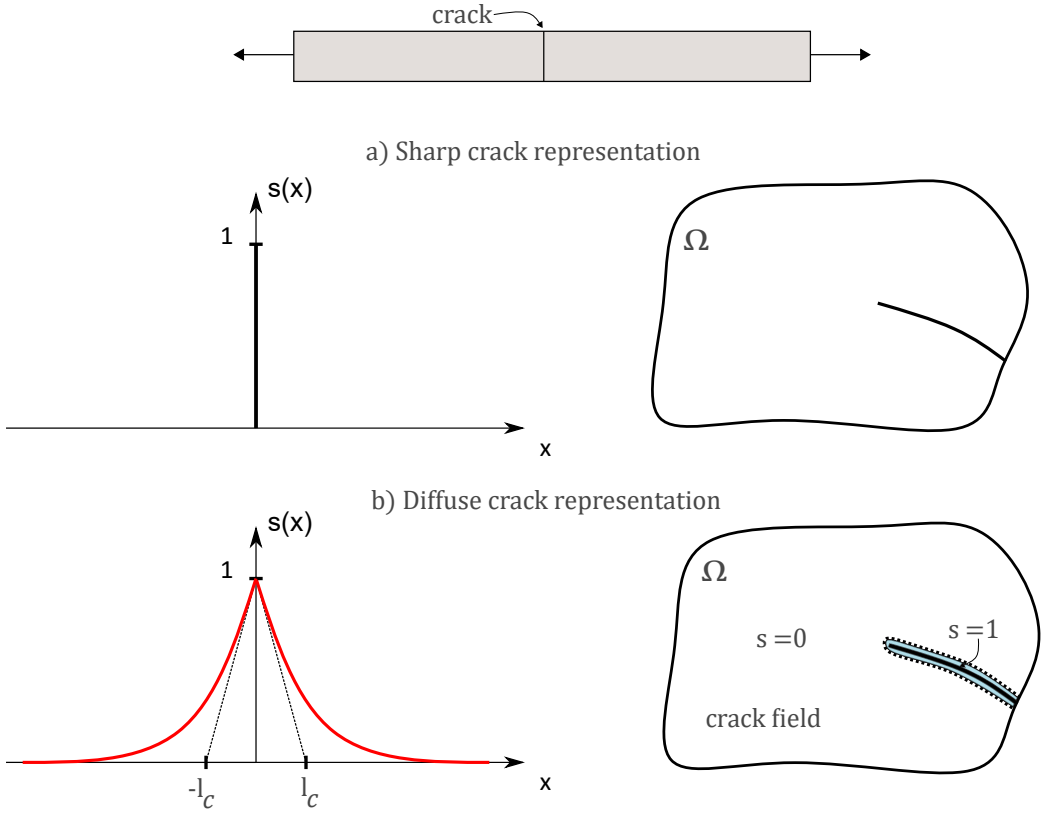

Figure 2.8: Phase-field representation of a crack topology.

To describe the fracture surface Γ, a phase-field function is introduced :

$$\Gamma(s) = \int_{\Omega} (\frac{s^2}{2l} + \frac{l}{2} \nabla s \cdot \nabla s) dV = \int_{\Omega} \gamma(s, \nabla s) dV \tag{2.8}$$

where γ is the fracture surface density. In this approach, two partial differential equations are solved: one related to the displacement field and the other one to the damage problem referred to as the crack phase-field. For dynamic brittle fracture, the phase-field governing equations for both problems are stated as below:

$$\rho \ddot{\mathbf{u}} = \nabla \cdot \sigma + \mathbf{f} \tag{2.9}$$

$$g_c(s^2 - l^2 \nabla^2 s) = 2l(1-s) \tag{2.10}$$

where g_c the surface energy needed to create a unit fracture surface. Using a non-linear elastic constitutive model, either quasi-static or dynamic, the displacement field is computed using the minimization problem of the energy functional [FRA 98]. This energy involves the Lagrangian of the two fields [MOL 20] and is defined as below:

$$\mathcal{L} = D(\dot{\mathbf{u}}) - \Pi(\mathbf{u}, s) \tag{2.11}$$

where $D(\dot{\mathbf{u}})$ is the kinetic energy and $\Pi(\mathbf{u},s)$ the potential energy. This latter consists of the elastic strain energy $E(\mathbf{u},s)$ and the fracture energy $W(s)$:

$$\Pi(\mathbf{u},s) = E(\mathbf{u},s) + W(s) \tag{2.12}$$

The preceding evolution equations, (2.9) and (2.10), are solved using one of the two existing solver techniques: the monolithic algorithm [MIE 10] where the displacement and the damage field are computed simultaneously, or the staggered algorithm [MOL 17] where they are computed independently.

2.5.1 Explicit phase-field

In most of the phase-field developments, the damage problem is solved using implicit schemes for phase field governing equation (cf. Eq. (2.10)). In the work of Miehe et al. [MIE 10], a time-regularized viscous crack propagation model has been proposed. The main objective behind adding this artificial regularization term η is to ensure the viscous dissipation of the PF. In the available literature, most of the explicit PF models solve the crack problem using this evolution equation as an explicit PF governing equation:

$$\dot{s} - \frac{1}{\eta}\left\langle \beta - \frac{g_c}{l}s \right\rangle_+ = 0 \tag{2.13}$$

where β is the local driving force field and η the viscous artificial regularization term. Through this equation, Miehe et al. [MIE 10] asserted that the evolution of the damage variable depends on the difference between the local driving force field and the geometric crack resistance. Other works were recently carried out to derive an equation of motion for the phase-field variable. In [KUH 08], Kuhn and Muller suggested an equation similar to the time-dependent Ginzburg-Landau equation:

$$\frac{1}{M}\dot{s} + 2sW(\varepsilon) - g_c\left(2\varepsilon\Delta s + \frac{1-s}{2\varepsilon}\right) = 0 \tag{2.14}$$

where s is the PF damage variable, M is a parameter controlling the rate at which local damage information diffuses into the bulk material, ε is a length scale over which cracks are smoothed, g_c is the fracture energy, W the undamaged strain energy functional and ε is the linearized strain. From a mathematical point of view, this latter equation was optimized in the work of Kamensky et al. [KAM 18] by adding a second time derivative of the damage field, referred to as the microscopic inertia term, into the equation:

$$\frac{1}{M}\dot{s} + \frac{2g_c\varepsilon}{c^2}\ddot{s} + 2sW(\varepsilon) - g_c\left(2\varepsilon\Delta s + \frac{1-s}{2\varepsilon}\right) = 0 \tag{2.15}$$

This additional term comprises the parameter c which is the speed limit on the propagation of the phase field through the undamaged material. For further details, refer to [KAM 18].

Explicit solvers of PF models have been applied partially [REN 19] or thoroughly [ZHA 21b, WAN 19c, ZHA 21a, WAN 20]. In the work of Ren et al. [REN 19], the model uses a staggered algorithm where the displacement field is solved explicitly using the Verlet-velocity integration scheme while the PF damage variable is solved implicitly. Other models [ZHA 21b, WAN 19c, ZHA 21a, WAN 20] employ an explicit time integration procedure for both the displacement and the PF problem. They are solved using explicit finite difference methods: central difference scheme and forward difference scheme, respectively. The latter models were mainly used to investigate failure in composite materials [ZHA 21b, ZHA 21a], thermo-elastic materials [WAN 20] or materials with compressive-shear failure behavior [WAN 19c].

2.5.2 Advantages and limitations

Recently, the phase-field model has been increasingly used due to its various advantages. Several works were able to capture some of the brittle fracture attributes such as crack branching. Dynamic PF models were also capable of achieving crack velocities up to 60% of Rayleigh wave speed Cr. The challenge behind the use of an explicit form of the crack PF and solving it explicitly, is the computational expense associated with small critical time steps. Hu et al. [HU 21] suggested a precise integration scheme (PIS) using higher time intervals than the ones used with finite difference method. This modification could overcome high computational costs without inducing divergence and numerical discrepancies. In the model developed by Wang [WAN 20], the dynamic processes such as crack branching are being captured and the crack speed (not greater than 20% of Rayleigh wave speed Cr) demonstrates good consistency with his experimental data. However, the method has not yet been employed for configurations and materials exhibiting rapidly moving cracks, approaching 80% of Cr. Besides, the need for a viscosity parameter to achieve convergence still raises a lot of questions. Since this parameter has no direct physical meaning, a parametric study is required to select its optimal values.

2.6 Peridynamics

Peridynamics (PD) is a continuum theory developed by Silling [SIL 00]. It consists in replacing the partial differential equations with integral equations. The overriding concern behind its development was to overcome the issues encountered in the classical continuum formulation when handling strong material discontinuities such as fracture. As an attempt to address brittle dynamic fracture problems, different numerical methods within the PD theory were developed. The most prevalent approach is the use of the meshfree scheme (EMU code) [SIL 05]. Other studies were conducted to incorporate this theory within the standard Finite Element framework since it is widely used for structural analysis [MAC 07]. As its name suggests, peridynamics is governed by a non-local interaction zone called horizon (Peri in Greek). As depicted in Fig. 2.9, the model is treated as a set

of material points separated by a finite distance ξ. The length parameter, $H(X)$, specifies the region inside which the material points interact and influence each other. A uniform grid spacing specifies the resolution of the network, whether it is coarse or refined.

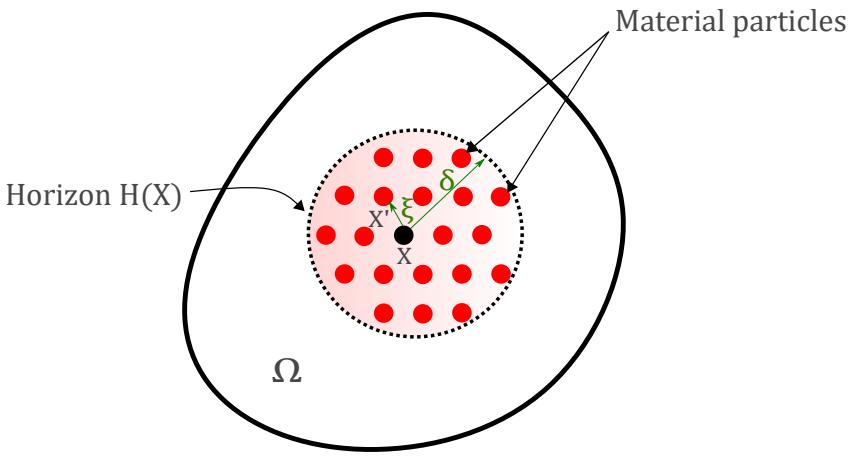

Figure 2.9: Schematic illustration of the peridynamic material particles.

Also, for each pair of points, an elastic bond either linear or non-linear is introduced to account for their connection and mutual interaction while ensuring the material consistency. The singular feature of those elastic bonds is their critical relative elongation, denoted η, beyond which the bond is considered broken and its contribution to the interaction becomes null (cf. Fig. 2.10). This parameter depends on the studied material and its energy release rate [SIL 05].

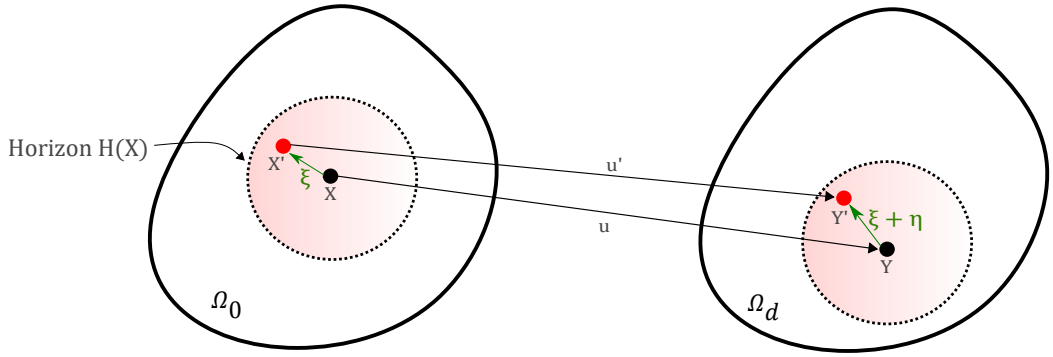

Figure 2.10: Peridynamic model: undeformed and deformed configurations

Upon the PD principle, it can be inferred that the predefined limit η governs the damage evolution. This bond-failure criteria is then self-sufficient to handle the dynamics behind crack propagation. Therefore, it goes without saying that no additional criteria is

needed to regulate cracks speeds or crack branching.
Among the PD theory, it is noteworthy to distinguish two different approaches. Based on the definition of the interaction forces, there exists a bond-based and a state-based peridynamics. In the first approach [HA 10], the interaction forces between two material points are solely determined by their relative displacements, while in the second [SIL 07], they are function of the deformations of all the materials points within the horizon and sometimes they do depend on other variables.

2.6.1 Explicit Peridynamic formulation

The PD equation of motion based on the original formulation [SIL 00] is solved for material points belonging to the horizon and is given by:

$$\rho\ddot{\mathbf{u}}(\mathbf{x},t) = \int_H \mathbf{f}\left(\mathbf{u}\left(\mathbf{x}',t\right) - \mathbf{u}(\mathbf{x},t), \mathbf{x}' - \mathbf{x}\right) \mathrm{d}V_{\mathbf{x}'} + \mathbf{b}(\mathbf{x},t) \tag{2.16}$$

where f is the pairwise force function that the particle $\mathbf{x}'$ exerts on the particle $\mathbf{x}$, $\mathbf{u}$ the displacement field and $\mathbf{b}$ is the body force. The integral is evaluated over a region H denoting the horizon.

The solution process is computed by means of a numerical technique implementing the PD problem. Although the meshfree method is frequently used, we will be focusing on the recent developments entailing the finite element analysis. In [MAC 07], the grid nodal points are assimilated to an assembly of truss elements, where their stiffness properties characterize the PD bonds. To depict the dynamic processes arising from brittle fracture and the system response upon the sequential breaking of bonds, we will outline the PD models using an explicit time integration scheme.

The most used time integration scheme is the Velocity-verlet algorithms also known as the mid-point integration. For each step, the acceleration is solved directly from the equation of motion defined in (2.16) and its value is used to assess the future state of the system. Through the application of the governing PD equation, the damage law is checked for each bond to determine the current state of damage.

To study the dynamic crack branching in brittle materials, Ha et al. [HA 10] performed a 2D PD simulation. For his numerical model, the meshfree method was used and the convergence of the method was checked regarding the size of the horizon and the grid spacing. The obtained results demonstrate a crack speed and branching patterns in great agreement with the experimental observations reported in [BOW 67]. However, when combining PD to finite element analysis, few works have been performed on dynamic brittle fracture. A state-based PD analysis was recently developed within the finite element framework [MAD 18], where the solution is achieved by conducting an implicit integration until crack initiation and then proceeding with an explicit algorithm. The crack propagation behavior in 3D fiber-reinforced composite (FRC) structures was inves-

tigated in the work of [ROK 18] and has shown that upon the loading conditions and the pre-existing defects, PD has prevailed in predicting crack paths.

2.6.2 Advantages and limitations

On numerous occasions, PD has proved to be efficient in terms of describing the complex dynamic patterns of cracks such as its branching. In addition to the main branches, this method is also capable of providing information about small branches. Therefore it fully recovers the crack features observed experimentally on some materials such as glass. However, some parameters within this formulation remain numerical and no physical explanation can be provided to vindicate their values. For instance, the horizon, which in reality is boundless, must be assigned a finite value. Quantifying its value can be cumbersome since it is believed to depend upon an intrinsic material length, characterizing the physics of interactions between particles [HA 10]. Consequently, the crack features, namely its speed and path, may vary significantly if different horizons are considered. In the work of Bobaru et al. [BOB 09], an adaptive refinement algorithm of the grid spacing and horizon was proposed. For 1D problems, this method has showed to achieve convergence to the classical solutions in the limit of the horizon going to zero [SIL 08].

2.7 Molecular Dynamics

Apprehending the features of dynamic brittle fracture has always been an abiding challenge. As mentioned before, many theories have arised to elucidate the discrepancy between theoretical and experimental results. One of the established observations is that the cracks will accelerate up to a critical speed lower than the Rayleigh wave speed. This out-of-reach speed has been proved to be the theoretical limit [STR 57, KAN 88]. To explain this phenomenon, an assumption based on the existence of micro-scale dissipation mechanisms was made. Therefore, many molecular dynamics (MD) simulations have been employed to explore the movement of atoms and molecules and their behaviour after their bonds breakage. By introducing the lattice model, Slepyan [SLE 10] had shown the existence of waves originating from the micro-structural scale, which should be accounted for when treating fracture. Capturing this wave radiation should give a deep insight into the energy release process for a propagating crack, thus shedding some light on the macro-level phenomena observed. These 2D lattice models can be described as a set of particles connected to the nearest neighbors with linear elastic bonds that break after undergoing a given extension (cf. Fig. 2.11).

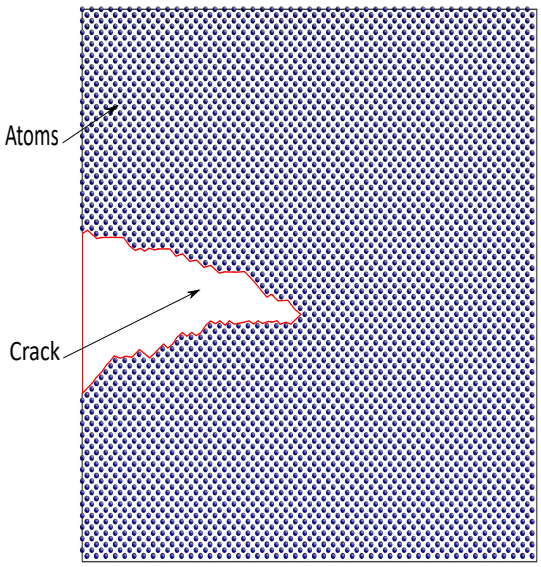

Figure 2.11: Schematic illustration of molecular dynamics simulation of crack growth.

When performing the computational analysis, MD simulations require the determination of the inter-atomic potentials. Those mathematical functions are derived from quantum mechanics described by Schrodinger equation [SCH 26]. For a given material, many approximations are needed and selecting one among others will depend on the level of quantum chemistry calculations and the experimental data. For structural analysis involving covalent systems, it is appropriate to use bound order potentials [ALB 02, PET 99] such as Tersoff potential [TER 88, TER 89, FAN 19] or EDIP potential [BAZ 97]. As regards single crystal silicon, a Stillinger-Weber (SW) potential is deemed more suitable [STI 85].

2.7.1 Applications to silicon fracture

In [HOL 98], Marder and Holland performed an MD simulation on single-crystal silicon to investigate the dynamics of crack propagation. In their work, they adopted an infinite strip geometry where a notch is inserted. For initiation, the two boundaries of the strip are pulled apart to store enough elastic energy ahead of the crack tip and initiate its propagation. The inter-atomic potential used in this case is the SW potential [STI 85]. The calculations were carried out in view of solving the equation of motion for all particles and Verlet algorithm was used for the time integration. The order of magnitude of the time step is few femtoseconds. Crack velocities were not evaluated in this study.

2.7.2 Advantages and limitations

From a qualitative point of view, MD portrays many microscopic processes such as lattice trapping and its effects on crack propagation. In the case of single-crystal silicon, it also allows a representation of crystallographic planes highlighting the anisotropy dependence of crack propagation. However, the high computational cost hinders us from considering 3D structures. Also, the strip geometry only represents a small portion of the matter. Its underlying parameters such as the periodic boundary conditions and the absorbing regions may bring us closer to reality yet disregard many key aspects. To illustrate this issue, we recall the assumptions that were made to justify the experimental observations and which involve scales of the size of the entire structure. The most relevant one asserts that the propagation of elastic waves and their reflection from the boundaries might have an impact on the crack velocity and its dynamics. Unfortunately, such hypothesis cannot be tested in MD simulations. Furthermore, it was observed in [HOL 98] that the used inter-atomic potential will not yield fracture along the experimentally preferred fracture planes of silicon. Since those potentials are perceived as approximations, they might omit some materials characteristics thus ensuing inconsistent results.

2.8 Conclusion

In this chapter, we provided a concise overview of some numerical approaches for dynamic brittle fracture. A detailed study of the modeling parameters has been performed to provide an insight on the requirements needed to capture the dynamic behavior of accelerating cracks. The majority of the aforementioned computational methods has shown promising results in terms of predicting singular crack paths. However, when handling complex geometries such as crack branching, some of the methods, namely peridynamics and phase-field, recovered the observed experimental patterns naturally, while others such as XFEM or the remeshing technique, relied upon a branching criterion to trigger this phenomena.

In view of crack speeds, very few studies were found to be addressing this matter. Mostly because its evolution along the crack path is intricately dependent upon micro-scale and macro-scale processes. Therefore, reproducing a realistic numerical model will utterly require a multi-scale approach.

Besides, it appears that many computational methods have introduced some numerical settings or length scales among their models, others have regulated their numerical parameters to experimental results in order to achieve great agreement with the measured data. As opposed to such models, we believe that an accurate estimation of the crack velocity should be recovered as a "natural" outcome of the numerical analysis or by giving a physical meaning to those parameters and linking them to the studied material intrinsic parameters.

Chapter 3

An XFEM model for dynamic crack propagation

Contents

3.1 Introduction

This chapter presents the step-by-step implementation plan of the explicit extended finite element method in Cast3m [CAS 21]. Although the alleged software is originally implicit, it consists of a toolbox that offers great freedom in terms of development and access to various modeling features. When simulating the dynamic behavior of cracks evolving in brittle materials, many numerical parameters are to be determined. Therefore, an exhaustive study was first conducted to establish the adequate numerical approach and its inherent settings. In the first part, the algorithm and procedures implemented in Cast3M are reported and the calculation methodology is outlined. In the second part, an example to predict dynamic crack propagation is presented. Eventually, the effect of some numerical parameters on the outcome and the performance of the computations is appraised.

3.2 Cast3m implementation of explicit extended finite element method

The strategy adopted by Cast3m consists in defining the model parameters such as mesh, loading type and XFEM settings. Thereafter, a temporal integration scheme is used to solve the mechanical problem. In fracture mechanics encompassing crack growth, an initiation criterion is constantly evaluated along the resolution process to account for the discontinuity movement. The general purpose of the following analysis is mainly to assess the newly implemented procedures and validate their suitability, robustness and adequacy once applied to our model. Also, this chapter is committed to providing short guidance on how to use and adapt this code for further applications.

3.2.1 Spatial discretization: Model parameters

In the experimental part of our study, we use pre-notched wafers of dimension 50mm x 50mm x 190μm and subjected to a quasi-static bending load (cf. FIG.3.1(a)). The post-mortem inspection of the crack surfaces has revealed that the front is elliptical and its shape evolves for different crack velocities (cf. FIG.3.1(b)). For the sake of comparison, it can be inferred that one of our model undeniable attributes is its three-dimensional configuration. It is of particular interest since we want our algorithm to cover a broad range of applications. Hence, be extended to problems with internal and through-thickness propagating cracks.

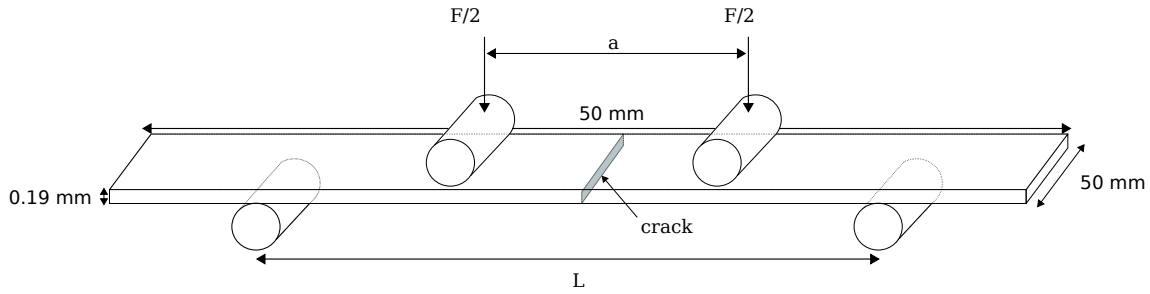

(a)

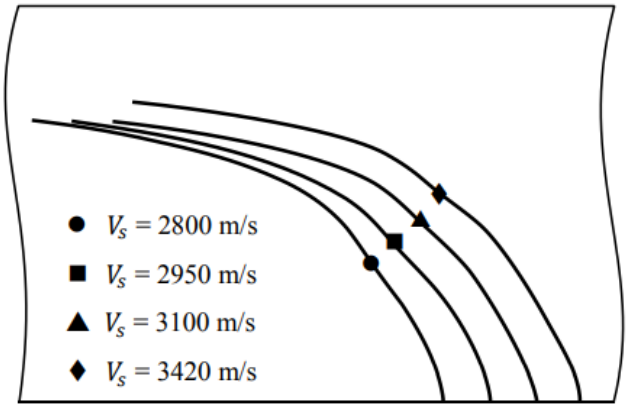

(b)

Figure 3.1: (a) Four-line bending test and (b) crack front shapes for different crack steady-state velocities [WAN 19b].

However, the small width of our wafers, compared to their other dimensions, can be cumbersome to represent numerically using a 3D model. If considering many elements through the thickness while preserving the quality of the mesh, our algorithm is bound to generate hundreds of thousands of elements. Such meshes would engender heavy computational costs. Furthermore, the small elements will strongly reduce the critical time step of the explicit integration scheme, which will be computed at a later stage.

3.2.1.1 Mesh model

To overcome the aforementioned issues, all the subsequent computations are performed on a simplified 3D model, roughly representative of the wafers geometry. The model is of dimension 6mm x 7mm x 1mm and is regularly meshed using linear hexahedral elements, referred to as CUB8 in Cast3m. As depicted in FIG.3.2, the structure is coarsely discretized, with 6 elements along the thickness and 30 elements along the crack trajectory. Additionally, two parts can be distinguished. A central zone, where the crack is intended to propagate, and whose elements are assigned the enrichment properties. It enables to

locate the elements cut by the crack, thus activating their additional degrees of freedom. As for the peripherals zones, they only include standard elements. A discrete representation of a sharp notch, which length is approximately 1.2 mm, is obtained using XFEM functions. Many conditions are to be fulfilled when including this discontinuity. The use of crack criteria based upon the J-integral requires specifying a domain or the elements layers along which it will be computed. Therefore, this compels the notch to go through at least 4 elements. Among the available enrichments (discontinuous and singular), only the discontinuous enrichment is considered. For crack tracking, level sets phi Φ and psi Ψ are used and updated after each crack extension to locate the new front.

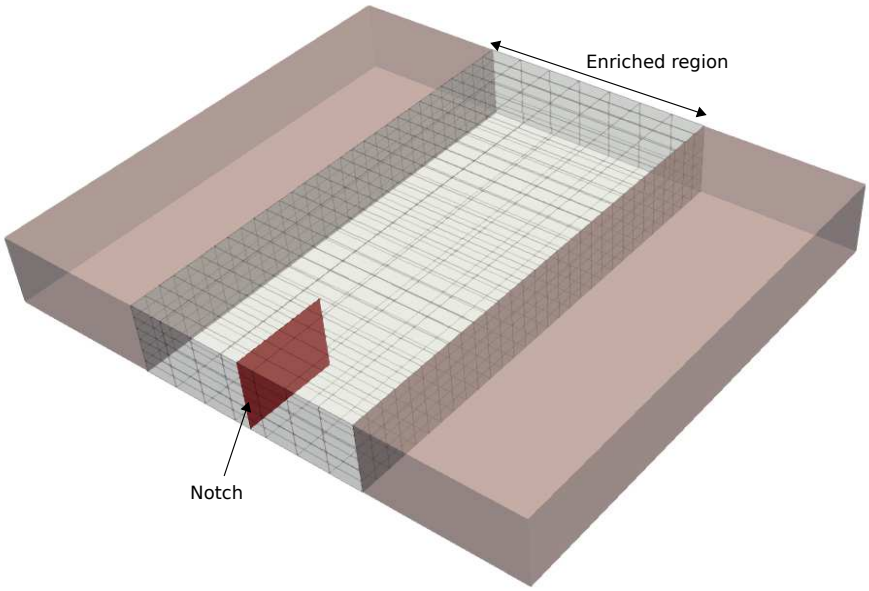

Figure 3.2: Extended Finite Element model for crack growth.

3.2.1.2 Material properties

Once the geometry is defined, the mechanical parameters have to be clearly stated to capture the brittle or ductile fracture behavior. In the course of our work, monocrystalline silicon, which is a very brittle material (cf. TAB.3.1), is considered. It is noteworthy to mention that it is an elastic material renowned for exhibiting orthotropic properties. Nevertheless, this feature is discarded in our calculations, which are carried on an isotropic material. This simplifying assumption avoids the complexity that would result from combining explicit XFEM with an orthotropic model.

Material properties	Units	Monocrystalline silicon (Si)
Density γ	$tons/mm^2$	$2{,}33.10^{-9}$
Young modulus E	MPa	130000
Poisson ratio	–	0,28
Fracture energy	mJ/mm^2	$1{,}73.10^{-3}$
Rayleigh wave speed	m/s	4600

Table 3.1: Mechanical and fracture properties in single-crystal silicon [MAS 13]

3.2.1.3 Mechanical loading

To underline the dynamic features of cracks in brittle solids, a constant force is applied and maintained constant along its propagation. Therefore, the impact of the loading type and its rate is neglected when evaluating crack dynamics. However, when considering the original undeformed mesh, progressive loading is to be applied in order to reach a constrained state, where cracks are about to initiate. Consequently, two mechanical loads are exerted alternatively: a linear load followed by a constant one (cf. FIG.3.3). The value of the latter is defined by the outcome of the former one. In Cast3m, for each loading type, an analysis is conducted. The formerly drawn distinction between the two applied loads will then lead to two separate analyses.

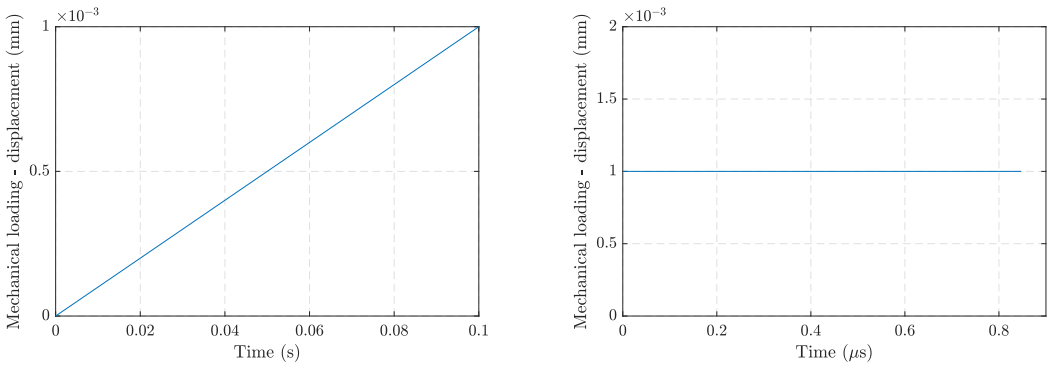

(a) (b)

Figure 3.3: (a) The progressive linear loading (first analysis) and (b) the constant loading (second analysis).

A linear quasi-static tensile loading is applied. As depicted in FIG.3.4, one edge of the sample undergoes a displacement of a few millimeters along x while the other extremity is maintained fixed by imposing a null displacement along x and no constraint along y and z. To replicate our experimental configuration, a bending test would have been more representative. However, given the shape of our wafers and the use of linear elements, it is more straightforward to go with a uniaxial tension configuration and avoid

any issue that may arise from bending non-linearities when implementing our algorithm.

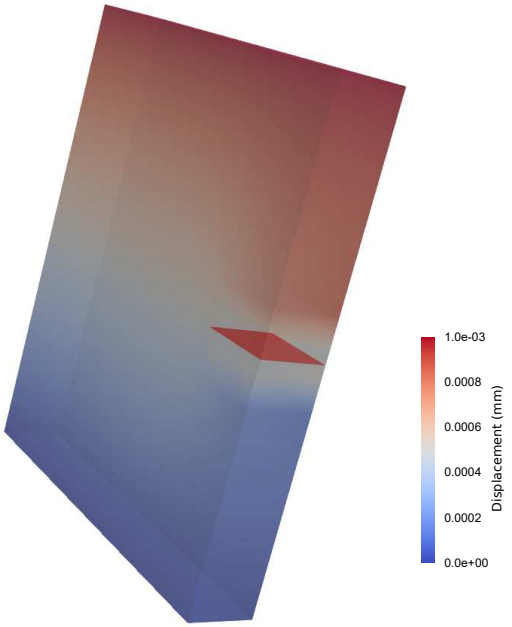

Figure 3.4: Finite element analysis of a plate subjected to a tensile loading (Mode I).

3.2.2 Temporal discretization

The main aim of our work is to shed light on dynamic processes associated with crack propagation on monocrystalline silicon. This dynamic fracture behavior stems from the rapidly moving cracks, reaching velocities close to the Rayleigh wave speed [FIN 99, WAN 19b]. Since failure occurs in a very short time, it is reasonable to approach this problem using an explicit time integration scheme. In the course of our work, dynamic calculations are performed simultaneously along crack propagation. Hence, the initiation criterion (either J-integral or stress intensity factors) is strongly conditional upon the computed fields ahead of the moving crack front.

For the purpose of reducing the computational cost, the first analysis (before the failure criterion is reached) is carried out using an implicit integration scheme. Only the second analysis involving crack propagation (once the crack onset criterion is verified) is solved explicitly.

3.2.2.1 Implicit calculations

Since it is a linear static analysis, an implicit solver in Cast3m, referred to as the procedure 'PASAPAS', is used. During each time step, the fracture parameter (J-integral in our

case) is computed and constantly compared to the crack initiation criteria. This threshold is chosen to be the critical energy release rate here. As long as the criterion is not met, the computations are pursued until reaching or slightly exceeding it. Then, the arguments of interest such as the displacement and the stress field are stored to be used for the subsequent analysis. We also recover the last loading value, which will be kept constant afterward.

3.2.2.2 Explicit calculations

To model our dynamic system, the time integration of the elastodynamic equation below is carried out using the Newmark method [NEW 59]:

$$M\ddot{\mathbf{U}} + K\mathbf{U} - \mathbf{f_{ext}} = 0 \tag{3.1}$$

where M is the mass matrix, K the stiffness matrix, $\ddot{\mathbf{U}}$ and $\mathbf{U}$ are the acceleration and the displacement vectors, respectively, and the system is subjected to external efforts denoted as $\mathbf{f}_{ext}$.

Newmark method

The main focus of this part relies on implementing the explicit Newmark algorithm within Cast3m. Therefore, a thorough insight into its approximations and structure is outlined below. This numerical approach approximates the temporal functions, displacement and velocity by means of Taylor expansion, to solve differential equations. Their developments lead to a third-order term assumed proportional to the acceleration, introducing the parameters γ and β. The displacement and its first-time derivative are solved as:

$$\begin{cases} U_{n+1} = U_n + \Delta t\dot{U}_n + \frac{\Delta t^2}{2}\ddot{U}_n + \frac{\Delta t^3}{3}\left(3\beta\frac{\ddot{U}_{n+1}-\ddot{U}_n}{\Delta t}\right) \\ \dot{U}_{n+1} = \dot{U}_n + \Delta t\ddot{U}_n + \frac{\Delta t^2}{2}\left(2\gamma\frac{\ddot{U}_{n+1}-\ddot{U}_n}{\Delta t}\right) \end{cases} \tag{3.2}$$

Eventually, the simplification of (3.2) leads to (3.3):

$$\begin{cases} U_{n+1} = U_n + \Delta t\dot{U}_n + \Delta t^2\left(\frac{1}{2}-\beta\right)\ddot{U}_n + \Delta t^2\beta\ddot{U}_{n+1} \\ \dot{U}_{n+1} = \dot{U}_n + \Delta t(1-\gamma)\ddot{U}_n + \gamma\Delta t\ddot{U}_{n+1} \end{cases} \tag{3.3}$$

In the Newmark family algorithms, two types can be distinguished (cf. TAB.3.2), either implicit or explicit. This characteristic is defined by the values of γ and β. Explicit solvers describe the solution at a subsequent time t_{n+1} using the current state only. Whereas implicit methods employ both the currently known state t_n and the future one t_{n+1} in the

approximation.

Integration method	γ	β	Type	Stability
Finite difference method	1/2	0	explicit	conditionally stable
Linear acceleration	1/2	1/6	implicit	conditionally stable
Average acceleration	1/2	1/4	implicit	unconditionally stable

Table 3.2: Properties of some Newmark computational schemes.

Taking into account our model requirements, a central finite difference method is chosen to describe the discretized fields $\dot{U}_{n+1}$ and U_{n+1} (3.4):

$$\begin{cases} U_{n+1} = U_n + \Delta t \dot{U}_n + \frac{\Delta t^2}{2} \ddot{U}_n \\ \dot{U}_{n+1} = \dot{U}_n + \frac{\Delta t}{2} \ddot{U}_n + \frac{\Delta t}{2} \ddot{U}_{n+1} \end{cases} \tag{3.4}$$

Stability of explicit finite difference method

At time t_n, the discretized structural equation of motion (3.1) becomes:

$$M\ddot{U}_n + KU_n - F_n = 0 \tag{3.5}$$

The use of a time integration scheme requires the study of its convergence, stability and consistency. In the following analysis, the stability of the central finite difference method is checked and a sufficient condition is developed to ensure accurate results.

For any given quantity V, the average and the difference between V at time n and $n+1$ are denoted as:

$$[V] = V_{n+1} - V_n \qquad \langle V \rangle = \frac{V_{n+1} + V_n}{2} \tag{3.6}$$

Using the above notations in (3.4), we obtain:

$$\begin{cases} [U] = \Delta t \langle \dot{U} \rangle - \frac{\Delta t^2}{4} [\ddot{U}] \\ [\dot{U}] = \Delta t \langle \ddot{U} \rangle \end{cases} \tag{3.7}$$

The stability of the method is not influenced by the existence of external efforts. Therefore, we rewrite our equation (3.5) at time t_n and t_{n+1} so that F_n and F_{n+1} are null. Their difference is expressed as:

$$\mathbb{M}[\ddot{U}] + \mathbb{K}[U] = 0 \tag{3.8}$$

Then, we multiply (3.8) by $[\dot{U}]^T$ and we replace $[U]$ by its expression in (3.7) [HUG 87]:

$$\langle \ddot{U} \rangle^T (\mathbb{M} - \frac{\Delta t^2}{4}\mathbb{K})[\ddot{U}] + [\dot{U}]^T \mathbb{K} \langle \dot{U} \rangle = 0 \tag{3.9}$$

This equation proves that the explicit method is stable only if $(\mathbb{M} - \frac{\Delta t^2}{4}\mathbb{K})$ is a positive definite matrix. Given its definition, the stability condition is then deduced when solving (3.11) and considering the eigenvalue analysis in vibration $det(\mathbb{K} - \omega^2 \mathbb{M}) = 0$, where X is the eigenvector associated with the eigenvalue ω^2:

$$\mathbb{K}X = \omega^2 \mathbb{M}X \tag{3.10}$$

$$\begin{aligned} X^T(\mathbb{M} - \frac{\Delta t^2}{4}\mathbb{K})X &= X^T\mathbb{M}X - \frac{\Delta t^2}{4}X^T\mathbb{K}X \\ &= (1 - \frac{\Delta t^2}{4}\omega^2)X^T\mathbb{M}X \end{aligned} \tag{3.11}$$

From this equation, it can be inferred that the stability condition depends on $1 - \frac{\Delta t^2}{4}\omega^2$ being positive. Hence, for a fixed mesh size, the choice of the time step Δt is defined as:

$$\Delta t \leq \Delta t_c = \frac{1}{\omega_{max}\sqrt{\frac{1}{4}}} \tag{3.12}$$

where ω_{max} is the greatest eigenvalue of the meshed structure, associated with the smallest element.

3.2.3 Mass lumping strategies

Defining the mass matrix remains one of the major impediments that hindered researchers from developing a fully explicit enriched model. As detailed in the previous section, the use of an explicit algorithm requires specifying the critical time step and constantly checking its relevance as the crack propagates. It has also been demonstrated that this time step is strongly contingent on the highest eigenvalue of the discretized structure. Along its extension, the crack tends to go through the element, reaching its edges or even altering its size. In such cases, the mesh size is no longer fixed. For distorted elements with very small segments, we obtain huge values of ω_{max}, thus a critical time step tending to zero, rendering the computations unfeasible.

Many works have been conducted to lump the mass matrix. Asareh et al. [ASA 20] have proposed a technique where null or negative masses are assigned to the enriched degrees of freedom. The main advantage of this method is its independence from the enrichment functions. However, the crack domain is only solved using an implicit algorithm. Menouillard lumping strategy [MEN 08], treats the broken elements explicitly but has only considered the discontinuous enrichment. His technique aims at preserving

the critical time step of a free-crack structure while conserving the kinetic energy for rigid body motions. It constructs a block diagonal matrix, where each enriched node is assigned its enriched degrees of freedom (dof) within the mass matrix. The appointed value is the same as the one computed for standard elements.

In Cast3m, the discontinuous enrichment introduces 3 dofs, namely A_x, A_y and A_z while the singular enrichment generates 24 dofs: B_{ij}, C_{ij}, D_{ij} and E_{ij}. The index $i \in \{1,2\}$ stands for the number of crack fronts (two fronts for internal cracks). The index j represents the dimension of our model where in 3D, $j \in \{x,y,z\}$. These degrees of freedom are associated with the singular function defined in (2.3). So far, no lumping technique has been developed to take into account these singular dofs explicitly. In this first approach, it is more straightforward to adapt our algorithm to discontinuous enrichment, hence the pertinence of Menouillard approach.

As the crack advances, new elements are continuously enriched. To account for these changes, we developed two Cast3M procedures that are executed simultaneously (cf. Appendix A). The first procedure, named *MASS3D*, modifies the mass matrix, by adding the dofs associated with the enriched elements. The second procedure *MESHXF* identifies the newly enriched elements and forward the information to the first one. At each time step, the elements crossed by the discontinuity are compared to those detected at the previous time step. If newly enriched elements are spotted, the first procedure proceeds to a modification of the mass matrix, otherwise, it remains the same.

3.2.4 Crack initiation criteria

In our configuration, where the crack path is already known, two features are to be determined to reproduce crack propagation: the initiation and propagation criteria. The major goal of our numerical model is to outline the reasons behind the crack terminal velocity. Hence, it is chosen to avoid any parameter or variable that may directly control the crack velocity. This implies that our algorithm defines an initiation criterion that is also expected to control crack extension.

Using the energy-based approach for crack initiation, we evaluate the strain energy release rate, or work per unit fracture surface area, denoted as the J-integral [RIC 68]. Our criterion stems from Griffith theory [GRI 21] stating that the crack will propagate if:

$$J \geq G_c \quad where \quad G_c = 2\gamma \tag{3.13}$$

where G_c is the critical energy release rate and γ the surface energy.

As aforementioned in Section 3.2.1.2, we disregard the orthotropic property of monocrystalline silicon. Therefore, the material features (isotropic, brittle and linear elastic) enable to employ an already implemented procedure G_{THETA} in Cast3M. This procedure requires the definition of several numerical parameters. The most prevalent

ones are the crack front location, the number of element layers around it and the displacement field, necessary to calculate the J-integral (cf. Appendix B).

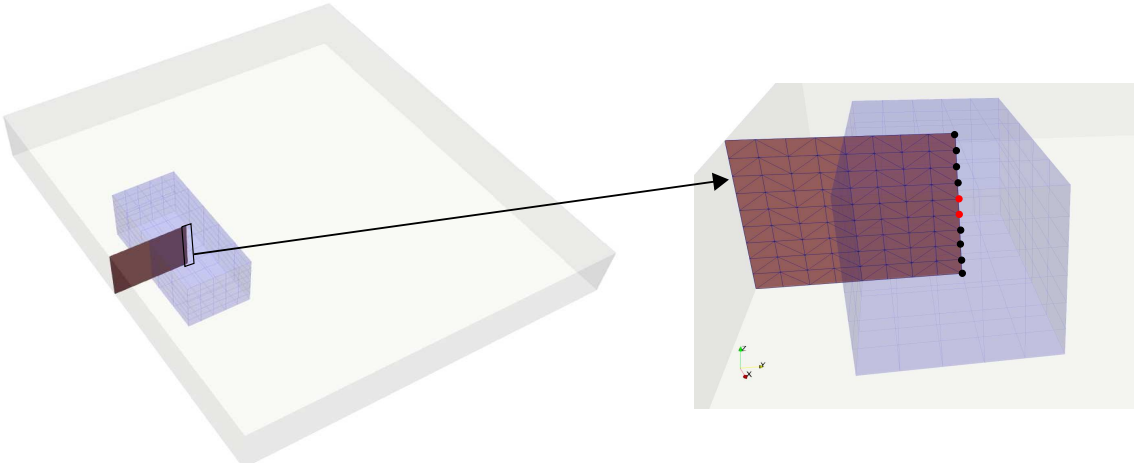

Figure 3.5: J-domain: element layers around the crack front.

According to the model, the crack front is discretized into several 2D linear triangular elements, namely TRI3. We specify a fixed number of element layers along which J-integral will be evaluated. For each front node, the procedure returns its proper J value. The blue elements layer associated with the red central nodes of the crack front is illustrated in FIG.3.5. However, for the other crack front nodes, there are fewer elements above or below than the layer thickness. Therefore, the J values computed herein are not valid.

In our case, we assume that the crack front is straight. If we were to consider the computed J values for each node, some will attain the criteria while others not, resulting in a blunt crack shape. To simplify and overcome this issue, only the J value computed at the central node is considered. It is then assigned to all the front nodes, thus ensuring an even propagation.

For each time step, in both static and dynamic analysis, the J-integral is computed and compared to the surface energy, which is a material property. If J is greater, our initiation criterion is met. The propagation rate is then governed by the excess of energy computed at this instant, which is converted to newly created crack surfaces $A_{created}$. Given the straight front and its rectilinear propagation, the crack increment l_{crack} is deduced from the geometric parameters of our model:

$$\begin{aligned} 2A_{created} &\iff \frac{J-G_c}{G_c} \\ l_{crack} &= \frac{A_{created}}{e} \end{aligned} \tag{3.14}$$

where e is our structure thickness and $A_{created}$ the crack surfaces area.

The first calculations revealed that small crack increments are created within the same element. This leads to substantial evanescent waves that impact the J-values and hinder the crack from going further than two elements. As a matter of fact, the use of discontinuous enrichment while omitting the singular one enables detection of the crack front only when it reaches an element edge. Therefore, it is not possible to follow its propagation inside an element. If the amount of energy transformed into crack surfaces is not high enough for the crack to go through a whole element, the crack grows by an extension da but can not be detected when evaluating the mechanical fields and the J-integral.

This issue prompts us to review and modify our propagation algorithm. As described in FIG.3.6, the propagation is constrained to an element-to-element propagation. The crack is set to propagate only if the amount of energy calculated is sufficient to break a whole number of elements. The front location is governed by a lower limit defined as the length of the element.

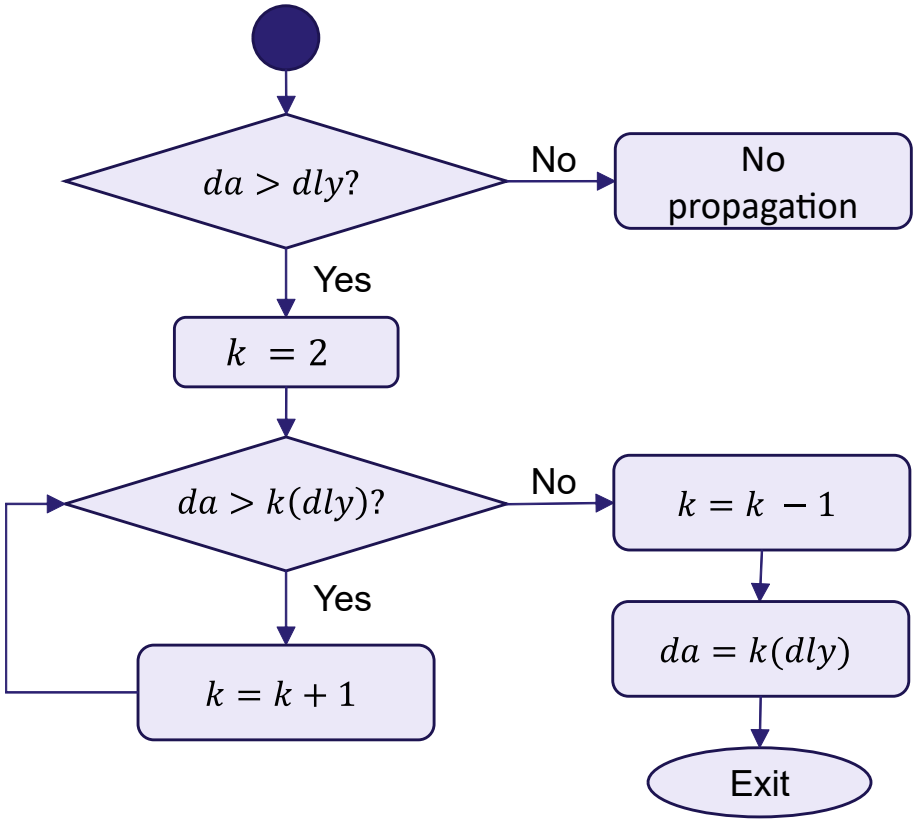

Figure 3.6: Crack propagation algorithm.

3.2.5 Cast3m algorithm

Quasi-static analysis - Procedure PASAPAS

— An increasing displacement is applied.

— The amount of energy required to break an element according to (3.14) is computed. This value is defined as G_{lim}.

— For each step of the procedure *PASAPAS*, the J-integral distribution along the crack front is evaluated.

— The J value of the central node is compared with G_{lim}:

- If $J \geq G_{lim}$: we exit the quasi-static analysis. For that given state, we extract and store the associated displacement and stress field. The value of the applied displacement is also saved to be used later.
- If $J < G_{lim}$: we keep on increasing the displacement until storing enough energy within the structure to trigger crack propagation.

Dynamic analysis - Central Finite Difference Scheme

— The time step Δt is computed.

— The fields of interest such as the displacements and stresses are initialized according to the quasi-static analysis.

— The loading is maintained constant throughout this analysis.

— The displacement d_{n+1} is computed:

$$d_{n+1} = d_n + \Delta t v_n + \frac{\Delta t^2}{2} a_n \tag{3.15}$$

— The J-integral is computed by the procedure G_{THETA} (where d_{n+1} is used as an input) and compared to G_{lim} or a multiple thereof.

— Activation of the propagation procedure: the fields are updated by adding the enriched degrees of freedom denoted as A_x, A_y and A_z in Cast3m. The level sets are updated so as to identify the position of the new crack front.

— The mass matrix is updated using the lumping strategy (See Section 3.2.3 for more details).

— The internal and external efforts denoted F_{n+1} are evaluated.

— The acceleration a_{n+1} is computed:

$$a_{n+1} = \mathbb{M}^{-1} F_{n+1} \tag{3.16}$$

— The velocity v_{n+1} is computed:

$$v_{n+1} = v_n + \frac{\Delta t}{2}(a_n + a_{n+1}) \tag{3.17}$$

3.3 Results and discussions

The results presented below resume all the foregoing model parameters and propagation criteria. A parametric study is carried out to evaluate the influence of several parameters on the J-integral and the crack velocity. The results are then discussed using the post-processing and visualization software Paraview [AHR 01] and Matlab [MAT 21].

The variable *u1phy* represents the displacement field of the structure. At each time step, the displacement fields *ucrck1u* and *ucrck1d* are computed for the upper and lower crack surfaces, respectively, using the operator *XFEM*. FIG.3.7 and FIG.3.8 illustrate the broken wafer with different amplification factors.

At the end of the dynamic analysis, we retrieve the crack length evolution with time. In the first simulation, two elements layers are used to compute the J-integral. As illustrated in FIG.3.7, the crack stops propagating nearly before reaching the end of the wafer. This occurs once the number of element layers ahead of the crack front becomes less than the number used by the G_{THETA} procedure. Besides, the J-integral values decrease considerably once the crack reaches the end of the plate, thus becoming lower than the crack initiation threshold.

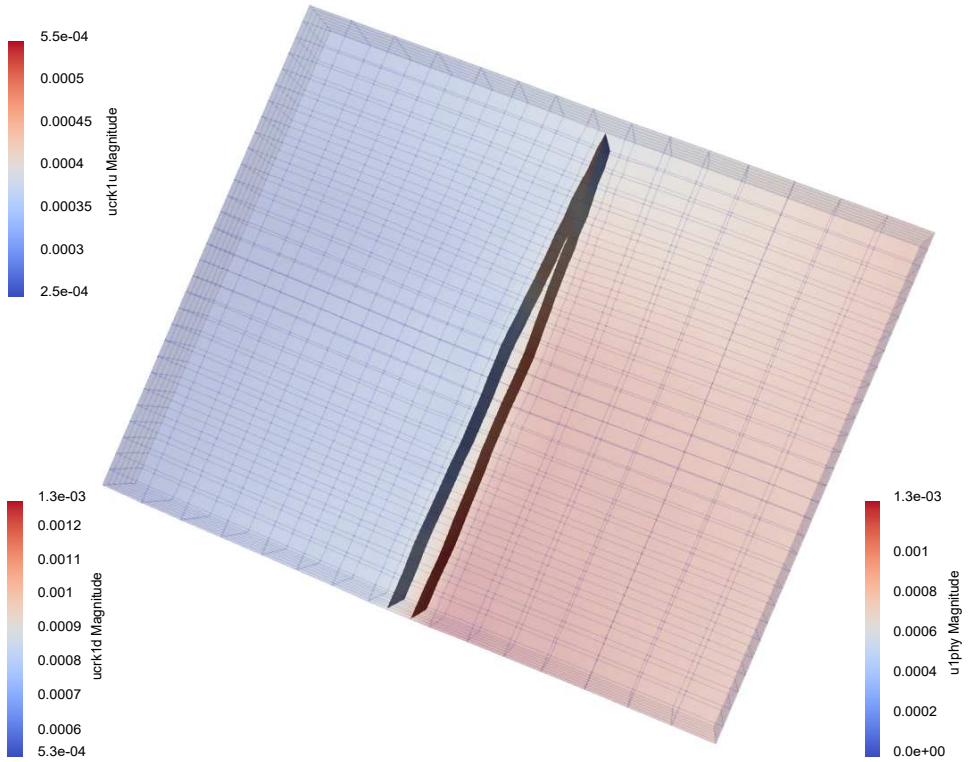

Figure 3.7: Numerical simulation of crack propagation - Amplification 200.

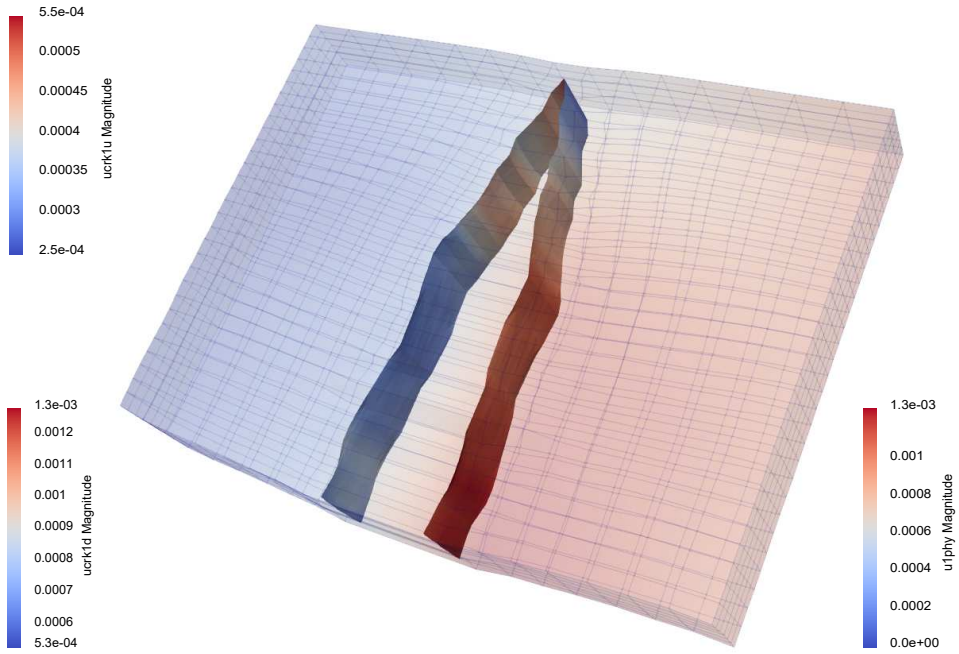

Figure 3.8: Numerical simulation of crack propagation - Amplification 1000.

3.3.1 *J*-integral along crack propagation

The first crack extension occurs at the first step of the explicit analysis. This explains the sudden drop in the J values observed in FIG.3.9. Throughout the computations, the J-integral is constantly checked until enough energy is stored to initiate another crack growth. The vertical red dashed line indicates the instants of crack propagation. It is observed that once propagation occurs, the J-integral values do not decrease immediately. As a matter of fact, if the crack extension is triggered at instant t_n, the actualization of the displacement field is performed at the same time step and concerns the newly enriched elements. This update is carried out by adding the degrees of freedom A_x, A_y and A_z and assigning them the null value. At this point, the crack had grown virtually but no structural physical quantity had been notified by its new position. It will then take two time steps, hence at t_{n+2}, so that the enrichment dofs of the displacement are filled with non-zero values representing the opening of the crack surfaces. Following these changes, the J value drops suddenly and throughout the calculations, it increases again up to the critical value. This pattern is repeated several times until reaching the other extremity of the plate.

Towards the edge of the plate, the J values do not exhibit the same pattern as before. More oscillations and an abrupt decrease in their values are observed. At this stage, if calculations are pursued, J can even attain negative values. The related crack surfaces are then subjected to extreme deformation. In Paraview, we can clearly visualize the amplification of the evanescent waves and their interaction with the crack, once reflected

from the free surfaces. Since many waves have accumulated during the propagation and possible edge effect, the computation of the J-integral and the crack velocity will not be considered valid near the end of the plate.

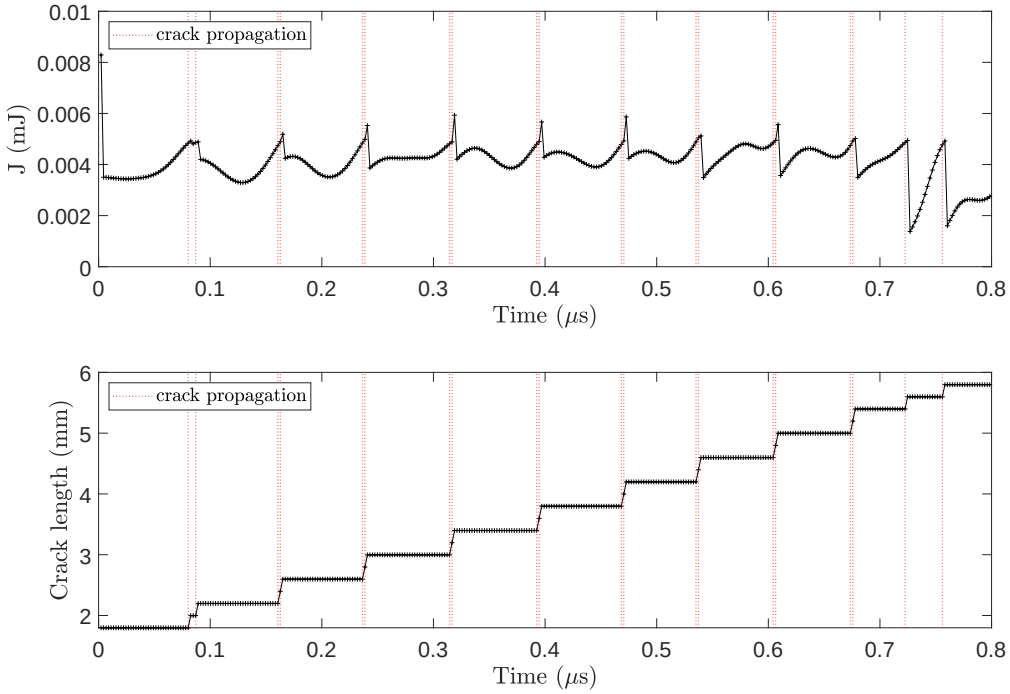

Figure 3.9: Evolution of J-integral and crack length.

3.3.2 Crack velocity

The aim of our study is to numerically estimate the crack speed in monocrystalline silicon and to identify the reasons behind its limiting velocity. With no propagation criteria, this value is assumed to be recovered as a direct result of the simulation. It also goes without saying that these results are quantitative since our numerical model and the applied loading are different from those used in experiments.

As illustrated in FIG.3.8, the velocity of the crack front oscillates. Therefore, the velocity evolution is smoothed (red line).

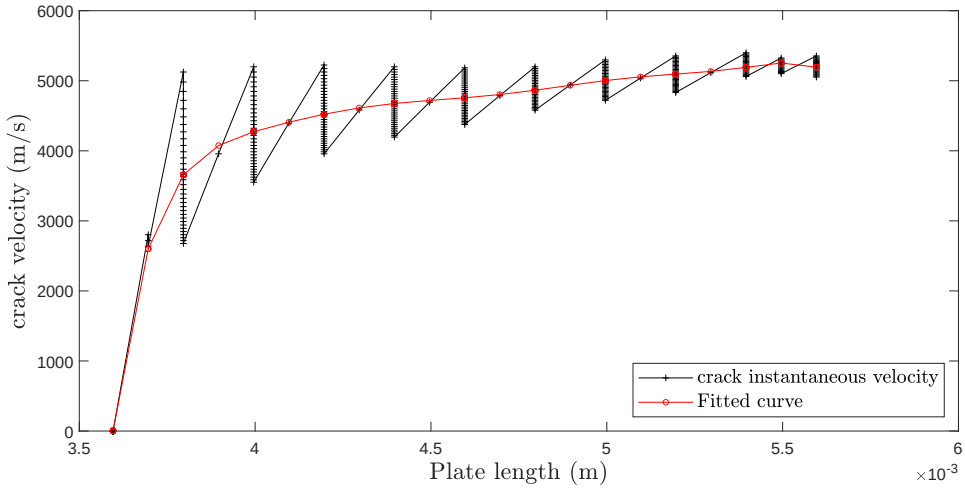

Figure 3.10: Evolution of the crack velocity.

The computed terminal velocity is slightly above the Rayleigh wave speed ≈ 4700 m/s. Furthermore, the instantaneous crack velocity and its profile are consistent with those recovered experimentally [WAN 19b]. Rapid acceleration is followed by a stationary phase where the attained velocity is the Rayleigh wave speed C_r. In FIG.3.10, the amplitude of the velocity oscillations is more important at the onset of the propagation. It is mainly due to the sudden change of the analysis type: from static to dynamic. Unlike the measured speed values, no limiting speed has been reported in these simulations. For this model, it can be inferred that with no condition on the crack speed, this latter is meant to reach its maximum value C_r.

3.3.3 Influence of the modeling parameters

Each numerical model implies the use of many parameters. Also, many assumptions and conditions are established for calibration purposes. Herein, two of the most important parameters are discussed. First, the computation of the J-integral depends upon the number of element layers around the front. Since these J values govern the crack propagation, it is only evident that the crack speed is in turn, influenced. Second, it has been shown in the work of [WAN 19b], that the crack speed is closely affected by the notch length. The crack exhibits higher velocities for smaller notches.

3.3.3.1 Number of element layers

In order to highlight the influence of the number of element layers on crack propagation, some values of this parameter are analyzed: 2, 3 and 4.

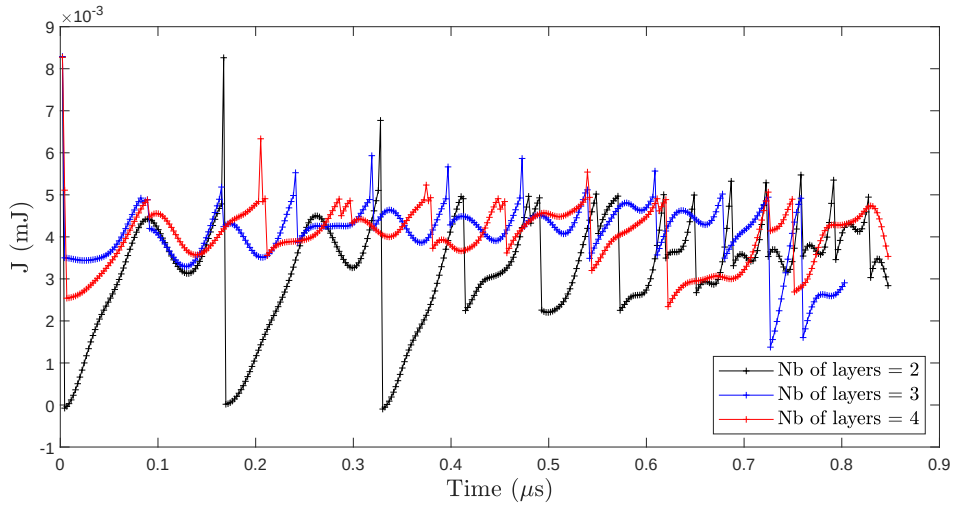

Figure 3.11: Evolution of J-integral for different number of element layers.

In FIG.3.11, the use of more than two element layers reduces the discrepancies of the J values following each propagation. Although the J field is more uniform in this case, the crack arrest is reported way before the structure complete failure. Nevertheless, FIG.3.12 demonstrates that the effect of the number of layers on the J values does not lead to a significant change in crack velocity. For the rest of the parametric analysis, we chose to keep two element layers.

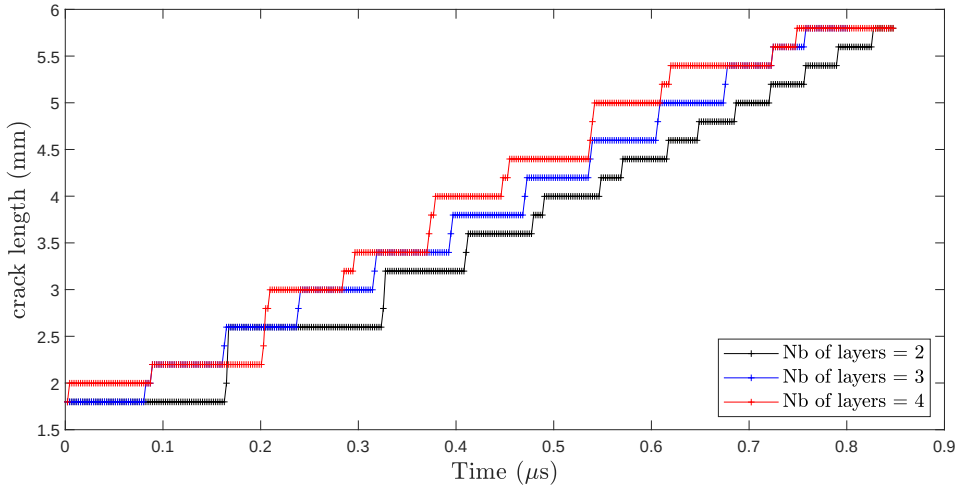

Figure 3.12: Crack propagation for a different number of element layers.

3.3.3.2 Notch length

For each notch length, a different static analysis is conducted beforehand to identify the loading for which the crack initiation criterion is met. We define three cases: l_{notch} = 1.2, 1.8 and 2.6 mm. The table below summarizes the average velocity for each case.

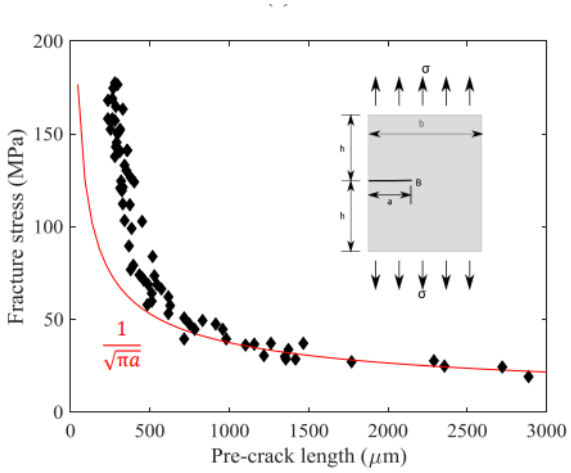

(a)

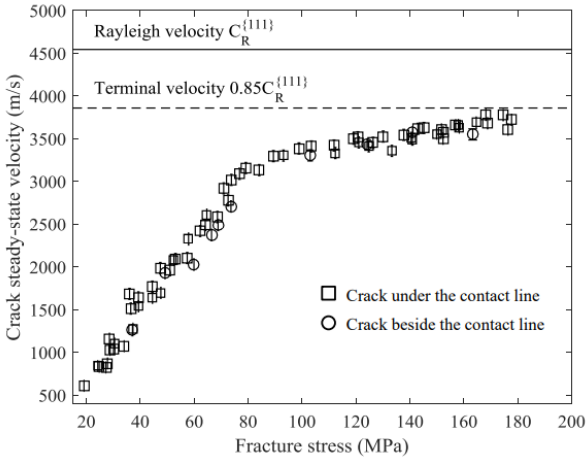

(b)

Figure 3.13: (a) Fracture stress σ_f as a function of notch length a (b) Fracture stress versus crack steady-state velocity [WAN 19b]

In the work of Wang et al. [WAN 19b], it has been demonstrated that the fracture stress decreases for an increasing notch length (cf. FIG.3.13(a)). Additionally, when velocities were measured, FIG.3.13(b) showed that for high fracture stresses, the maximal attainable velocity was 85% of C_r.

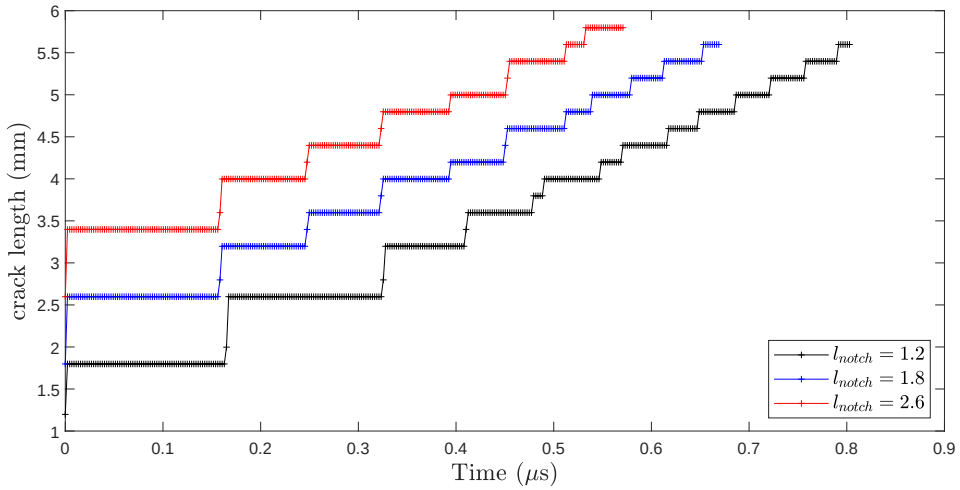

Figure 3.14: Crack propagation for different notch lengths.

In our work, the crack average velocity is deduced from FIG.3.14. As expected, TAB.3.3 shows that our model is broadly in line with the trend of speed measurements conducted on monocrystalline silicon (cf. FIG.3.13). The shortest the notch, the higher its velocity. Nevertheless, no limiting velocity has been reported. In fact, these values cannot be compared directly to the measured ones, since our reference model is different from the experimental configuration.

Notch length (mm)	Crack average speed (m/s)
1.2	4746
1.8	4499
2.6	4220

Table 3.3: Crack average velocity for different notch lengths.

3.4 Conclusion

It was shown in this chapter that the implementation of an explicit XFEM in Cast3m has proven capable of simulating crack propagation on monocrystalline silicon. Despite the limited crack description and the imposed conditions, the obtained results are in accordance with the theoretical work conducted by Freund [FRE 90]. As a matter of fact, the maximum speed acquired by the crack is the Rayleigh wave velocity. Also, the crack instantaneous speed exhibits the same pattern as portrayed in the work of Wang et al. [WAN 19b]: a rapid acceleration phase followed by a steady-state velocity. For a simplified 3D model, we outlined the solutions and limitations we had come across while constructing our algorithm. Although it provides an insight into the dynamics

of a rapidly moving crack, it remains inconclusive regarding the processes behind the limiting velocity observed in experiments. Clearly, numerical errors prior to some inputs, for instance, the J-domain, can play a significant role in preventing a more realistic representation of the propagation.

All the above analysis remains purely qualitative and has not been the subject of a quantitative study yet. First of all, the model dimensions do not reflect the geometry of our wafers and secondly, the loading type is different (tension vs. bending). A major impediment in reproducing the experiments relies on the approach adopted by Cast3m to evaluate the initiation criterion. Under a bending test, the elliptical front shape can be particularly problematic to track, when evolving along the plate thickness. The front nodes beside the tensile surface are meant to fulfill the crack initiation criteria before those located at the compressed surface. Unfortunately, the J calculations around these nodes are inaccurate and the elliptical front shape can not be recovered. Another issue raised was the formulation of the J-integral. So far, we evaluated the static strain energy release rate. However, since the propagation is characterized as dynamic, the kinetic energy is significant and could be taken into account when assessing crack extension based on a dynamic J-integral.

To conclude, the use of the eXtended Finite Element Method in explicit dynamics has shown encouraging results. The numerical validation of the implemented Cast3m algorithm is considered as an important early step in achieving a fully realistic and viable model. More importantly, the identification of our model shortcomings provides a clear basis for further development in this field.

Chapter 4

Experimental study of dynamic crack propagation

Contents

4.1 Crack velocity measurement methods

Many techniques have been developed to monitor crack growth and assess its velocity [SCH 59]. Among common methods, we find the high-speed camera and the potential drop technique. These measurement methods have proven capable of capturing the high-velocity cracks observed in brittle materials, thus shedding some light on the physical phenomena governing the fracture processes. In this section, we will first recall the principle of each method and its recent developments. In the second stage, all the crack velocity measurements conducted on crystalline silicon will be reviewed and discussed.

4.1.1 High-speed camera

A high-speed camera is a well-known apparatus used in many fields to track and record rapid physical phenomena. For several decades, this imaging technique has utterly evolved in terms of spatial and temporal resolution and has been extended to a wider range of materials. Initially, only transparent materials were considered. Nowadays, even non-transparent materials can be examined using the light reflected from a plane surface. In fracture, it has been extensively used to measure crack growth rate while observing its path and the associated fracture processes. For brittle materials, where crack speeds are nearing the Rayleigh wave velocity, this technique was revealed to be quite efficient and accurate [WAN 19b, KIM 12, **?**].

Basically, during a phenomenon that we want to observe, the camera takes a series of images and stores them as sequential frames. If any variation can be detected along the occurrence of the phenomenon, it can be used to trigger the camera. Some examples of detectable signs are the sound, a luminosity variation, or a force drop.

In photography, one other major setting to achieve accuracy and good quality frames is the shutter speed also known as the exposure time. During the frame time interval, a fraction of a second is dedicated to exposing camera sensors to a certain amount of light. Defining the shutter speed is crucial to obtain a good exposure of the frame and also to reduce errors when measuring short-time varying quantities. This controls the motion blur while achieving the righteous lighting for the grabbed frame. As regards fast phenomenon, lightning can be very challenging when increasing the camera frequency.

4.1.2 Potential drop technique

The potential drop technique was first introduced by [BAR 57] to measure crack growth kinetics of specimens containing high hydrogen concentration. Nowadays, it is a widely used method to measure crack extension. As its name implies, the measured electrical potential of a given sample will vary once this latter undergoes a change of state. This allows us to explore and quantify the variations in the material structure, thus the crack position within the specimen. Originally, only conductive materials were entitled to this

method. Subsequently, adjustments were made to study insulators by depositing very thin conductive layers over their surface. Their fracture properties should be similar to those of the investigated material.

The potential methods can be classified into two main categories: the direct current potential drop method (DCPDM) and the alternating current potential drop method (ACPDM). The first technique enables to monitor crack length whereas the second technique is characterized by its skin effect and it is mainly used to detect small cracks beside the surface and evaluate their depth [RAJ 10, LI 16].

4.2 Material and experimental set-up

Widely used in solar panels, mono and multi-crystalline silicon are the two most common materials used for the production of wafers. Aside from their crystalline structure, they both serve the same purpose of converting renewable solar energy into electricity. Given the astounding properties of cleavage dynamic fracture exhibited by crystalline silicon, all the ensuing experiments will be performed on this material. In the course of this work, monocrystalline silicon will be studied. The crack paths and velocities will be disclosed and measured using the aforementioned methods.

4.2.1 Monocrystalline silicon

As its name may suggest, monocrystalline silicon is composed of one homogeneous and continuous single crystal and is characterized by its diamond structure (cf. FIG.4.1). This atomic arrangement is inherent in semiconductors such as silicon or germanium. It can be compared to two intersecting face-centered cubic lattices where atoms form covalent bonds.

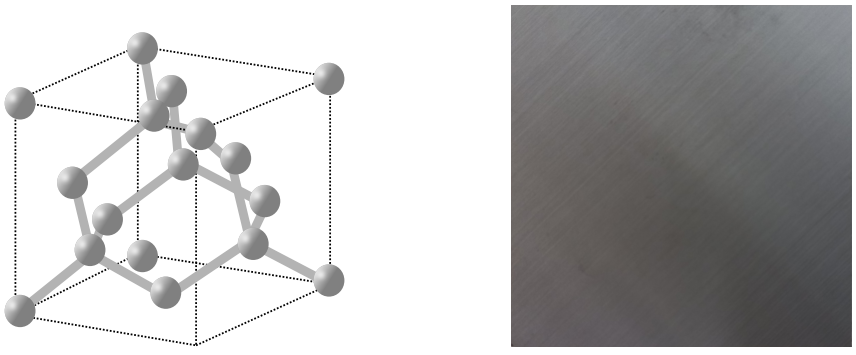

(a) (b)

Figure 4.1: (a) Crystalline structure of silicon and (b) monocrystalline silicon wafer.

Within a silicon crystal lattice, the mechanical, thermal and electrical properties will

differ from one crystal plane to another. These planes (cf. FIG.4.2) and their crystallographic directions are defined using Miller indices (hkl) and [hkl], respectively.

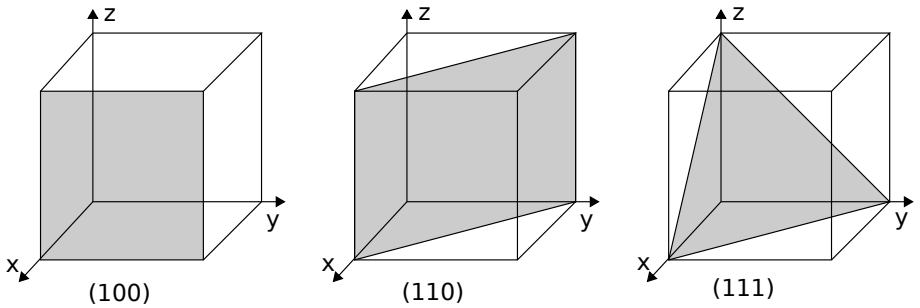

Figure 4.2: Crystal planes in silicon cubic lattice.

In cleavage fracture, cracks propagate along certain atomic planes, also referred to as preferential cleavage planes. For silicon, it mainly takes place along the (110) and (111) planes, which display low surface energies, as revealed in the work of [ZHA 18, LI 05, PÉR 00] (cf. TAB.4.1).

Crystal plane	Surface energy (J/m^2)
(100)	1.99
(110)	1.41
(111)	1.15

Table 4.1: Surface energies of various silicon crystal planes [HES 93].

The monocrystalline wafers are obtained using the Czochralski growth process [CZO 18]. It consists in immersing one single crystal named seed into a molten bath of silicon. The existing atoms will then get affixed to the seed as it is being pulled up from the liquid bath (cf. FIG.4.3(a)). The single crystal ingot is then cut and sliced up into wafers using the diamond wire technique. Various chemical and texturization treatments are then applied to the wafers before the final electrical circuits are printed (cf. FIG.4.3(b)).

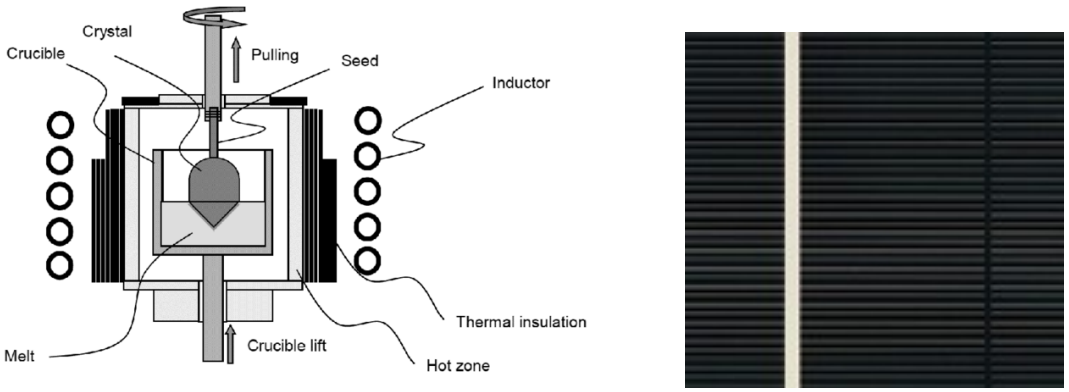

(a) (b)

Figure 4.3: (a) Czochralski Crystal Growth Process [AKS 12] and (b) monocrystalline silicon solar cell.

4.2.2 Multicrystalline silicon

The multicrystalline form of silicon is achieved by melting together multiple pure silicon fragments. Under a well-controlled temperature mold, the mixture is cooled to obtain a solidified ingot that is, at a later stage, cut to obtain wafers. As shown in FIG.4.4, these wafers display numerous small crystals, each characterized by its own grain size and orientation.

When compared to monocrystalline, multicrystalline wafers have a lower manufacturing cost since they undergo rapid solidification. However, they are less efficient when used in photovoltaic panels. The presence of grain boundaries prevents electrons from moving freely throughout the solar cells, thus impacting their performance and quality.

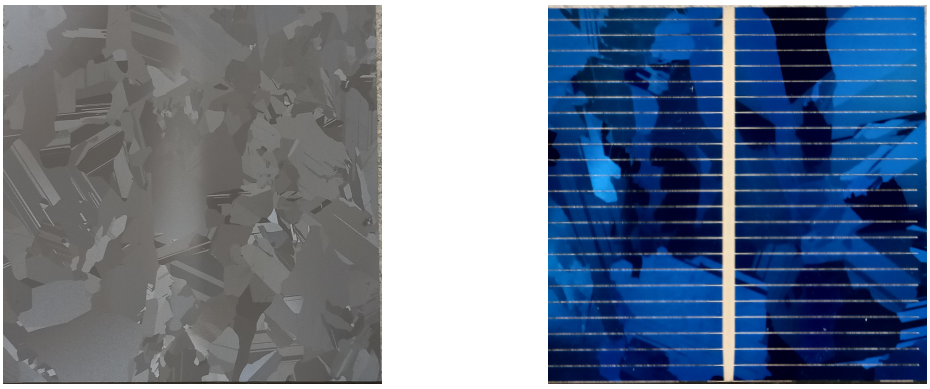

(a) (b)

Figure 4.4: (a) Multicrystalline silicon wafer and (b) multicrystalline silicon solar cell.

4.2.3 Mechanical set-up: four-line bending test

The specimens used in our tests are small samples of dimensions 50*mm* x 50*mm* x 190μm, obtained by cleaving the wire-sawn (001) silicon wafers (cf. FIG.4.5). They are oriented so that the surface is perpendicular to the [001] direction. To control the position of the crack initiation (and propagation), a centered notch is created manually using a sharp instrument. Therefore, the notch length, measured by optical microscopy on post-mortem samples, can not be controlled and varies from one sample to another. This prevents us from doing perfectly replicated tests. Nevertheless, it enables to investigate many crack velocities (cf. FIG.3.13(b)).

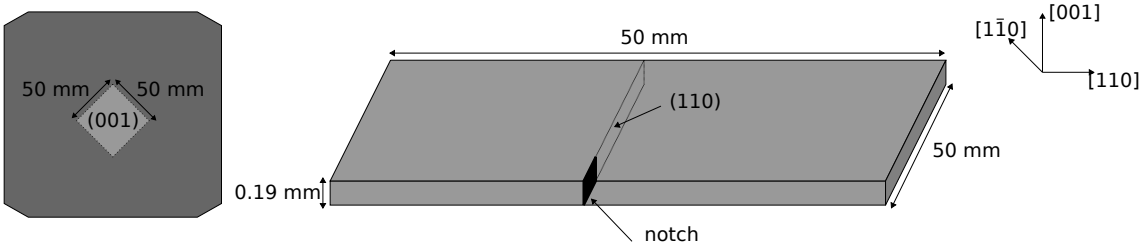

Figure 4.5: Geometry of monocrystalline silicon samples.

The silicon samples are subjected to a four-line bending test (cf. FIG.3.1(a)) using the MTS Criterion Series 40 tensile machine. The geometry of the experimental set-up, depicted in FIG.4.6, has been manufactured to match the specimen [ZHA 16].

Figure 4.6: Four line bending mechanical test.

The operational mode within the TW Elite software consists in defining the test type and the procedure variables. Once launched, it dictates the commands to the machine which executes the experiment. For further details, please refer to the well-described manuscript of the apparatus [MTS 14]. To ensure a quasi-static loading, a small displacement rate ($\approx$ 0.02mm/s) is applied. The force is measured continuously during testing, and the peak force (just before failure) is used to compute the failure stress for each broken sample using the four-line bending formula :

$$\sigma_f = \frac{3F(L-a)}{bh^2} \tag{4.1}$$

where F is the loading force at failure, b the sample width, L the distance between the two lower rollers and a the distance between the two upper rollers(cf. FIG.3.1(a)).

Since the load applied to the sample is rather low, a force sensor with a low force range is added along the mobile extremity of the machine to obtain a more accurate measure than the one acquired using the machine force sensor.

4.3 Potential drop technique

In our laboratory, many tests were previously conducted to operate the potential drop method on silicon wafers, which are semiconductors. In this section, an overview of the sample preparation and the electrical configurations is presented. Ultimately, the obtained results are compared to the existing data and further developments are considered.

4.3.1 Deposition method and sample preparation

Ultrasonic cleaning

To ensure a flawless deposition of chrome and gold layers onto the silicon samples, we start by cleaning our specimens. A batch of 25 samples is arranged in an open container. The first step consists in immersing them in an isopropyl alcohol solution. Once soaked for several minutes, they are placed in the ultrasound cleaning machine for 5 minutes. This equipment uses high-intensity sound waves to agitate the submerging liquid, hence removing the intricate contaminants and impurities of the sample surface.

EVA300 machine

This thermal vacuum evaporation machine was developed both for batch production and for research and development (cf. FIG.4.7). It is also renowned for its robustness, adaptability and efficiency when depositing thin films on the substrates. The thermal evaporation technology comprises a vacuum chamber. Therein, a metal or nonmetal pure material is heated until reaching the evaporation state. Then, this vapor stream is deposited onto the substrate to form a coating whose thickness is falling within a range of several angstroms to a few microns.

In our configuration, we chose chrome for the conductive layer and gold for the electrodes. After cleaning, the samples are carefully fixed to the machine rotating disk. Onto them, a stencil delineating the surface area of the conductive layer or the electrodes is placed. We then attach the assembly to the upper part of the apparatus and the deposition procedure is initiated.

Figure 4.7: EVA300 vacuum evaporation machine.

Deposition of chrome and gold layers

Two distinct depositions are performed. The first conductive layer is a deposit of a 60*nm* of chrome, illustrated in light grey in FIG.4.8(a). Therefore, the samples are retrieved and the stencil is changed to proceed with the second deposition of the sensing electrodes made of gold. However, when performing a straightforward deposition of gold onto the previous chrome layer, adhesion was not good enough. In fact, the uppermost surface of the chrome layer oxidizes once the samples are taken out of the machine. To avoid this issue, during the second deposition with electrode stencil, we carry out a deposition of 10*nm* of chrome first, before starting the deposition of 150*nm* of gold.

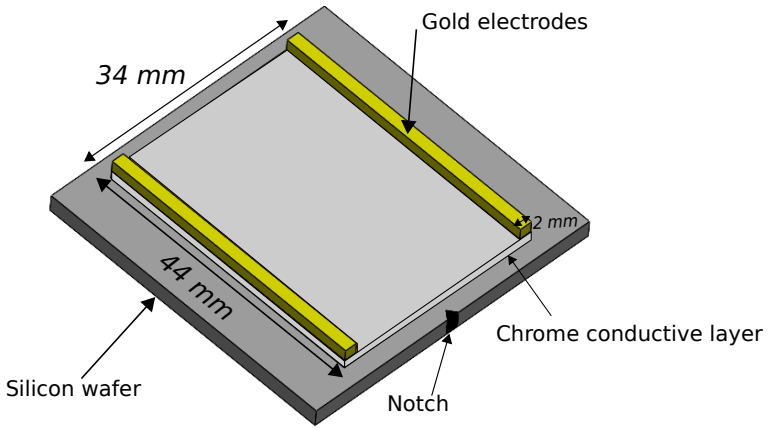

(a)

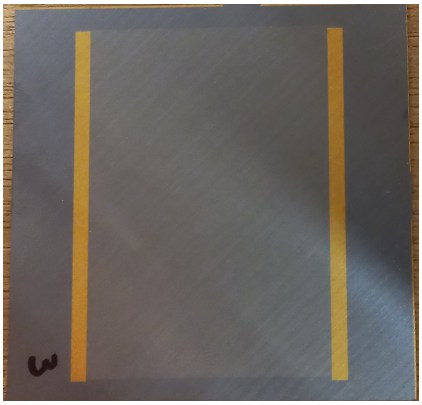

(b)

Figure 4.8: Silicon sample with conductive layers: (a) illustration with layers dimensions and (b) sample picture.

4.3.2 Electrical setup

4.3.2.1 Wheastone bridge

Our first configuration is a traditional Wheatstone bridge where the resistance R_4 is replaced by our pre-notched silicon sample. The resistances of the Wheatstone bridge R_1, R_2 and R_3 are chosen equal to 100Ω, and the sample resistance will vary from approximately 30Ω (before failure) to thousands of ohms (when totally failed). According to this variation, the electric potential V_{out} will change when the crack propagates through the wafer. This potential drop is measured using a Tektronix oscilloscope of bandwidth 50Hz. For each analog channel (cf. FIG.4.9), the oscilloscope will add an impedance to the circuit. Ideally, an infinite impedance would minimize the effect of the measurement device and would not alter the studied system. However, a relatively small impedance is chosen for our scope internal resistances (50Ω mode) because it is connected to an

equivalent small output impedance.

The circuit is powered by an external battery. To detect any changes in its voltage and how it may impact our measurements, two other oscilloscope channels ($CH2$ and $CH3$) are used. They will be measuring the tension going through the battery positive and negative ends. A math operation of these two measures will be performed to check the voltage stability throughout the experiment.

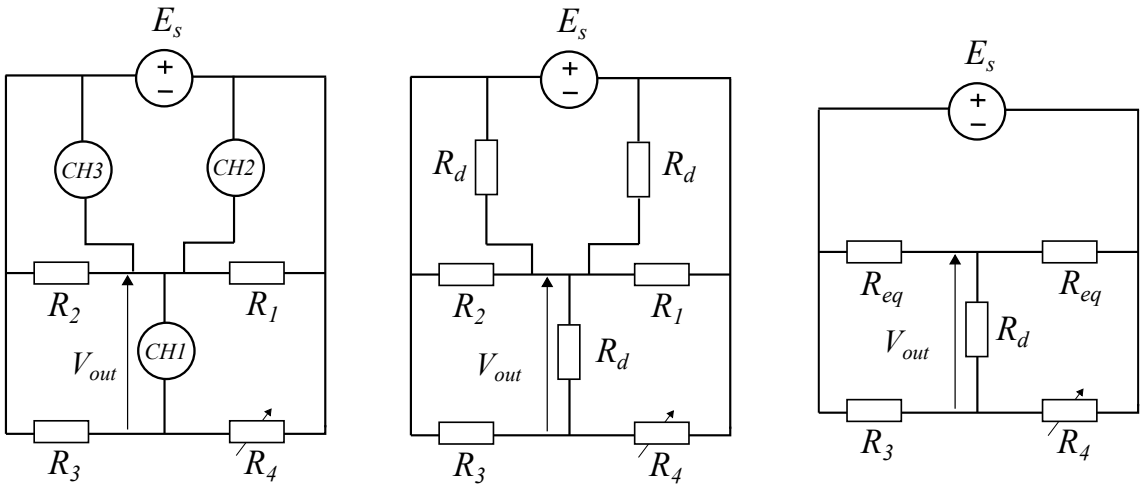

Figure 4.9: Wheatstone bridge circuits.

To link the silicon sample to the electrical circuit portrayed in FIG.4.10, two probes are welded onto the golden layers. This allows a proper flow of the current through the sample since it is a more conductive material compared to silicon and chrome.

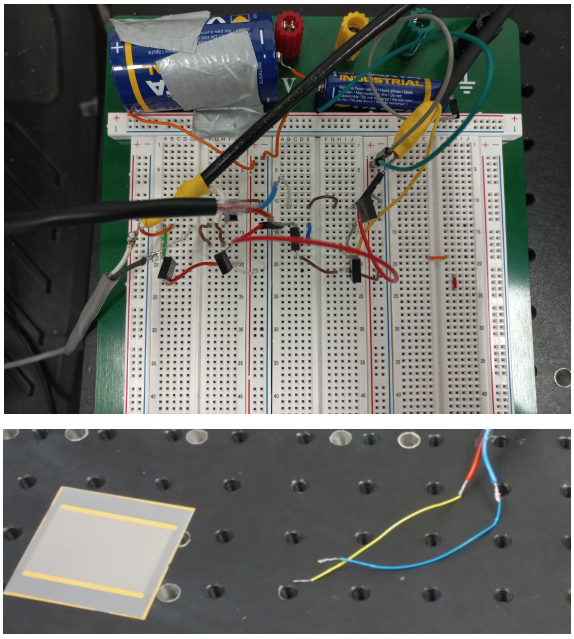

Figure 4.10: The Wheatstone bridge circuit (up) and close up on silicon sample welded.

Since we included the oscilloscope internal resistance R_d, the Wheatstone bridge formula is computed as follows:

$$V_{out} = E_s R_d \left[\frac{R_4 R_{eq} - R_{eq} R_3}{R_d(R_{eq}+R_{eq})(R_3+R_4) + R_{eq}R_3(R_{eq}+R_4) + R_{eq}R_4(R_{eq}+R_3)} \right] \tag{4.2}$$

where $R_{eq} = \frac{RR_d}{R+R_d}$ and $R = R_1 = R_2$. The resistance of the silicon sample is deduced from the previous equation:

$$R_4 = \frac{R_3[E_s R_d R_{eq} - V_{out} R_{eq} R_{eq} - V_{out} R_d (R_{eq}+R_{eq})]}{V_{out} R_d (R_{eq}+R_{eq}) + V_{out} R_{eq}(R_{eq}+R_3) + V_{out} R_{eq} R_3 + E_s R_d R_{eq}} \tag{4.3}$$

$$x_{crack} = L_{wafer} - \frac{L_{wafer} R_{40}}{R_4} \tag{4.4}$$

When loading the specimen, the crack will propagate straight ahead (without branching) along the weakest plane, and the notch ensures that it is located approximately in the middle of the specimen. During bending tests, the lower surface is subjected to tension, while the upper side undergoes compression. It has been shown in the work of [SHE 04], that under such loading conditions, the elliptical crack front will display a certain delay when propagating through the sample free surfaces. As logical as it sounds, tensile forces tend to tear up the concerned regions before incurring failure in the compressed areas.

In FIG.4.11, the specimen is placed so that its conductive layers are subjected to tensile loading. We, therefore, follow the crack evolution of the tensile side of the sample.

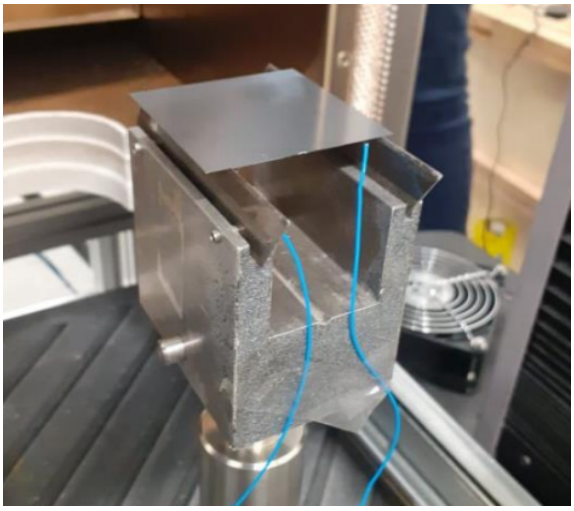

Figure 4.11: Silicon sample positioned on the 4-line bending apparatus before testing.

Once the crack reaches the conductive layer, a sudden change of the potential is perceived on the screen of the oscilloscope. Clearly, a temporal and quantitative trigger are previously defined. We set a threshold of a few voltages above the lower limit for the quantitative trigger. As for the temporal one, it is positioned in the middle of the monitor screen range. Therefore, it outlines the two portions of the signal before and after crack propagation on the conductive layer. It is noteworthy to mention that the conductive layer is not printed at the edge of the sample. Therefore, it will not capture the real onset of the crack but rather its entrance within the conductive layer.

4.3.2.2 Linearized Wheatstone bridge

With the presented configuration, it is observed that the wafer resistance changes promptly from a few ohms to thousands of ohms. While approaching the broken state, the achieved terminal resistivities are by far greater than those of the Wheatstone bridge components. Consequently, the electrical circuit is unbalanced and it is directly reflected in the output voltage. To 'balance' the circuit and obtain accurate measures of the tension across the wafer, operational amplifiers are used and the circuit is then qualified as 'linearized'. The new circuit arrangement is described in FIG.4.12, where $R_1 = R_2 = R_3 = 120\Omega$ and $R_5 = 1000\Omega$. The silicon sample R_4 and R_5 are connected in parallel. The equivalent resistance of this parallel circuit is denoted as R_c.

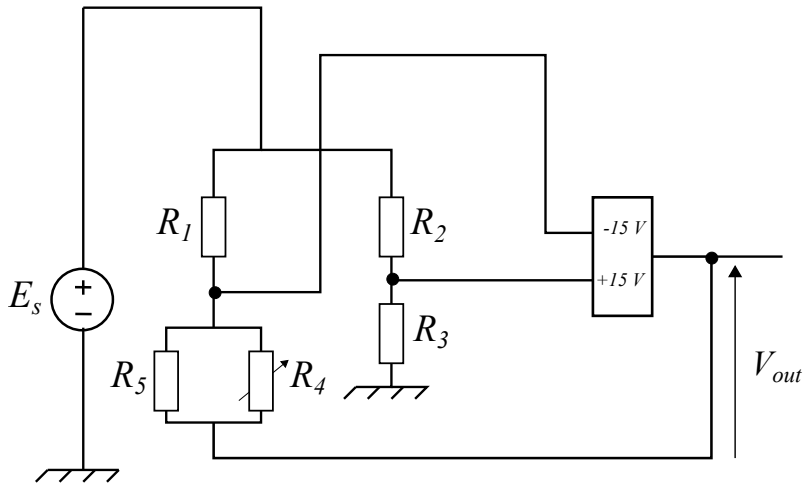

Figure 4.12: Linearized Wheatstone bridge circuit.

The expression for the equivalent resistance R_c as a function of the other parameters is:

$$R_c = R_1(1 - \frac{2V_{out}}{E_s}) \tag{4.5}$$

The sample resistance R_4 is then computed using the following equation :

$$R_4 = \frac{R_c R_5}{R_5 - R_c} \tag{4.6}$$

4.3.3 Results and discussions

Wheatstone bridge

The main purpose behind using the potential drop technique is its high resolution. The measured signal covers a large period of time: before, during and after crack propagation (cf. FIG.4.13(a) for test n°1) with up to 500 000 measurement points. However, what matters to us is the transient phase corresponding to crack growth. For instance, with an average crack velocity of 150 m/s, 3176 measurement points cover the propagation process, while the high-speed camera only returned 13 measurement points.

The initiation of crack propagation is chosen based on the average initial resistance computed by the oscilloscope before crack propagation. The two dotted red lines on FIG.4.16 represent the minimum and maximum voltage values corresponding to the sample before and after complete failure, respectively. Crack propagation is assumed to start at the last recorded value equal to the initial wafer resistance (cf. FIG.4.13(b)). All the ensuing results stem from the cropped voltage signal, whose measuring range has been selected manually. This is why comparing these results with other experimental methods will allow more detailed conclusions to be drawn regarding crack speeds.

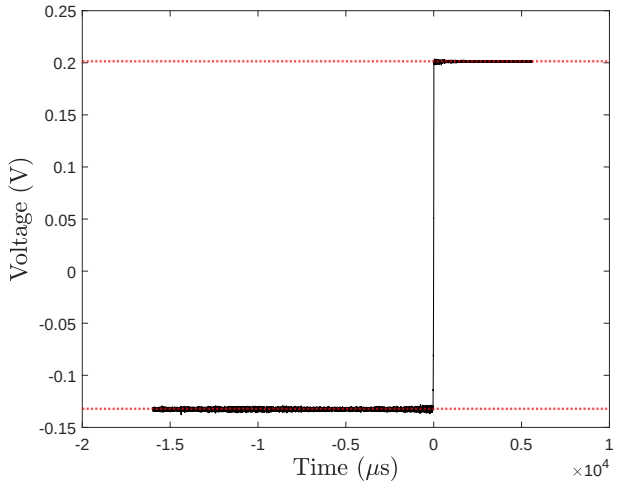

(a)

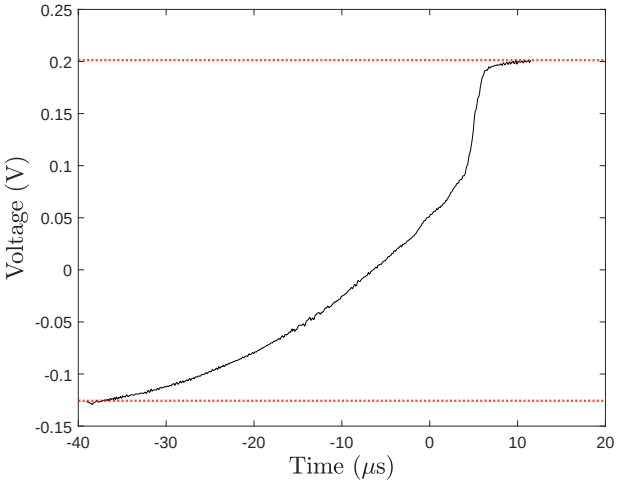

(b)

Figure 4.13: (a) Oscilloscope measurement of the wafer voltage and (b) zoom on the measured signal during crack propagation for test n°1.

FIG.4.14 shows the variation of the sample resistance using the output voltage and equation (4.3). From the computed resistance, the crack length x_{fiss} within the conductive layer can be computed using the following equation:

$$x_{fiss} = \frac{(R_4 - R_0)L}{R_4} \tag{4.7}$$

where R_0 is the initial value of the sample resistance R_4. In the test n°1, the value R_0 is 47Ω. The eq.(4.7) is obtained assuming the electrical field is homogeneous inside the uncracked conductive layer. Since this layer is very thin compared to the silicon sample and that border effects may arise, we have checked whether this assumption was valid

using finite element simulations. In Cast3m, we developed an electrical model to evaluate the wafer resistance for different crack positions. To some extent, the numerical results fit the analytical approximation of the crack position with respect to the wafer resistance. At the beginning of crack growth, the two curves overlay perfectly. When the crack reaches the end of the sample, some discrepancy is observed and is due to edge effects in the electrical field.

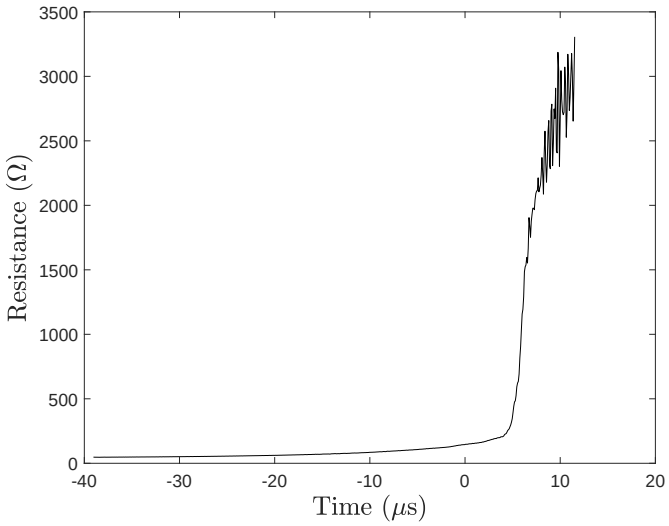

Figure 4.14: Silicon sample resistance computed using eq. (4.3).

In FIG.4.15(a), we use the above results and equations to plot the crack length. As observed on the electrical signal, the crack length signal exhibits some oscillations. Since we need to derive this latter to obtain the crack velocity, we need to smooth the crack position curve prior to derivation. The crack instantaneous velocity is presented in FIG.4.15(b) and is provided as a function of crack length.

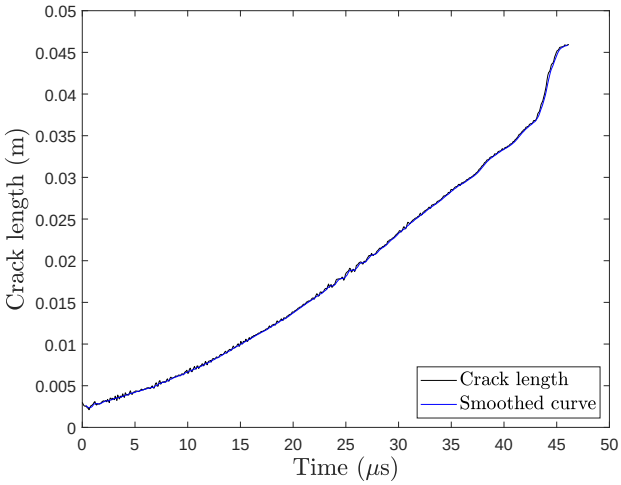

(a)

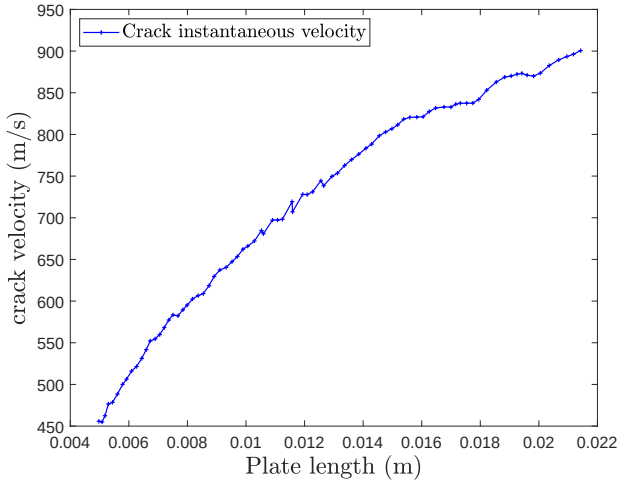

(b)

Figure 4.15: (a) Crack length computed using eq. (4.7) and (b) crack instantaneous velocity versus crack length for test n°1.

FIG.4.15(b) shows that the instantaneous crack velocity tends to rise when attaining the end of the conductive coating. Comparing this velocity profile with what has been reported as a crack steady-state velocity highlight some measure inconsistencies. As a matter of fact, the electrical quantities are directly collected onto the chrome layer and it is assumed that both materials (silicon and chrome) behave similarly. Nevertheless, it appears that despite the chrome brittleness, its fracture toughness under a thin film geometry is quite different and may be lower than that of the substrate. Many techniques such as micro indentation have been developed to appraise the fracture toughness of thin films [XIA 04]. Additionally, the crack position values are the results of an approximation, hence it is considered as an indirect measurement quantity that may behave differently

from one specimen to another and depending on the employed experimental conditions.

Besides, given the dimensions of the conductive chrome layer (cf. FIG.4.8(a)), the crack length is only assessed along a distance of 44mm. Therefore, one of the shortcomings of this method is the lack of information on the onset of the crack. It is inferred that the signal will vary once the crack enters the chrome layer. However, it is noteworthy to mention that monocrystalline silicon is a semiconductor, thereby the voltage variation might occur way ahead, before reaching the region of interest. Due to the complexity of the problem, some edge effects might arise and the produced effect may lead us astray when correlating the electrical signal to the crack position. To tackle this issue, a 3D numerical simulation of our specimen was performed to assess the electrical current behavior across the different layers and for various crack lengths. A thorough analysis of the results was conducted and it was observed that the current intensity in silicon remains negligible in comparison with the one going through the chrome or the gold layer. For all the reasons above, care should be taken when using the instantaneous velocity computation and when comparing it with the high-speed camera data.

Also, the average velocity along the chrome layer is around 974 m/s. By means of an optical microscope, we measured a notch length of approximately $520\mu m$ for this test. The dependency between pre-notch size and crack velocity in monocrystalline silicon was reported in the work of Wang et al. [WAN 19b]. Using the potential drop technique, the test presented herein reveals a crack velocity lower than expected in the literature. The difference can be attributed to either the effect of the conductive layer (that was supposed to be negligible), the approximation of the pre-notch measurement with optical microscopy, or the statistical nature of the brittle failure itself.

Linearized Wheatstone bridge

The same post-processing was carried out for test n°2 realized with a modified configuration of the Wheatstone bridge. We notice that the measured voltage undergoes a slow variation before swiftly reaching the failure state, in few μs. Additionally, we observe that the terminal voltage values and the wafer resistance are less disrupted (cf. FIG.4.16) than for test n°1. This linearized version of the Wheatstone bridge is more appropriate to capture the crack position once this latter reaches the end of the thin film zone. For this second test, the initial resistance is nearly 46Ω.

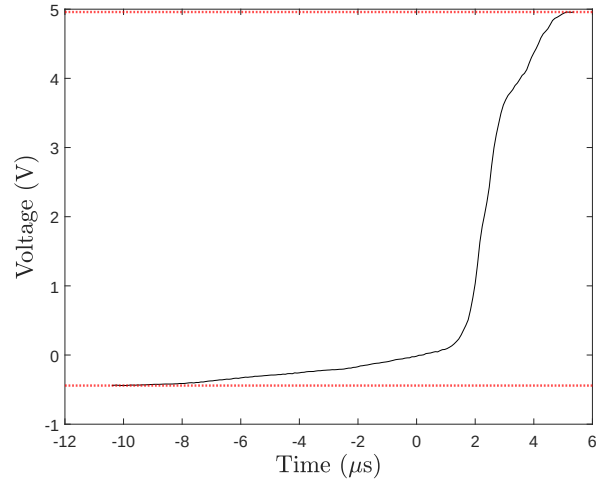

(a)

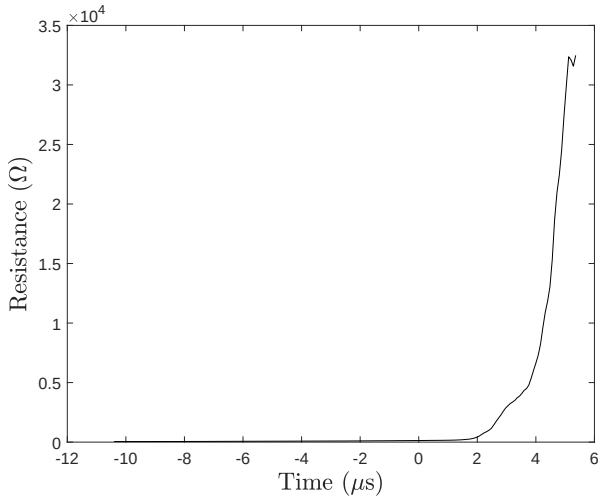

(b)

Figure 4.16: (a) Oscilloscope measurement of the wafer voltage and (b) Silicon sample resistance computed using eq. (4.3) for test n°2.

Again, the crack length versus time (cf. FIG.4.17(a)) is obtained from the resistance using Eq. 4.7 and the instantaneous crack velocity can be derived from its length (cf. FIG.4.17(b)). The crack instantaneous velocity exhibits larger variations in test n°2 than in test n°1, especially at the beginning and end of the crack propagation. The average crack speed is around 3090m/s, still beneath the Rayleigh wave velocity. Nevertheless, this value should be taken with care since the velocity varies greatly during crack propagation.

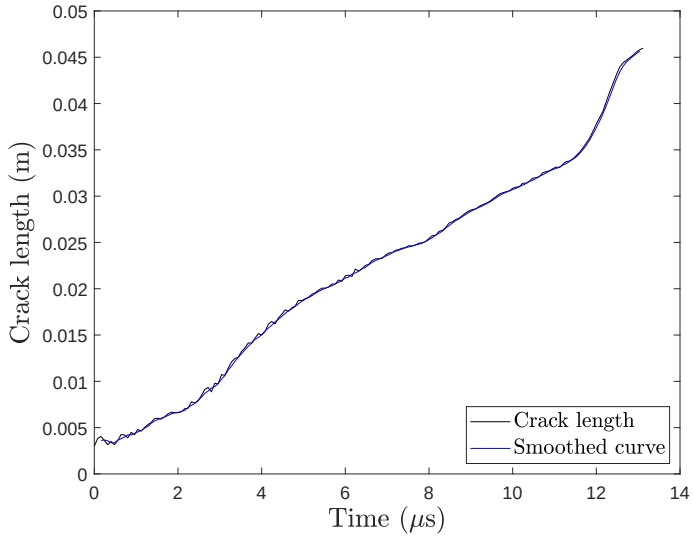

(a)

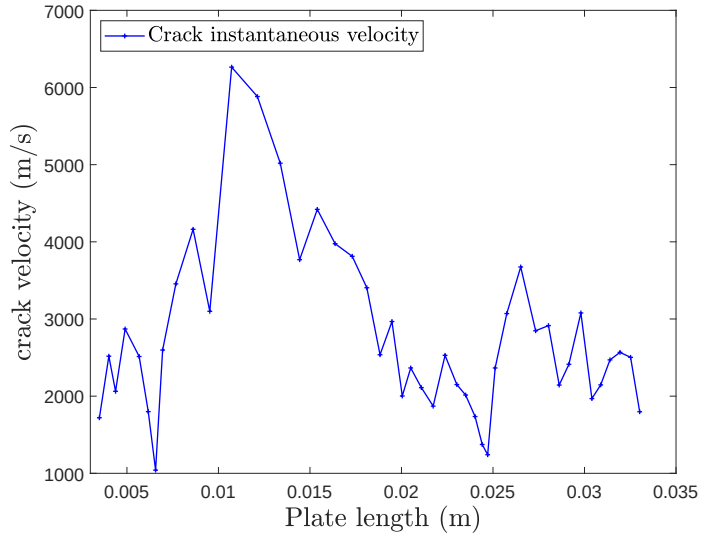

(b)

Figure 4.17: (a) Crack length versus time and (b) crack instantaneous velocity versus crack length for test n°2.

These experimental tests, using both configurations of the Wheatstone bridge, have met with ambivalent results. This outcome has motivated us to delve deeper and combine this method with the high-speed camera for a more reliable measurement of the crack speed and a more realistic correlation.

4.4 High-speed camera

While carrying on the aforementioned method, a high-speed camera was installed to record the fracture process. The ensuing video will be analyzed and its data will be post-processed via Fiji [SCH 12] and Matlab [MAT 21] software. Thereafter, the crack growth rate will be jointly compared to the one deduced from the potential drop. The main objective, herein, is to ascertain the measuring accuracy of the newly developed method. We also sought to highlight the relevance of this approach in the endeavor of detecting the two phases of crack propagation: the accelerating phase and the steady-state phase described in the work of Wang et al. [WAN 19b].

4.4.1 Experimental set-up

The bending setup is positioned in a way where the crack propagates along the downward part of the wafer. Placing the Phantom V710 camera below the specimen to record fracture mechanisms is unfeasible. Therefore, an inclined flat mirror of angle 45° is set beneath the wafer and between the two rollers of the bending assembly. The reflection of the fracture area is then grabbed by the camera located right ahead (cf. FIG.4.18).

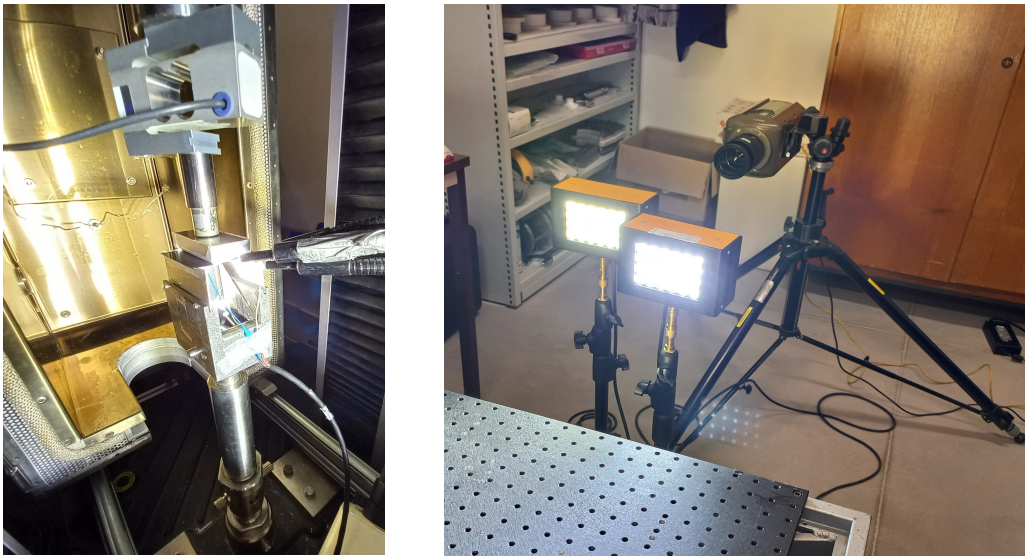

Figure 4.18: Experimental 4-line bending set-up (left) and high-speed Phantom V710 camera (right).

The continuous lighting is guaranteed by two high-intensity LEDs (MultiLED G300) positioned right in front of the camera lens and facing the sample. Additional lighting can be added beside the experimental setup. The acquisition frequency of the recorded frames is 390804 Hz and the image resolution is of 128x64 pixels. This resolution is only appointed in the case of monocrystalline silicon since it is a rectilinear propagation. Consequently, only a small region behind the notch is to be investigated. The exposure

time is 1.7 μs. Any modification of the settings is simultaneously performed via the Phantom Camera Control (PCC) software and is evaluated by judging the quality of the displayed image. It is preferable, to secure a relatively bright image before starting the test. This allows better a visualization of the crack path later on.

4.4.2 Crack velocity measurements on monocrystalline silicon

The recorded video comprises more than a hundred thousand frames. To avoid having a large file size, we visually select the set of frames covering the crack propagation phenomenon. Then, the video is unbundled and saved as a group of images under the Tiff 16 bits format. This is quite useful since this format retains most of the raw data contained in the original camera file (saved under the file extension '.cine'). It also offers a higher degree of latitude for post-processing. The images are arranged and named in ascending order according to their occurrences.

The fracture occurs along a straight line and at the onset of the centered pre-notch. Hence, only the middle part of the wafer is considered. In Fiji, all the images are cropped so as to focus on this region of interest. For this test n°3, we obtain an image resolution of 96x16.

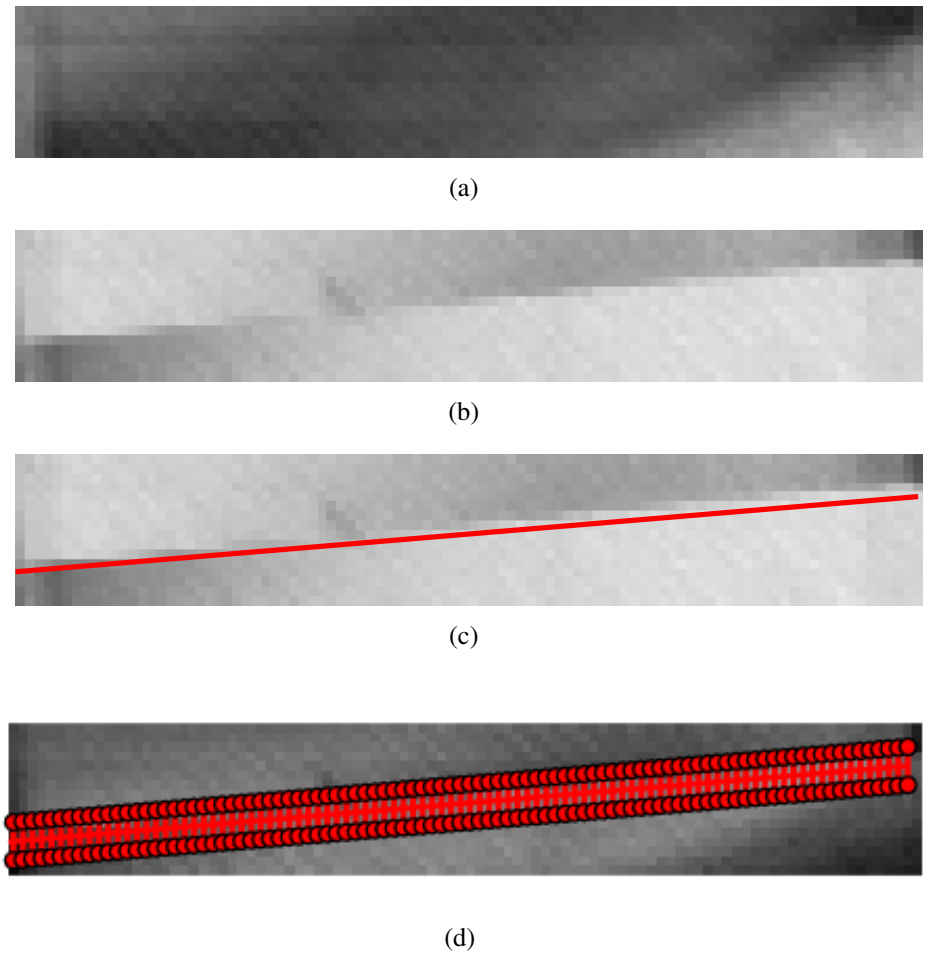

(a)

(b)

(c)

(d)

Figure 4.19: Post-processing of pictures: (a) first frame, (b) last frame, (c) last frame with crack trajectory and (d) last frame with vertical lines to locate the crack tip.

Using Matlab, we load the previously saved images. To clearly distinguish the crack path, the last frame is studied. By means of a luminosity variation, the path is visually distinguished from the rest of the picture components. As depicted in FIG.4.19(c), a straight horizontal or slightly tilted line is plotted above the crack trajectory. Then, an assortment of vertical lines is defined along the previously outlined path FIG.4.19(d). Each line covers a certain range of pixels. Their main purpose is to assess the change in the pixel values beneath them. The onset of the pixels variation is associated with the crack tip location and the corresponding frame invokes the time at which the crack has attained this position.

To obtain an accurate estimate of the crack tip position, we chose to define a spacing of 1 pixel between the vertical lines. Their length is fixed according to the lighting of the specimen. In our case, we chose to cover at least 5 pixels vertically. The pixel mean value is computed for each line and stored in a matrix.

For a given image, each vertical line is characterized by a fixed position along the crack path, referred to as the horizontal pixel coordinates. We also compute the mean value of the pixels above which it is drawn. Throughout all the selected frames, we plot the pixel value associated with each vertical line as a function of their position (cf. FIG.4.21). A threshold of 2500 is defined to locate the onset of the signal disturbances which describes the crack tip position.

By adopting this approach and post-processing camera data with Fiji and Matlab, we were able to evaluate the crack instantaneous velocity with 15 points instead of approximately 5 points as reported in the literature [WAN 19a].

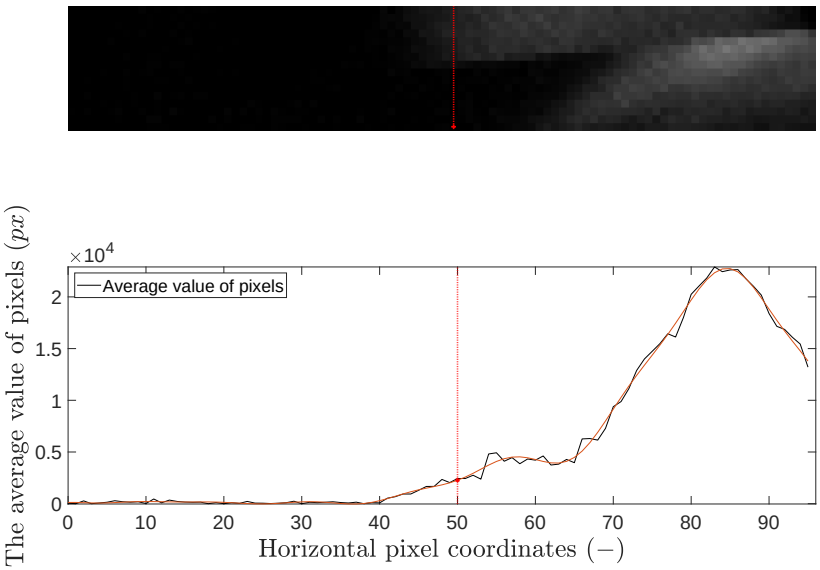

(a)

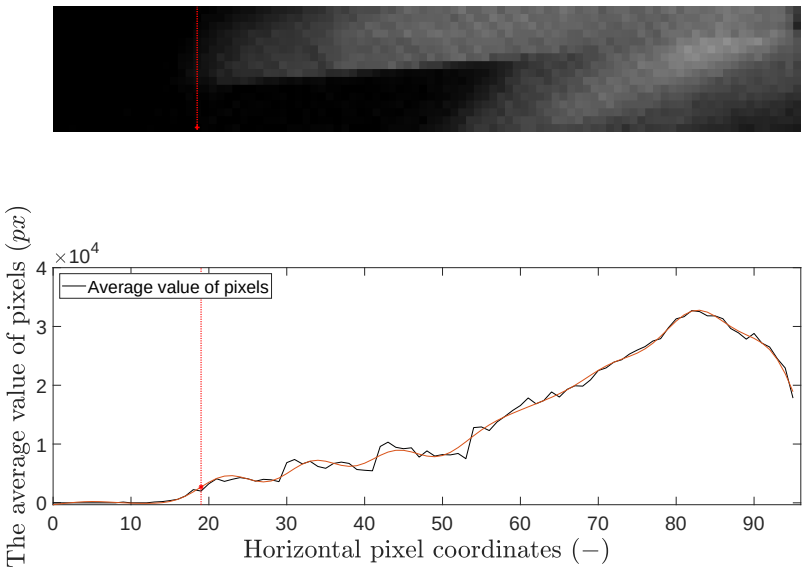

(b)

Figure 4.20: Average pixel values along the sample at two different times and crack position identification (red line).

4.4.3 Results and discussions

In order to compare the crack velocity obtained using the high-speed camera and the potential drop technique, we conduct our experiment so that both methods are performed simultaneously. Many tests were carried out but due to the brittleness of our sample and the complexity of our setup (the entanglement of the wires welded onto the plate), few were deemed successful.

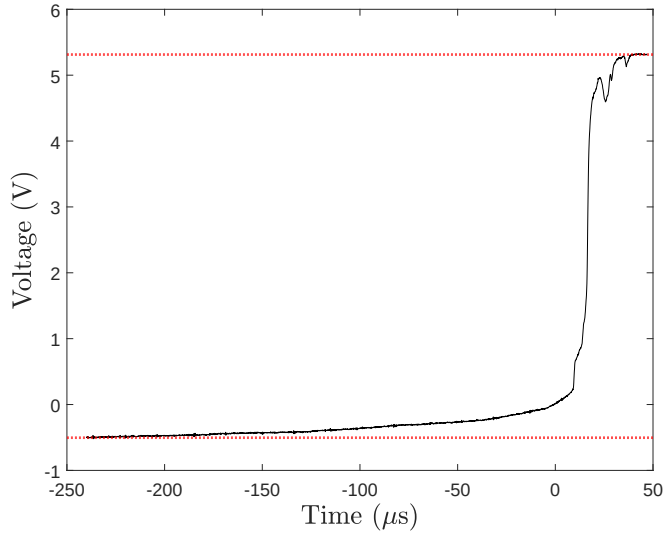

(a)

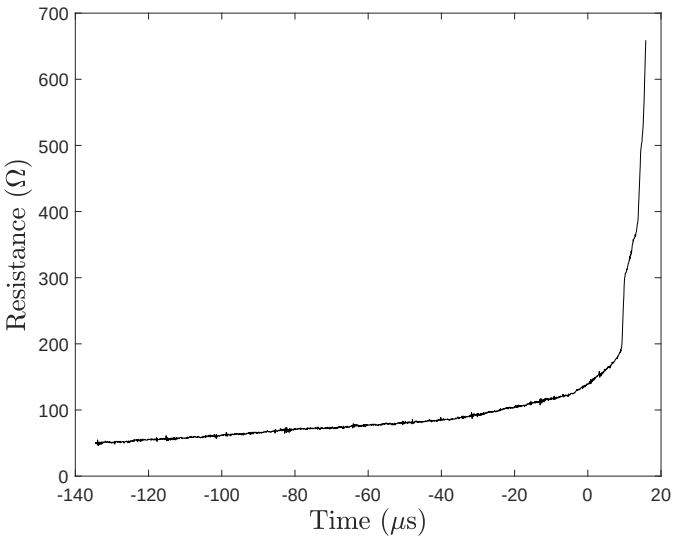

(b)

Figure 4.21: (a) Voltage across the wafer and (b) the corresponding resistance versus time for test n°3.

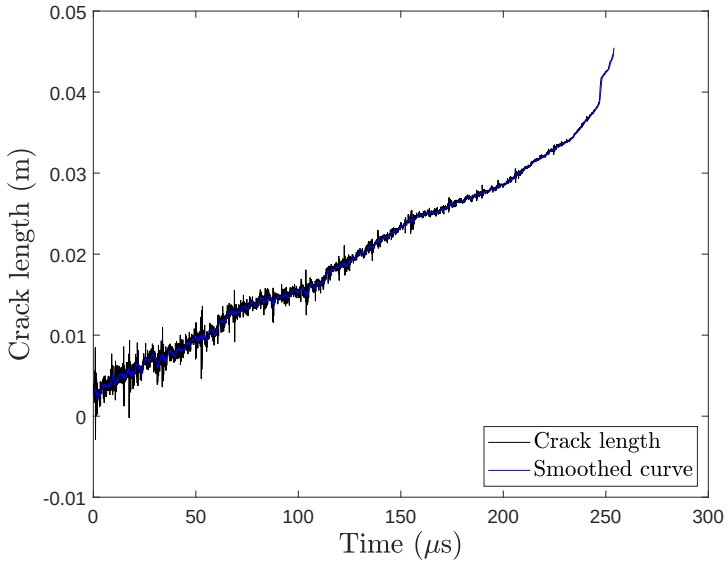

Figure 4.22: Crack length versus time with potential drop technique

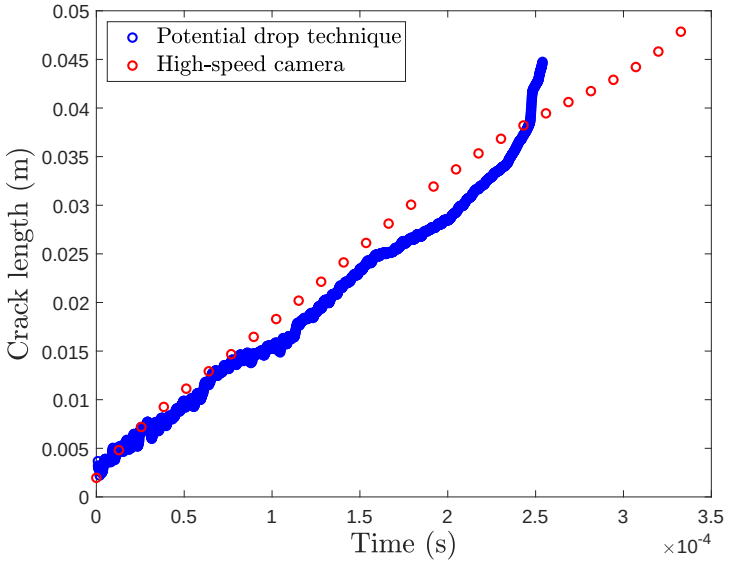

Figure 4.23: Crack length versus time obtained with both techniques.

The evolution of the crack length as a function of time is presented in FIG.4.23. With both methods, we obtain a relatively linear crack length and approximately the same average crack velocity: 150m/s with the potential drop technique and 138m/s with the high-speed camera.

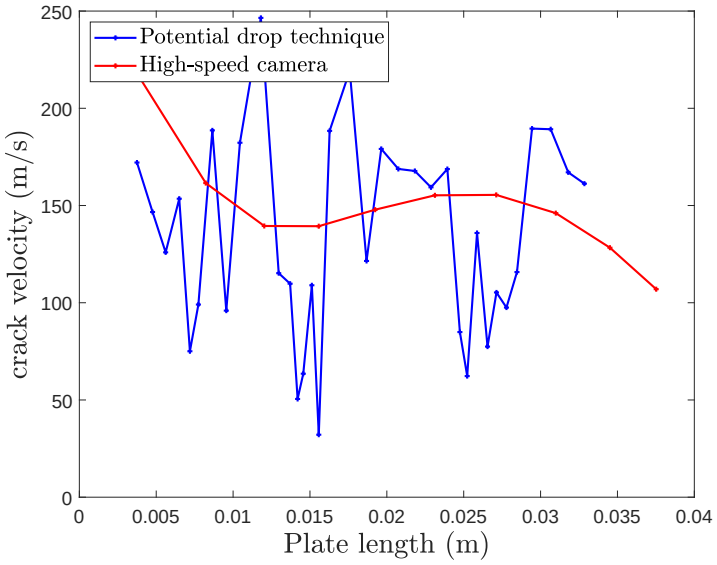

Figure 4.24: Crack instantaneous velocity versus crack propagation obtained with both techniques.

For test N°3, the instantaneous crack velocity is plotted for both methods and compared in FIG.4.24. As for the camera, the crack speed curve reveals a central steady state where the velocity is around 150m/s but both extremities are associated with either a slight acceleration or deceleration of the crack growth rate. Regarding the potential drop, the measured crack speed displays strong oscillations but remains within the same range as the one delineated by the camera. The last portion of the signal that covers the end of the propagation has been disregarded since the relationship linking crack length to the wafer resistance is not accurate and the associated velocity is flawed.

4.5 Conclusion

The disparities in results observed for both the high-speed camera and the potential drop technique can be explained in many ways. On one hand, it can be assumed that the camera measurements are more accurate and reliable. In fact, it captures several thousand images that enable crack visualization and brings a greater understanding of the physical phenomena. The image post-processing on the other hand might generate some errors according to the user viewpoint and methodology. When it comes to the electrical signal obtained using the potential drop method, interference or other environmental factors can alter the system response. Also, the existence of many cables linked to the electrical setup is liable to disturb the signal. As the wafer undergoes compression, it has been observed in some cases that by fixing the welded cables on the two electrode layers of the specimen, the wafer tends to break completely while its two parts remain in contact. Herein, the current is likely to pass by, making the endpoint of the signal undetectable.

Therefore, the previously identified inconsistencies of the crack position or velocity at the onset and the end of propagation may spring from the uncertainties brought on by the manual selection of the signal boundaries.

The work covered in this chapter focused on developing a new experimental setup for a more precise and continuous evaluation of the crack propagation speed on monocrystalline silicon. It should be pointed out that his technique proceed to a modification of our specimen surface by depositing a thin layer of a conductive material. Its material properties might be slightly modified from those of pure silicon. Since the available data omits those surface treatments, it seems incoherent to carry on a comparative analysis of our findings with the literature. Aside from the crack average velocity that was found to be comparable to the velocity obtained with a high-speed camera, the evolution of the crack growth rate remains complex to evaluate quantitatively.

Conclusion

Recent advances in numerical simulation have made it possible to predict crack initiation and its path within the structure. These findings have contributed to improving the structural performance of different systems and preventing catastrophic failures from happening. However, when it comes to crack propagation velocity, this characteristic is often perceived as less relevant to the structural engineering field. Indeed, knowing the crack speed does not provide any information on how to improve the material design or how to stop it once initiated. Even if this crack feature does not directly meet industry concerns, it has raised great interest within the scientific community. From the theoretical predictions of Freund, it was presumed that the crack will attain the Rayleigh wave speed C_r. However, in brittle failure, many studies have discovered a rather interesting property of rapidly moving cracks: the crack maximum speed only represents a substantial portion of the Rayleigh wave velocity and for said portion, it will differ from one material to another. Monocrystalline silicon undergoes cleavage fracture, which is the most extreme form of brittle failure. Its limiting velocity was found to be nearing 80% of C_r. Besides, other materials such as polymethylmetacrylate (PMMA) or glass have displayed velocities in the range of 40% to 50% of C_r. These speed measurements revealed a recurring pattern that has compelled researchers to delve deeper into the small-scale phenomena occurring in the process zone. Undoubtedly, a dissipation mechanism is preventing the crack from achieving its maximum theoretical speed value. But the question remains as to whether it stems for instance from the microstructure of the material or the interaction of the elastic waves with the moving front.

The main objective of this study was to shed light on the effects of inertia on crack growth, thus its speed. An explicit XFEM model for dynamic crack propagation was developed. The complexity of the problem and its dependence on many numerical settings has compelled us to make numerous simplifying assumptions. An analysis of the mandatory and optional model features has been carried out beforehand. The major requirements consisted in respecting the 3D aspect of our sample, computing the dynamic response of the structure using an explicit time integration scheme and eventually representing the crack using the XFEM approach.

In conjunction with the numerical developments, many experimental tests were carried out. The pre-notched monocrystalline wafers were subjected to pure bending conditions. Once the fracture stress was attained, the crack started propagating straight-

forwardly in the extension of the notch. Using either the high-speed camera or the potential drop technique (PDT), the crack length has been retrieved so we were able to characterize its speed. While the potential drop technique relies on an electrical measurement of the wafer resistance to deduce the crack front position, the high-speed camera captures a series of frames where the front location can be perceived by a change in the pixel values along the crack trajectory.

Experimental study:

On the course of this work, many experimental tests were carried out using the potential drop technique and among which only a few were deemed workable. Herein, three crack velocity measurements were presented and analyzed. To validate the accuracy and precision of the method, the last measurement was performed concurrently with the high-speed camera. Post-mortem samples were observed using optical microscopy and the pre-notch size was evaluated. For the potential drop technique, the velocity is an indirect quantity that ensues from the electrical signal, thus the voltage variation across the wafer. Using the analytical relationship between the voltage or resistance and the crack length, the velocity can be deduced. A numerical model was established to test the accuracy of this relationship. It was observed that once the crack reaches the end of the plate, both numerical and analytical values are quite disparate. This discrepancy mainly stems from edge effects that arise toward the end of the silicon sample. To correlate the pre-notch length to the measured velocity, the PDT results were compared to the ones relayed in the literature [WAN 19b]. The velocity values were of the same order (between 150 and 3000 m/s) with a difference of +/-200m/s with literature. In this regard, using the high-speed camera measurement in parallel with the PDT is necessary for a more reliable velocity measurement. The third test, which was conceived to fulfill this purpose, has shown promising results since both methods displayed a crack velocity of the same order (140-150m/s).

Besides, the PDT technique has been carried out with conductive layers on both sides of the silicon samples in order to highlight the cracking time lag between the upper and bottom faces of the wafer described in the literature [SHE 04]. However, post-processing the electrical signal was not possible due to the electrical interaction between the two circuits and the semi-conductive properties of the silicon. An outlook would be to perform a 3D simulation using finite element software to describe the crack length/voltage relationship and to quantitatively characterize the crack delay between the two free surfaces.

Numerical study:

Representing our real wafer samples using 3D elements was very cumbersome since their width are extremely small compared to their other dimensions. For the sake of assessing the accuracy and precision of the implemented codes and procedures

that govern crack propagation, all the calculations were performed on a small silicon plate of dimensions 6x7x1 mm^3 under uniaxial tension. In the course of this work, the monocrystalline silicon orthotropy has been disregarded since the crack path is already known. It grows in a straight line on the (110) plane. Griffith principle is used as the initiation criterion, where the value of the J-integral is constantly compared to the energy release rate. Once the J-integral is greater than the threshold, the excess energy is converted to newly created surfaces associated with a crack extension. To solve our dynamic problem, many explicit solvers could be used, among which the finite difference scheme has been selected. At an early stage, it has become evident that the use of both XFEM enrichment functions, singular and discontinuous, would be a daunting task when lumping the mass matrix. Hence, only the discontinuous enrichment was considered. Therefore, the crack front had to be located on the edge of the elements. This assumption alone implied that crack propagation initiates only when enough energy is stored to break the entire element. To alleviate the computational cost of the model, two successive analyses were performed. Firstly, a static implicit analysis where an increasing loading is applied. Its purpose resides in predicting the stress and strain fields of the silicon wafer under uniaxial tension, right before crack initiation. Then a dynamic analysis is solved under a constant loading, using the implemented explicit scheme and follows each crack extension and the variation of the J-integral.

The velocity is a natural outcome of the simulation since no propagation criterion has been defined. The obtained results showed a crack velocity of the same order as the Rayleigh wave speed. Additionally, the computed crack instantaneous speeds show a steady-state velocity preceded by a short acceleration phase, the same trend as the one depicted in the work of Wang et. al [WAN 19b]. However, the presented work remains purely qualitative and can not be directly compared to the conducted experiments due to the different loading conditions and the specimen geometries. Moreover, it has been notified that the computed crack velocity strongly depends on the initiation criterion. Hence it could be of interest to use the dynamic J-integral instead of the static one.

Since it is an element-to-element propagation, crack growth was discrete. Indeed, it has been observed that after each crack extension, the energy release rate decreases. Meanwhile, the crack stops since the initiation criterion is no longer fulfilled. A few steps later, it rises again to resume crack propagation. Overall, the J-integral exhibits oscillations stemming from the discrete representation of the discontinuity and the omission of the singular enrichment.

Although the presented work was purpose-built, its development relied on combining the XFEM approach with an explicit solver for three-dimensional structures. These models can be very helpful for future usage since all the procedures and operators are adjusted to address 3D crack problems. The implemented numerical model has brought promising results regarding the simulation of rapidly-moving cracks. We aimed to reveal that no propagation criterion is needed to achieve such high velocities. The use of an ex-

plicit algorithm that takes into account the rapid variation of the physical quantities along elastic wave propagation has been revealed to be a crucial requirement to capture such dynamic behavior. However, for a more quantitative comparison, thus shedding light on the limiting velocity, several aspects are to be further developed. Firstly, the wafer geometry and the loading could correspond to the experimental conditions. Therefore, the numerical crack velocity could be directly compared to the measured one. Secondly, the material orthotropy could also be considered. Apart from the elastic orthotropy, the fracture criterion is also to be modified regarding the fracture orthotropic behavior of monocrystalline silicon. Finally, adding the singular enrichment within the XFEM formulation would improve the initial model by allowing crack propagation inside the elements. A mesh refinement (without the singular enrichment) has been performed in an attempt to overcome this issue. Unfortunately, multiple evanescent waves have arisen and their interaction with the crack front has prevented the crack from propagating until the end of the specimen.

Appendix A

```
1  ******************************************************
2  ******************************************************
3  ****   PROCEDURE MASSC3D - Z.BOULAAJAJ 04/05/21   ****
4  ******************************************************
5  ******************************************************
6
7  *-----------------------------------------------------------------------
8  *-----------------------------------------------------------------------
9  * Notes :
10 *
11 *   - Calcul de la matrice de masse et sa diagonalisation en utilisant
12 *   la méthode de Menouillard
13 *
14 *-----------------------------------------------------------------------
15 *-----------------------------------------------------------------------
16
17 $$$$ MASSC3D
18
19 'DEBPROC' MASSC3D MO10*MMODEL MO21*MMODEL su_xfem0*MAILLAGE;
20
21 ************************************************************
22 ********** DEFINITION DE LA MATRICE DE MASSE  **************
23
24
25 *-------------- Matrice masse : Zone standard
26
27 MAIL1 = 'EXTR' MO10 'MAIL' ;
28 * Calcul de la matrice de masse standard
29 T_MAS1 = 'MASSE' MO10 MA10;
30 * Lumping de la matrice standard pour le maillage entier
31 T_Lump1 = 'LUMP' MO10 MA10;
32
33
34 *-------------- Matrice masse : Zone enrichi
35
36 MAIL2 = 'EXTR' MO21 'MAIL' ;
37 * Calcul de la matrice de masse standard
38 T_MAS2 = 'MASSE' MO21 MA21;
39 * Lumping de la matrice standard pour le maillage entier
40 T_Lump2 = 'LUMP' MO21 MA21;
41
42 NBEL00 = NBEL su_xfem0;
43
44 SI ( NBEL00  'NEG' 0);
45
46 *------------- Rajout des ddl enrichis en plus de T_lump2
47
48 * Extraire les valeurs de la diagonale / Creation
49 * d'un CHPOINT contenant les valeurs de la diag
50 val0 = 'EXTR' T_Lump2 'DIAG' ;
```

```
52  * Extraire la valeur de la diagonale type réel
53  val = extr (extr (exco val0 'UX')'VALE' 'SCAL') 1;
54
55  * Definition de la dim des matrices élementaires
56  * 3D et 8 noeuds pour un element standard
57
58  * Cas 3D
59  n = 3*8;
60
61  val2 = PROG n * 0.;
62
63  NN = n - 1;
64
65  * Creer une liste de reel avec val en position diag
66
67  REMPLACER val2 1 val;
68  evol1 = val2;
69
70  val2 = PROG n * 0.;
71
72  it0 = 1;
73
74  REPETER bouc1 NN;
75
76  it0 = it0 + 1;
77  REMPLACER val2 it0 val;
78
79  evol1= evol1 ET val2;
80  val2 = PROG n * 0.;
81
82  FIN bouc1;
83
84  * Construction de la matrice elementaire de l'element enrichi
85
86  * Cas 3d
87  lmot0 = 'MOTS' 'AX' 'AY' 'AZ';
88
89  * Cas 2D
90  *lmot0 = 'MOTS' 'AX' 'AY';
91
92  xfem_lump = MANU 'RIGIDITE' 'TYPE' 'MASSE' su_xfem0 lmot0 evol1;
93
94  * La matrice de rigidité totale
95
96  MASS_lump2 = T_Lump2 ET xfem_lump;
97
98  MASS_TOT = MAss_lump2 ET T_Lump1;
99
100 SINON;
101
102 MASS_TOT = T_Lump2 ET T_Lump1;
103
104 FINSI;
```

```
1  ******************************************************
2  ******************************************************
3  ****   PROCEDURE MESHXF - Z.BOULAAJAJ 04/05/21   ****
4  ******************************************************
5  ******************************************************
6  *----------------------------------------------------------------------
7  *----------------------------------------------------------------------
8  * Notes :
9  *
10 *   - Extraction du maillage enrichi ( Que les éléménts contenant la
11 *     Fissure en se basant sur la valeur des fonctions de niveaux
12 *
13 *----------------------------------------------------------------------
14 *----------------------------------------------------------------------
15
16 $$$$ MESHXF
17
18 'DEBPROC' MESHXF VTOT*MAILLAGE psi1*CHPOINT phi1*CHPOINT;
19
20 *################ MAILLAGE ENRICHIS/STANDARDS ##############*
21
22 * La condition doit porter sur les valeurs des level sets phi et psi
23 * Changement des level-sets CHPOIN en CHMAL
24
25 phi_ch = CHAN  'CHAM'  phi1 VTOT 'NOEUDS';
26 psi_ch = CHAN  'CHAM'  psi1 VTOT 'NOEUDS';
27
28 *------------------- Extraction des valeurs de psi
29
30 Y1 = MINI psi1;
31 Y2 = 1.e-15;
32
33 * il faut obligatoirement rajouter le terme STRI
34 * Pour ne considérer que les éléments avant
35
36 GEO_Y = psi_ch 'ELEM' 'COMPRIS' Y1 Y2 'STRI';
37
38 *------------------- Extraction des valeurs de phi
39
40 X1 = 0. ;
41 X2 =  MAXI phi1;
42
43 GEO_X1 = phi_ch 'ELEM' 'COMPRIS' X1 X2;
44
45 X12 = 0.;
46 X22 = MINI phi1;
47
48 GEO_X2 = phi_ch 'ELEM' 'COMPRIS' X22 X12;
49
50 GEO_X = GEO_X1 INTER GEO_X2;
51
52 *------------------- Maillage enrichi
53
54 GEO3 = GEO_X INTER GEO_Y;
55
56 'FINPROC'GEO3;
57
58 *FINP GEO3;
59
60 $$$$
```

Appendix B

Procedure *PASAPAS* - Cast3M

```
nb_couches = 2;

GTAB = tabl;
GTAB .'OBJECTIF' = MOT 'J';
GTAB .'COUCHE' = nb_couches;
GTAB .'PSI' = psi1;
GTAB .'PHI' = phi1;
GTAB .'FRONT_FISSURE' = front1 . it ;
GTAB .'MODELE' = MODTOT;
GTAB .'CARACTERISTIQUES' = MATOT;
GTAB .'SOLUTION_RESO' = DEPLA_N;
GTAB .'CHARGEMENTS_MECANIQUES' = F1;
G_THETA GTAB;
```

Psi1 & **phi1** = level sets of the actual crack front

Front1 . it = the crack front at time *t*

MODTOT = the mechanical isotropic model

MATOT = the model mechanical properties

DEPLAN = the displacement field at time *t*

F1 = The mechanical loading

Bibliography

[AHR 01] AHRENS J., BRISLAWN K., MARTIN K., GEVECI B., LAW C., PAPKA M.
Large-scale data visualization using parallel data streaming. *IEEE Computer Graphics and Applications*, vol. 21, n° 4, 2001, p. 34–41. Conference Name: IEEE Computer Graphics and Applications.

[AKS 12] AKSELROD M. S., BRUNI F. J.
Modern trends in crystal growth and new applications of sapphire. *Journal of Crystal Growth*, vol. 360, 2012, p. 134–145.

[ALB 02] ALBE K., NORDLUND K., AVERBACK R. S.
Modeling the metal-semiconductor interaction: Analytical bond-order potential for platinum-carbon. *Physical Review B*, vol. 65, n° 19, 2002, Page 195124.

[ALS 20] ALSHOAIBI A. M., FAGEEHI Y. A.
2D finite element simulation of mixed mode fatigue crack propagation for CTS specimen. *Journal of Materials Research and Technology*, vol. 9, n° 4, 2020, p. 7850–7861.

[ASA 20] ASAREH I., SONG J.-H., MULLEN R. L., QIAN Y.
A general mass lumping scheme for the variants of the extended finite element method. *International Journal for Numerical Methods in Engineering*, vol. 121, n° 10, 2020, p. 2262–2284.

[ATK 68] ATKINSON C., ESHELBY J. D.
The flow of energy into the tip of a moving crack. *International Journal of Fracture Mechanics*, vol. 4, n° 1, 1968, p. 3–8.

[ATL 85] ATLURI S. N., NISHIOKA T.
Numerical studies in dynamic fracture mechanics. *International Journal of Fracture*, vol. 27, n° 3, 1985, p. 245–261.

[BAR 57] BARNETT W. J., TROIANO A. R.
Crack propagation in the hydrogen-induced brittle fracture of steel. *JOM*, vol. 9, n° 4, 1957, p. 486–494.

[BAR 62] BARENBLATT G. I.
The mathematical theory of equilibrium cracks in brittle fracture. *Advances in Applied Mechanics*, vol. 7, 1962, p. 55–129.

[BAŽ 78] BAŽANT Z. P., GLAZIK JR J. L., ACHENBACH J. D.
Elastodynamic fields near running cracks by finite elements. *Computers & Structures*, vol. 8, n° 2, 1978, p. 193–198.

[BAZ 97] BAZANT M. Z., KAXIRAS E., JUSTO J. F.
Environment-dependent interatomic potential for bulk silicon. *Physical Review B*, vol. 56, 1997, p. 8542–8552.

[BEL 99] BELYTSCHKO T., BLACK T.
Elastic crack growth in finite elements with minimal remeshing. *International Journal for Numerical Methods in Engineering*, vol. 45, n° 5, 1999, p. 601–620.

[BEL 01] BELYTSCHKO T., MOËS N., USUI S., PARIMI C.
Arbitrary discontinuities in finite elements. *International Journal for Numerical Methods in Engineering*, vol. 50, n° 4, 2001, p. 993–1013.

[BEL 03] BELYTSCHKO T., CHEN H., XU J., ZI G.
Dynamic crack propagation based on loss of hyperbolicity and a new discontinuous enrichment. *International Journal for Numerical Methods in Engineering*, vol. 58, n° 12, 2003, p. 1873–1905.

[BLA 12] BLAL N., DARIDON L., MONERIE Y., PAGANO S.
Artificial compliance inherent to the intrinsic cohesive zone models: criteria and application to planar meshes. *International Journal of Fracture*, vol. 178, n° 1, 2012, p. 71–83.

[BOB 09] BOBARU F., YANG M., ALVES L. F., SILLING S. A., ASKARI E., XU J.
Convergence, adaptive refinement, and scaling in 1D peridynamics. *International Journal for Numerical Methods in Engineering*, vol. 77, n° 6, 2009, p. 852–877.

[BOS 06] VAN DEN BOSCH M., SCHREURS P., GEERS M.
An improved description of the exponential Xu and Needleman cohesive zone law for mixed-mode decohesion. *Engineering Fracture Mechanics*, vol. 73, n° 9, 2006, p. 1220–1234.

[BOS 08] VAN DEN BOSCH M., SCHREURS P., GEERS M.
On the development of a 3D cohesive zone element in the presence of large deformations. *Computational Mechanics*, vol. 42, n° 2, 2008, p. 171–180.

[BOU 00] BOURDIN B., FRANCFORT G. A., MARIGO J.-J.
Numerical experiments in revisited brittle fracture. *Journal of the Mechanics and Physics of Solids*, vol. 48, n° 4, 2000, p. 797–826.

[BOU 08] BOURDIN B., FRANCFORT G. A., MARIGO J.-J.
The variational approach to fracture. *Journal of Elasticity*, vol. 91, n° 1, 2008, p. 5–148.

[BOW 67] BOWDEN F., BRUNTON J., FIELD J., HEYES A.
Controlled fracture of brittle solids and interruption of electrical current. *Nature*, vol. 216, n° 5110, 1967, p. 38–42.

[BUI 77] BUI H. D.
Mécanique de la rupture fragile, 1977.

[CAR 20] CARTON L.
Mechanical properties of thin silicon wafers for photovoltaic applications : Influence of material quality and sawing process. Ph.D., INSA Lyon, 2020.

[CAS 21] CAST3M
Finite element software developed by the French Atomic Energy Center (CEA), 2021.

[CHA 01] CHABOCHE J. L., FEYEL F., MONERIE Y.
Interface debonding models: a viscous regularization with a limited rate dependency. *International Journal of Solids and Structures*, vol. 38, n° 18, 2001, p. 3127–3160.

[CHE 67] CHEREPANOV G. P.
Crack propagation in continuous media: PMM vol. 31, no. 3, 1967, pp. 476–488. *Journal of Applied Mathematics and Mechanics*, vol. 31, n° 3, 1967, p. 503–512.

[COU 28] COURANT R., FRIEDRICHS K., LEWY H.
Über die partiellen Differenzengleichungen der mathematischen Physik. *Mathematische Annalen*, vol. 100, n° 1, 1928, p. 32–74.

[CZO 18] CZOCHRALSKI J.
Ein neues Verfahren zur Messung der Kristallisationsgeschwindigkeit der Metalle. *Zeitschrift für Physikalische Chemie*, vol. 92U, n° 1, 1918, p. 219–221.

[DEB 96] DEBRUYNE G.
A Lagrangian description of the moving crack problem. *Advances in Fracture Resistance in Materials*, vol. 2, 1996, p. 273–280.

[DOY 13] DOYEN D., ERN A., PIPERNO S.
Quasi-explicit time-integration schemes for dynamic fracture with set-valued cohesive zone models. *Computational Mechanics*, vol. 52, n° 2, 2013, p. 401–416.

[DUB 13] DUBOIS F., MOZUL R.
Lmgc90. *11e Colloque National en Calcul des Structures*, 2013.

[DUG 60] DUGDALE D. S.
Yielding of steel sheets containing slits. *Journal of the Mechanics and Physics of Solids*, vol. 8, n° 2, 1960, p. 100–104.

[ELI 02] ELICES M., GUINEA G. V., GÓMEZ J., PLANAS J.
The cohesive zone model: advantages, limitations and challenges. *Engineering Fracture Mechanics*, vol. 69, n° 2, 2002, p. 137–163.

[ERD 63] ERDOGAN F., SIH G. C.
On the Crack Extension in Plates Under Plane Loading and Transverse Shear. *Journal of Basic Engineering*, vol. 85, n° 4, 1963, p. 519–525.

[FAN 19] FAN Z., WANG Y., GU X., QIAN P., SU Y., ALA-NISSILA T.
A minimal Tersoff potential for diamond silicon with improved descriptions of elastic and phonon transport properties. *Journal of Physics: Condensed Matter*, vol. 32, n° 13, 2019, Page 135901.

[FIN 99] FINEBERG J., MARDER M.
Instability in dynamic fracture. *Physics Reports*, vol. 313, n° 1, 1999, p. 1–108.

[FRA 98] FRANCFORT G. A., MARIGO J.-J.
Revisiting brittle fracture as an energy minimization problem. *Journal of the Mechanics and Physics of Solids*, vol. 46, n° 8, 1998, p. 1319–1342.

[FRE 72] FREUND L.
Energy flux into the tip of an extending crack in an elastic solid. *Journal of Elasticity*, vol. 2, n° 4, 1972, p. 341–349.

[FRE 90] FREUND L. B.
Dynamic Fracture Mechanics. Cambridge Monographs on Mechanics, 1990.

[FRE 08] FREED Y., BANKS-SILLS L.
A new cohesive zone model for mixed mode interface fracture in bimaterials. *Engineering Fracture Mechanics*, vol. 75, n° 15, 2008, p. 4583–4593.

[GOL 74] GOL'DSTEIN R. V., SALGANIK R. L.
Brittle fracture of solids with arbitrary cracks. *International Journal of Fracture*, vol. 10, n° 4, 1974, p. 507–523.

[GRA 02] GRAVOUIL A., MOËS N., BELYTSCHKO T.
Non-planar 3D crack growth by the extended finite element and level sets—Part II: Level set update. *International Journal for Numerical Methods in Engineering*, vol. 53, n° 11, 2002, p. 2569–2586.

[GRI 21] GRIFFITH A. A.
VI. The phenomena of rupture and flow in solids. *Philosophical transactions of the royal society of london. Series A, containing papers of a mathematical or physical character*, vol. 221, n° 582-593, 1921, p. 163–198.

[HA 10] HA Y. D., BOBARU F.
Studies of dynamic crack propagation and crack branching with peridynamics. *International Journal of Fracture*, vol. 162, n° 1, 2010, p. 229–244.

[HES 93] HESKETH P. J., JU C., GOWDA S., ZANORIA E., DANYLUK S.
Surface Free Energy Model of Silicon Anisotropic Etching. *Journal of The Electrochemical Society*, vol. 140, n° 4, 1993, Page 1080.

[HIL 76] HILLERBORG A., MODÉER M., PETERSSON P.-E.
Analysis of crack formation and crack growth in concrete by means of fracture mechanics and finite elements. *Cement and Concrete Research*, vol. 6, n° 6, 1976, p. 773–781.

[HOF 78] HOFFMANN A., LIVOLANT M., ROCHE R.
CASTEM: a system of finite element computer programs for elastic and inelastic analysis of mechanical structures of reactors. rapport, 1978, CEA Centre d'Etudes Nucleaires de Saclay.

[HOL 98] HOLLAND D., MARDER M.
Ideal brittle fracture of silicon studied with molecular dynamics. *Physical Review Letters*, vol. 80, n° 4, 1998, Page 746.

[HU 21] HU X., HUANG X., YAO W., ZHANG P.
Precise integration explicit phase field method for dynamic brittle fracture. *Mechanics Research Communications*, vol. 113, 2021, Page 103698.

[HUG 79] HUGHES T. J., PISTER K. S., TAYLOR R. L.
Implicit-explicit finite elements in nonlinear transient analysis. *Computer Methods in Applied Mechanics and Engineering*, vol. 17, 1979, p. 159–182.

[HUG 87] HUGHES T.
The Finite Element Method: Linear Static and Dynamic Finite Element Analysis, 1987.

[ING 13] INGLIS C. E.
Stresses in a plate due to the presence of cracks and sharp corners. *Transactions of the Royal Institution of Naval Architects*, vol. 55, 1913, p. 219–241.

[ING 77] INGRAFFEA A.
Nodal grafting for crack propagation studies. *International Journal for Numerical Methods in Engineering*, vol. 11, n° 7, 1977, p. 1185–1187.

[IRW 21] IRWIN G. R.
Analysis of Stresses and Strains Near the End of a Crack Traversing a Plate. *Journal of Applied Mechanics*, vol. 24, n° 3, 2021, p. 361–364.

[KAM 18] KAMENSKY D., MOUTSANIDIS G., BAZILEVS Y.
Hyperbolic phase field modeling of brittle fracture: Part I—theory and simulations. *Journal of the Mechanics and Physics of Solids*, vol. 121, 2018, p. 81–98.

[KAN 88] KANNINEN M. F., POPELAR C. A., SAUNDERS H.
Advanced Fracture Mechanics. *Journal of Vibration, Acoustics, Stress, and Reliability in Design*, vol. 110, n° 3, 1988, p. 419-420.

[KEE 76] KEEGSTRA P.
A transient finite element crack propagation model for nuclear pressure vessel steels. *Journal of the Institution of Nuclear Engineers*, vol. 17, n° 4, 1976, p. 89–96.

[KIM 12] KIM W.-J., LEE J.-M., KIM J.-S., LEE C. J.
Measuring high speed crack propagation in concrete fracture test using mechanoluminescent material. *Smart Structures and Systems*, vol. 10, n° 6, 2012, p. 547–555.

[KUB 03] KUBAIR D. V., GEUBELLE P. H.
Comparative analysis of extrinsic and intrinsic cohesive models of dynamic fracture. *International Journal of Solids and Structures*, vol. 40, n° 15, 2003, p. 3853–3868.

[KUH 08] KUHN C., MÜLLER R.
A phase field model for fracture. *PAMM: Proceedings in Applied Mathematics and Mechanics*, vol. 8, 2008, p. 10223–10224.

[LI 05] LI X., KASAI T., NAKAO S., ANDO T., SHIKIDA M., SATO K., TANAKA H.
Anisotropy in fracture of single crystal silicon film characterized under uniaxial tensile condition. *Sensors and Actuators A: Physical*, vol. 117, n° 1, 2005, p. 143–150.

[LI 16] LI Y., GAN F., WAN Z., LIAO J.
An SVM approach with alternating current potential drop technique to classify pits and cracks on the bottom of a metal plate. *AIP Advances*, vol. 6, n° 9, 2016, Page 095202.

[MAC 07] MACEK R. W., SILLING S. A.
Peridynamics via finite element analysis. *Finite Elements in Analysis and Design*, vol. 43, n° 15, 2007, p. 1169–1178.

[MAD 18] MADENCI E., DORDUNCU M., BARUT A., PHAN N.
A state-based peridynamic analysis in a finite element framework. *Engineering Fracture Mechanics*, vol. 195, 2018, p. 104–128.

[MAS 13] MASOLIN A., BOUCHARD P.-O., MARTINI R., BERNACKI M.
Thermo-mechanical and fracture properties in single-crystal silicon. *Journal of Materials Science*, vol. 48, n° 3, 2013, p. 979–988.

[MAT 21] MATLAB
version 9.11 (R2021b), Natick, Massachusetts, 2021.

[MEL 96] MELENK J. M., BABUŠKA I.
The partition of unity finite element method: basic theory and applications. *Computer Methods in Applied Mechanics and Engineering*, vol. 139, n° 1-4, 1996, p. 289–314.

[MEN 06] MENOUILLARD T., RETHORE J., COMBESCURE A., BUNG H.
Efficient explicit time stepping for the eXtended Finite Element Method (X-FEM). *International Journal for Numerical Methods in Engineering*, vol. 68, n° 9, 2006, p. 911–939.

[MEN 07] MENOUILLARD T.
Dynamique explicite pour la simulation numérique de propagation de fissure par la méthode des éléments finis étendus. Ph.D., Lyon, INSA, 2007.

[MEN 08] MENOUILLARD T., RÉTHORÉ J., MOËS N., COMBESCURE A., BUNG H.
Mass lumping strategies for X-FEM explicit dynamics: Application to crack propagation. *International Journal for Numerical Methods in Engineering*, vol. 74, n° 3, 2008, p. 447–474.

[MIE 10] MIEHE C., WELSCHINGER F., HOFACKER M.
Thermodynamically consistent phase-field models of fracture: Variational principles and multi-field FE implementations. *International Journal for Numerical Methods in Engineering*, vol. 83, n° 10, 2010, p. 1273–1311.

[MIS 11] MISSOUM-BENZIANE D., CHIARUTTINI V., GARAUD J.-D., FEYEL F., FOERCH R., OSIPOV N., QUILICI S., RANNOU J., ROOS A., RYCKELYNCK D.
Z-set/ZeBuLoN: une suite logicielle pour la mécanique des matériaux et le calcul de structures. *10e Colloque National en Calcul des Structures*, 2011, p. 8–9.

[MOË 99] MOËS N., DOLBOW J., BELYTSCHKO T.
A finite element method for crack growth without remeshing. *International Journal for Numerical Methods in Engineering*, vol. 46, n° 1, 1999, p. 131–150.

[MOL 17] MOLNÁR G., GRAVOUIL A.
2D and 3D Abaqus implementation of a robust staggered phase-field solution for modeling brittle fracture. *Finite Elements in Analysis and Design*, vol. 130, 2017, p. 27–38.

[MOL 20] MOLNÁR G., GRAVOUIL A., SEGHIR R., RÉTHORÉ J.
An open-source Abaqus implementation of the phase-field method to study the effect of plasticity on the instantaneous fracture toughness in dynamic crack propagation. *Computer Methods in Applied Mechanics and Engineering*, vol. 365, 2020, Page 113004.

[MOR 19] DE MORAIS A.
Evaluation of a trilinear traction-separation law for mode II delamination using the effective crack method. *Composites Part A: Applied Science and Manufacturing*, vol. 121, 2019, p. 74–83.

[MOT 48] MOTT N. F.
Brittle fracture in mild steel plates. *Engineering*, vol. 165, 1948, p. 16–18.

[MTS 14] MTS C.
MTS Criterion Series 40 Product Manual, Eden Prairie, Minnesota, 2011-2014.

[NEE 87] NEEDLEMAN A.
A continuum model for void nucleation by inclusion debonding. *Journal of Applied Mechanics*, vol. 54, n° 3, 1987, p. 525–531.

[NEW 59] NEWMARK N. M.
A Method of Computation for Structural Dynamics. *Journal of the Engineering Mechanics Division*, vol. 85, n° 3, 1959, p. 67–94.

[NIS 05] NISTOR I., PANTALÉ O., CAPERAA S.
On the modeling of the dynamic crack propagation by extended finite element method: numerical implementation in dynela code. Citeseer, 2005.

[NIS 06] NISTOR I., CAPERAA S., PANTALE O.
A Dynamic Crack Propagation Criteria for XFEM, Based on Path-Independent Integral Evaluation. *Fracture of Nano and Engineering Materials and Structures*, p. 943–944, 2006.

[OSH 88] OSHER S., SETHIAN J. A.
Fronts propagating with curvature-dependent speed: Algorithms based on Hamilton-Jacobi formulations. *Journal of Computational Physics*, vol. 79, n° 1, 1988, p. 12–49.

[PAR 09] PARK K., PAULINO G. H., ROESLER J. R.
A unified potential-based cohesive model of mixed-mode fracture. *Journal of the Mechanics and Physics of Solids*, vol. 57, n° 6, 2009, p. 891–908.

[PÉR 00] PÉREZ R., GUMBSCH P.
An ab initio study of the cleavage anisotropy in silicon. *Acta Materialia*, vol. 48, n° 18, 2000, p. 4517–4530.

[PER 10] PERALES F., DUBOIS F., MONERIE Y., PIAR B., STAINIER L.
Multi-body NSCD strategy as a multi-domain solver. Application to code coupling dedicated to the modeling of fracture of heterogeneous media. *European Journal of Computational Mechanics*, vol. 19, 2010, p. 389–417.

[PET 99] PETTIFOR D., OLEINIK I.
Analytic bond-order potentials beyond Tersoff-Brenner. I. Theory. *Physical Review B*, vol. 59, n° 13, 1999, Page 8487.

[RAJ 10] RAJA M. K., MAHADEVAN S., RAO B. P. C., BEHERA S. P., JAYAKUMAR T., RAJ B.
Influence of crack length on crack depth measurement by an alternating current potential drop technique. *Measurement Science and Technology*, vol. 21, n° 10, 2010, Page 105702.

[REN 19] REN H., ZHUANG X., ANITESCU C., RABCZUK T.
An explicit phase field method for brittle dynamic fracture. *Computers & Structures*, vol. 217, 2019, p. 45–56.

[RIC 68] RICE J. R.
A Path Independent Integral and the Approximate Analysis of Strain Concentration by Notches and Cracks. *Journal of Applied Mechanics*, vol. 35, n° 2, 1968, p. 379–386.

[RIC 12] RICHEFEU V., CHRYSOCHOOS A., HUON V., MONERIE Y., PEYROUX R., WATTRISSE B.
Toward local identification of cohesive zone models using digital image correlation. *European Journal of Mechanics - A/Solids*, vol. 34, 2012, p. 38–51.

[ROK 18] ROKKAM S. K., TRUONG Q. T., GUNZBURGER M., GOEL K.
A peridynamics-FEM approach for crack path prediction in fiber-reinforced composites. *2018 AIAA/ASCE/AHS/ASC Structures, Structural Dynamics, and Materials Conference*, 2018, Page 651.

[ROS 81] ROSE J. H., FERRANTE J., SMITH J. R.
Universal binding energy curves for metals and bimetallic interfaces. *Physical Review Letters*, vol. 47, n° 9, 1981, Page 675.

[ROZ 08] ROZYCKI P., MOËS N., BECHET E., DUBOIS C.
X-FEM explicit dynamics for constant strain elements to alleviate mesh constraints on internal or external boundaries. *Computer Methods in Applied Mechanics and Engineering*, vol. 197, n° 5, 2008, p. 349–363.

[SAM 02] SAMUDRALA O., HUANG Y., ROSAKIS A.
Subsonic and intersonic mode II crack propagation with a rate-dependent cohesive zone. *Journal of the Mechanics and Physics of Solids*, vol. 50, n° 6, 2002, p. 1231–1268.

[SCH 26] SCHRÖDINGER E.
An undulatory theory of the mechanics of atoms and molecules. *Physical Review*, vol. 28, n° 6, 1926, Page 1049.

[SCH 59] SCHARDIN H. et al.
Velocity effects in fracture. , 1959.

[SCH 03] SCHEIDER I., BROCKS W.
The effect of the traction separation law on the results of cohesive zone crack propagation analyses. *Key Engineering Materials*, vol. 251, 2003, p. 313–318.

[SCH 12] SCHINDELIN J., ARGANDA-CARRERAS I., FRISE E., KAYNIG V., LONGAIR M., PIETZSCH T., PREIBISCH S., RUEDEN C., SAALFELD S., SCHMID B., TINEVEZ J.-Y., WHITE D. J., HARTENSTEIN V., ELICEIRI K., TOMANCAK P., CARDONA A.
Fiji: an open-source platform for biological-image analysis. *Nature Methods*, vol. 9, n° 7, 2012, p. 676–682.

[SET 99] SETHIAN J. A.
Level set methods and fast marching methods: evolving interfaces in computational geometry, fluid mechanics, computer vision, and materials science, vol. 3, 1999.

[SHE 85] SHEPHARD M. S., YEHIA N. A., BURD G. S., WEIDNER T. J.
Automatic crack propagation tracking. *Advances and Trends in Structures and Dynamics*, p. 211–223, 1985.

[SHE 04] SHERMAN D., BE'ERY I.
Dislocations deflect and perturb dynamically propagating cracks. *Physical Review Letters*, vol. 93, n° 26 Pt 1, 2004, Page 265501.

[SIH 74] SIH G. C.
Strain-energy-density factor applied to mixed mode crack problems. *International Journal of Fracture*, vol. 10, n° 3, 1974, p. 305–321.

[SIL 00] SILLING S. A.
Reformulation of elasticity theory for discontinuities and long-range forces. *Journal of the Mechanics and Physics of Solids*, vol. 48, n° 1, 2000, p. 175–209.

[SIL 05] SILLING S. A., ASKARI E.
A meshfree method based on the peridynamic model of solid mechanics. *Computers & Structures*, vol. 83, n° 17-18, 2005, p. 1526–1535.

[SIL 07] SILLING S. A., EPTON M., WECKNER O., XU J., ASKARI E.
Peridynamic states and constitutive modeling. *Journal of Elasticity*, vol. 88, n° 2, 2007, p. 151–184.

[SIL 08] SILLING S. A., LEHOUCQ R. B.
Convergence of peridynamics to classical elasticity theory. *Journal of Elasticity*, vol. 93, n° 1, 2008, p. 13–37.

[SLE 10] SLEPYAN L.
Wave radiation in lattice fracture. *Acoustical Physics*, vol. 56, n° 6, 2010, p. 962–971.

[SMI 09] SMITH M.
ABAQUS/Standard User's Manual, Version 6.9. , 2009.

[SON 09] SONG J.-H., BELYTSCHKO T.
Cracking node method for dynamic fracture with finite elements. *International Journal for Numerical Methods in Engineering*, vol. 77, n° 3, 2009, p. 360–385.

[STI 85] STILLINGER F. H., WEBER T. A.
Computer simulation of local order in condensed phases of silicon. *Physical Review B*, vol. 31, n° 8, 1985, Page 5262.

[STO 01] STOLARSKA M., CHOPP D. L., MOËS N., BELYTSCHKO T.
Modelling crack growth by level sets in the extended finite element method. *International Journal for Numerical Methods in Engineering*, vol. 51, n° 8, 2001, p. 943–960.

[STR 57] STROH A. N.
A theory of the fracture of metals. *Advances in Physics*, vol. 6, n° 24, 1957, p. 418–465.

[SUK 01] SUKUMAR N., CHOPP D. L., MOËS N., BELYTSCHKO T.
Modeling holes and inclusions by level sets in the extended finite-element method. *Computer Methods in Applied Mechanics and Engineering*, vol. 190, n° 46-47, 2001, p. 6183–6200.

[TER 88] TERSOFF J.
Empirical interatomic potential for silicon with improved elastic properties. *Physical Review B*, vol. 38, n° 14, 1988, Page 9902.

[TER 89] TERSOFF J.
Modeling solid-state chemistry: Interatomic potentials for multicomponent systems. *Physical Review B*, vol. 39, n° 8, 1989, Page 5566.

[TIJ 00] TIJSSENS M., VAN DER GIESSEN E., SLUYS L.
Modeling of crazing using a cohesive surface methodology. *Mechanics of Materials*, vol. 32, n° 1, 2000, p. 19–35.

[TRÄ 98] TRÄDEGÅRD A., NILSSON F., ÖSTLUND S.
FEM-remeshing technique applied to crack growth problems. *Computer Methods in Applied Mechanics and Engineering*, vol. 160, n° 1-2, 1998, p. 115–131.

[WAN 19a] WANG M.
Dynamic fracture of solar grade single crystalline silicon wafers. Ph.D., INSA Lyon, 2019.

[WAN 19b] WANG M., ZHAO L., FOURMEAU M., NELIAS D.
Crack plane deflection and shear wave effects in the dynamic fracture of silicon single crystal. *Journal of the Mechanics and Physics of Solids*, vol. 122, 2019, p. 472–488.

[WAN 19c] WANG T., YE X., LIU Z., CHU D., ZHUANG Z.
Modeling the dynamic and quasi-static compression-shear failure of brittle materials by explicit phase field method. *Computational Mechanics*, vol. 64, n° 6, 2019, p. 1537–1556.

[WAN 20] WANG T., YE X., LIU Z., LIU X., CHU D., ZHUANG Z.
A phase-field model of thermo-elastic coupled brittle fracture with explicit time integration. *Computational Mechanics*, vol. 65, n° 5, 2020, p. 1305–1321.

[WAW 89] WAWRZYNEK P. A., INGRAFFEA A. R.
An interactive approach to local remeshing around a propagating crack. *Finite Elements in Analysis and Design*, vol. 5, n° 1, 1989, p. 87–96.

[WES 21] WESTERGAARD H. M.
Bearing Pressures and Cracks: Bearing Pressures Through a Slightly Waved Surface or Through a Nearly Flat Part of a Cylinder, and Related Problems of Cracks. *Journal of Applied Mechanics*, vol. 6, n° 2, 2021, p. A49–A53.

[WU 78] WU C. H.
Maximum-energy-release-rate criterion applied to a tension-compression specimen with crack. *Journal of Elasticity*, vol. 8, n° 3, 1978, p. 235–257.

[XIA 04] XIA Z., CURTIN W. A., SHELDON B. W.
A new method to evaluate the fracture toughness of thin films. *Acta Materialia*, vol. 52, n° 12, 2004, p. 3507–3517.

[XU 94] XU X.-P., NEEDLEMAN A.
Numerical simulations of fast crack growth in brittle solids. *Journal of the Mechanics and Physics of Solids*, vol. 42, n° 9, 1994, p. 1397–1434.

[YAG 77] YAGAWA G., SAKAI Y., ANDO Y.
Analysis of a rapidly propagating crack using finite elements. *Fast fracture and crack arrest*, vol. 627, p. 109–122, 1977.

[YAH 18] YAHYA N., LYTWYN M.
The use of bilinear cohesive zone model to study the fracture of mode I in adhesive joints. *International Journal of Engineering and Innovative Technology*, vol. 5, n° 1, 2018.

[ZHA 08] ZHANG Z., PAULINO G. H., CELES W.
Cohesive modeling of dynamic crack growth in homogeneous and functionally graded materials. *AIP Conference Proceedings*, vol. 973, 2008, p. 562–567.

[ZHA 16] ZHAO L.
On the fracture of solar grade crystalline silicon wafer. Ph.D., INSA Lyon, 2016.

[ZHA 18] ZHAO L., BARDEL D., MAYNADIER A., NELIAS D.
Velocity correlated crack front and surface marks in single crystalline silicon. *Nature Communications*, vol. 9, n° 1, 2018, Page 1298.

[ZHA 21a] ZHANG P., YAO W., HU X., BUI T. Q.
An explicit phase field model for progressive tensile failure of composites. *Engineering Fracture Mechanics*, vol. 241, 2021, Page 107371.

[ZHA 21b] ZHANG P., YAO W., HU X., ZHUANG X.
Phase field modelling of progressive failure in composites combined with cohesive element with an explicit scheme. *Composite Structures*, vol. 262, 2021, Page 113353.

[ZHO 05] ZHOU F., MOLINARI J.-F., SHIOYA T.
A rate-dependent cohesive model for simulating dynamic crack propagation in brittle materials. *Engineering Fracture Mechanics*, vol. 72, n° 9, 2005, p. 1383–1410.

FOLIO ADMINISTRATIF

THÈSE SOUTENUE DEVANT L'INSTITUT NATIONAL DES SCIENCES APPLIQUÉES DE LYON

NOM: BOULAAJAJ DATE de SOUTENANCE: 03/03/2023

Prénom: Zineb

TITRE: Numerical and experimental study of crack propagation on monocrystalline silicon wafers

NATURE: Doctorat Numéro d'ordre: 2023ISAL0015

École doctorale: MEGA (ED162)

Spécialité: Génie Mécanique

RÉSUMÉ:
La défaillance mécanique est un phénomène critique affectant les performances électriques du silicium monocristallin, couramment utilisé dans les cellules photovoltaïques et les systèmes micro électromécaniques. La rupture fragile dynamique des composants Si est principalement causée par la présence de fissures. De nombreuses études ont été menées pour appréhender les tendances d'une rupture fragile par clivage. D'un point de vue expérimental, il s'avère que la propagation des fissures dans le silicium monocristallin peut atteindre jusqu'à 80% de la vitesse des ondes de Rayleigh. Cette vitesse limite a soulevé de nombreuses questions quant à sa dépendance vis-à-vis de la microstructure et des phénomènes dissipatifs survenant en pointe de fissure.
Dans le cadre des efforts déployés pour élucider le caractère dynamique des fissures, une étude numérique est réalisée afin de prédire leur vitesse de propagation et son évolution au cours du temps. Les effets inertiels sont pris en compte à l'aide d'un schéma d'intégration explicite. Une étude préliminaire a d'abord été menée dans le but de définir tous les paramètres numériques qui pourraient intervenir et influer sur l'apparition et l'évolution de la discontinuité mobile. Initialement, nous avions pour objectif de reproduire les essais expérimentaux, ainsi un modèle tridimensionnel s'avérait indispensable. L'approche XFEM a été utilisée afin de simuler les fissures et le modèle 3D explicite a été implémenté sur le code open source Cast3m.
Vu la rapidité du phénomène et la géométrie de nos échantillons, la caractérisation fine de la vitesse des fissures représente un enjeu de taille. Pour ce faire, une série de mesure par couches minces a été effectuée. Les échantillons sont des wafers en silicium monocristallin préparés préalablement en déposant sur leurs surfaces une mince couche de chrome et des électrodes en or. Afin de contrôler la trajectoire de la fissure, une pré-entaille a été faite à la main sur chaque wafer. Le circuit électrique est un pont de Wheatstone constitué de 4 résistances, où l'une est remplacée par un wafer et d'une pile alimentant l'ensemble. L'extension de la fissure entraîne un changement notable dans la mesure de tension. Une relation entre la tension et la position du front de fissure nous permet de déduire la vitesse de propagation. Cette configuration expérimentale à très haute fréquence est ensuite validée en effectuant simultanément les mêmes mesures à l'aide d'une caméra rapide.

MOTS-CLÉS: XFEM, rupture fragile, dynamique, fissuration 3 D, méthode de mesure par couches minces, vitesse de propagation, caméra rapide.

Laboratoire de recherche: Laboratoire de Mécanique des Contacts et des Structures
UMR CNRS 5259 - INSA de Lyon
18-20 rue des Sciences
69621 Villeurbanne Cedex FRANCE

Directeur de thèse: NELIAS Daniel

Président du jury: à déterminer

Composition du jury: BONAMY Daniel
PRABEL Benoit
NELIAS Daniel
MAIGRE Hubert
RETHORE Julien
ADDA-BEDIA Mokhtar
FOURMEAU Marion